공학박사 학위논문

Experimental Study of Local Scouring at the Downstream of River Bed Protection

하천 하상보호구조물 하류부에서 국부세굴에 관한 실험적 연구

2016 년 2 월

서울대학교 대학원
건설환경공학부
박 성 원

ABSTRACT OF DISSERTATION

Experimental Study of Local Scouring at the Downstream of River Bed Protection

by Sung Won Park

Doctor of Philosophy in Civil and Environmental Engineering

Seoul National University

Professor Jin Hwan Hwang, Advisor

Local scouring at the downstream of the river bed protection is one of the most important parts of the design criteria and sustainable management of the upstream hydraulic structures, such as dam spillway, gated or fixed weir. Especially, bed erosions in the vicinity of hydraulic structures and temporal development of maximum scour depth can threaten the safeties of hydraulic structures. From the previous researches, it has been known that dominant factors on local scouring were temporal development of the scour depth, initial flow and turbulent characteristics and properties of the river bed materials from the numerical and experimental approaches. However inappropriate the assumptions of previous researches and limitation of the measurement and monitoring caused the application of various empirical coeffcients and scour prediction.

In this study, physical tests of the local scouring at the downstream of the fixed bed were conducted with movable bed materials with advanced laboratory facillities. Experimental approaches were focused on the temporal evolution of scoured hole and flow and turbulence characteristics in it at each time step in order to analyze the countermeasure of the excessive losses of the bed materials near the longitudinal transition. From the temporal change of the bed elevation at each time step, the empirical relationships between temporal change of the maximum scour depth and hydraulic conditions were concluded and can be used prediction of the value of the maximum scour depth. Especially depth averaged relative turbulence intensity at the longitudinal transition of bed and bed shear stress were revealed the dominant factors on the temporal change and equilibrium value of the maximum scour depth. To analyze the flow and turbulence characteristics in the stabilized scoured hole, similar physical process near the backward facing step were conducted with using the PIV and ADV measurement system. High resolution PIV system was helpful to analyze the flow pattern near the step and reults of the 3-D ADV system were postprocessed with despiking method and ensemble averaging which was based on consideration of the integral time scale. With the analysis of the flow and turbulence results in the stabilized scoured hole, occurrence of the reversal flow and turbulent shear layer near the scoured hole was revealed to be dominant on the additional bed losses from the bed.

To find the appropriate countermeasure of the maximum scour depth, additional tests with mesh grid generated turbulent flow near the transition were conducted with same condition of the upstream water supply and water depth at the end of the laboratory flume. Results of the larger values of the depth averaged relative turbulence intensity were concluded the detention of the temporal change of scour depth and decrease of the equilibrium-maximum scour depth. Empirical equations which were suggested in this study, can be used to predict the maximum scour depth with well-known hydraulic parameters. And they can be also applied to be the quantitative index of improvement and design of the rive bed protection for the less erosion of the bed materials near the river bed protection

keywords: Local Scouring, River Bed Protection, Depth-averaged Relative Turbulence Intensity, Maximum Scour Depth, Bed Shear Stress, Turbulence Shear Layer, Mesh Grid Genereated Turbulent Flow

Student Number: 2009-30231

TABLE OF CONTENTS

LIST OF FIGURES

LIST OF TABLES

LIST OF SYMBOLS

Latin Uppercase

A	Cross section
C	Chézy friction coefficient
C_{eq}	Equilibrium Coefficient of Local Scouring
C_r	Integral coefficient (~8.5±15%)
C_s	Integral coefficient (~5.0±25%)
D_*	Sedimentological diameter
E	Expected values
Fr	Froude number
K	Calibration coefficient
K_1	Coefficient
L_s	Total length of scour hole (e.g. longitudinal length from the transition to the first initial bed elevation at each time step)
L_1	Longitudinal distance from the longitudinal transition (x = 0) to the location of y_{m} at each time step
P	Pressure
Q	Water discharge
Re	Reynolds number
Re_*	Boundary Reynolds number
R_h	Hydraulic radius
S_f	Friction slope
S_0	Bed slope

T_i	Integral time scale
U_c	Critical mean velocity
U_e	External freestream velocity
$U_{m,e}$	Cross-sectional velocity of equilibrium state at $x= L_1$
U_0	Cross-sectional velocity

Latin Lowercase

a	Calibration exponent of density
a_m	Value of the maxima axe of PST method
a_1	Calibration coefficient of energy slope regression
a_2	Calibration exponent of energy slope regression
b	Calibration exponent of turbulence coefficient
b_m	Value of the minima axe of PST method
c	Calibration exponent of Froude number
d	Calibration exponent of Reynolds number
d_s	Diameter of sediment particle
d_{50}	Median size of d_s
e	Exponential
f_{DW}	Friction coefficient of Darcy Weisbach equation
g	Gravitational acceleration
$h_{m,e}$	Water depth of equilibrium state at $x= L_1$
h_0	Water depth at the longitudinal transition ($x= 0$)
k	Turbulent kinetic energy per unit mass
k_b	Turbulent kinetic energy at $u_* z/\nu= 70$

k_s	Nikuradse's equivalent roughness height
k_x	Stream-wise directional turbulence intensity
k_y	Span-wise directional turbulence intensity
k_z	Water-depth directional turbulence intensity
k_0	Depth-averaged turbulent kinetic energy at the transition
$q_{m,e}$	Discharge per unit width of equilibrium state at $x= L_1$
q_0	Discharge per unit width at the longitudinal transition ($x= 0$)
r	Correlation coefficient
r_0	Depth-averaged relative turbulence intensity
t	Elapsed time
t_n	Time step
t_1	Characteristic time at which $y_\mathrm{m} = h_0$
u	Instantaneous velocity of stream-wise direction
u'	Turbulence intensity of stream-wise direction
u_*	Bed shear velocity
$u_{*,c}$	Critical shear velocity
v	Instantaneous velocity of span-wise direction
v'	Turbulence intensity of span-wise direction
w	Instantaneous velocity of water-depth direction
w'	Turbulence intensity of water-depth direction
y_m	Maximum scour depth (e.g. the first minimum value of bed elevation from the transition at each time step)

Greek Uppercase

Δ^n	The n^{th} derivatives

Greek Lowercase

α	Turbulence coefficient
α_u	Coefficient of stream-wise directional turbulence intensity
α_v	Coefficient of span-wise directional turbulence intensity
α_w	Coefficient of water-depth directional turbulence intensity
α_{uv}	Calibration coefficient of stream-wise directional turbulence intensity
α_{uw}	Coefficient of stream-wise directional turbulence intensity
α_0	Coefficient of k_0
α_1	Calibration Coefficient of r_0 with Froude number
α_2	Calibration Coefficient of r_0 with Reynolds number
α_3	Regression Coefficient of r_0
β_1	Calibration exponent r_0 with Froude number
β_2	Calibration exponent of r_0 with Reynolds number
δ	Boundary layer thickness
δ_*	Displacement thickness
θ	Momentum thickness
θ_d	Downstream scour slope (bed slope of the positions from L_1 to L_s)
θ_r	Rotation angle of the principal axis in PST method
θ_u	Upstream scour slope (bed slope from longitudinal transition to the L_1)

κ	Von Kármán Coefficient
γ	Calibration exponent
μ	Dynamic viscosity of water
ν	Kinematic viscosity of water
ρ_w	Density of water
ψ_c	Shields' parameter
σ	Standard deviation
λ	Characteristic length scale
λ_U	Universal threshold term
ξ_i	Random variable
τ	Time lag
τ_0	Bed shear stress
$\tau_{0,\mathrm{RSS}}$	Bed shear stress using vertical distribution of the Reynolds shear stress

CHAPTER 1

INTRODUCTIONS

1.1 Backgrounds

Hydraulic structures, such as spillway of dam, culvert and weir in rivers and streams are generally built with additial structures of appropriate scales and shapes. Those additional structures are called as bed protection and distinguished with energy dissipation, stilling basin, apron, and end sill. All of them have their function and play important roles to reduce the excessive losses of bed materials and convert the hydraulic jump or jet flow into stabilized flow patterns (USBR, 1984; USBR, 1987, USACE, 1987; USACE, 1992; CIRIA, 2007).

In most conditions of flow and sediment transport in field, higher turbulent flow is generated due to the constriction of the channel width and depth, control of the water discharge from the upstream. Therefore, bed protections are often constructed in order to protect the structures and also river bed. Even though the bed protections are setup, excessive loss and erosion of bed materials are occurred locally and frequently. This erosion is called as the local scour hole and it can threaten the safety of the upstream structures and cause the failure of the upstream structures. Therefore, prediction and prevention of the local scouring should be performed with consideration of various situations (USACE, 1987; USACE, 1992; CIRIA, 2007). Recently, functions and designs of hydraulic structures at the upstream of the bed protections become more complicated. However, limitations of design procedure of bed protection frequently made the local scouring and failure of the hydraulic structures also. Therefore previous design process also should be modified to overcome the limitations with considerations of physical process of local scouring.

1.2 Objectives

The purpose of this study is to reveal the physical mechanism of local scouring with experimental approaches and analyze the method to reduce the predicted scouring scales. And results of this experimental study can be helpful for estimation.

Motivations of this study are as follows:

a) Dominant factors:

   What are the dominant factors on local scour?

   What are the research of dominant factors on local scouring recently revealed?

   What made the local scouring with those factors?

b) Equilibrium State:

   How can the local scouring reach to the equilibrium state?

   Is it possible to estimate the equilibrium state of the maximum scour depth?

   Is previously suggested equations to predict the equilibrium maximum scour depth appropriate and applicable to the most cases?

c) Flow Characteristics:

   What are the hydraulic charactersitics in the scoured hole?

   Do they affect to the local scouring?

d) Engineering Application:

   How can this research be applied to the field conditions and problems?

1.3 Overview of Thesis

Theoretical backgrounds of flow patterns in various boundary and sedimentological parameters were reviewed in Chapter 2. And experimental setup and concepts of the tests were explained in Chapter 3 with measuring apparatus and research procedures. Chapter 4 consists of two parts. Firstly, temporal changes of local scouring were analyzed with experimental results. And secondly, flow and turbulence charactersitics, which can be dominant on sediment transport in the stabilized scoured were measured and compared with the scour process. And the MGGT flow condition, which can be a new concept of the countermeasure against the local scouring at the downstream of the fixed bed, were described and tested in Chapter 5. Dominant factors, which were revealed in Chapter 4 and 5 were combined as the normalized scales of the scouring in Chapter 6. Lastly, concise conclusions and summaries of this study was decribed in Chapter 7. Brief information of the methodologies of this study was schematized in Figure 1.1.

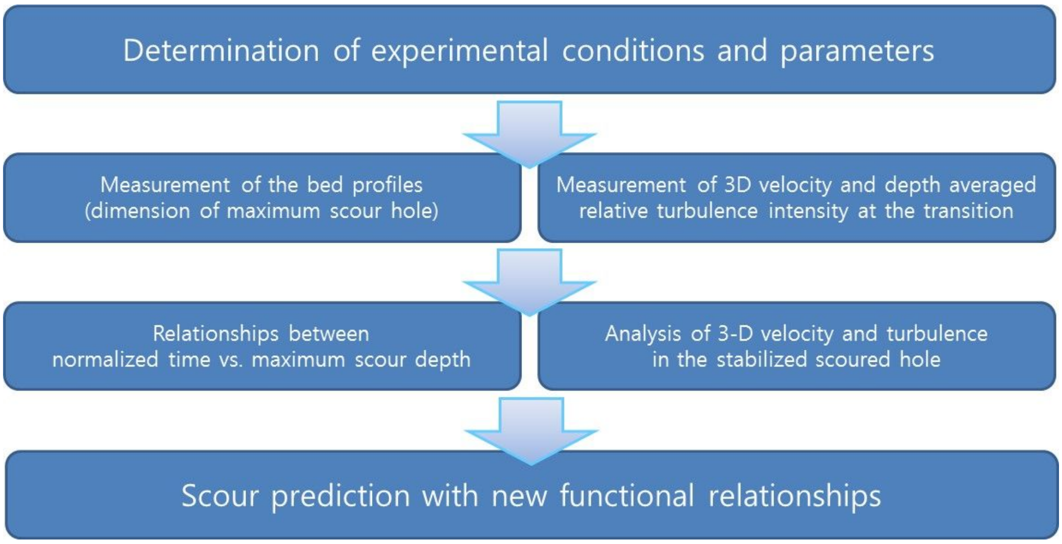

Figure 1.1 Schematic Diagram of the Research Methodologies

CHAPTER 2

THEORETICAL BACKGROUNDS

2.1 Local Scouring and Equilibrium State

2.1.1 Conceptual Model

Local scouring results directly from the impact of the structure and its operation on the flow and types of scour can be distinguished into jet scour, constriction scour, bend and bank scour, and etc. with sediment supply from the upstream or not. Scour process and notations of this study were schematized in Figure 2.1. L_s and y_m are the total length of scour hole (e.g. longitudinal length from the transition to the first initial bed elevation at each time step) and the maximum scour depth (e.g. the first minimum value of bed elevation from the transition at each time step), respectively. L_1 is the longitudinal distance from the transition (x = 0) to the location of y_m at each time step. And the bed slopes of L_1 and from L_1 to L_s (θ_u & θ_d: upstream and downstream scour slope) respectively affect the stability of the upstream structures and were found to be reached an equilibrium state faster than the other dimensions (Hoffmans, 1993). Meanwhile, the eroded sediment particles from the bed are moved toward downstream and deposited randomly and this sediment transport can make upper dimensions of scour hole. Especially, y_m is the most important dimension for the design of upstream structures such as bed protection, and has been considered dominantly in previous researches (Breusers, 1966; Monsonyi and Schoppmann, 1968; Dietz, 1969; van der Meulen and Vinjé, 1975; Buchko et al., 1987; Hoffmans and Verheij, 1997; Balachandar and Kell, 1997; Amoudry and Liu, 2009; Termini, 2010).

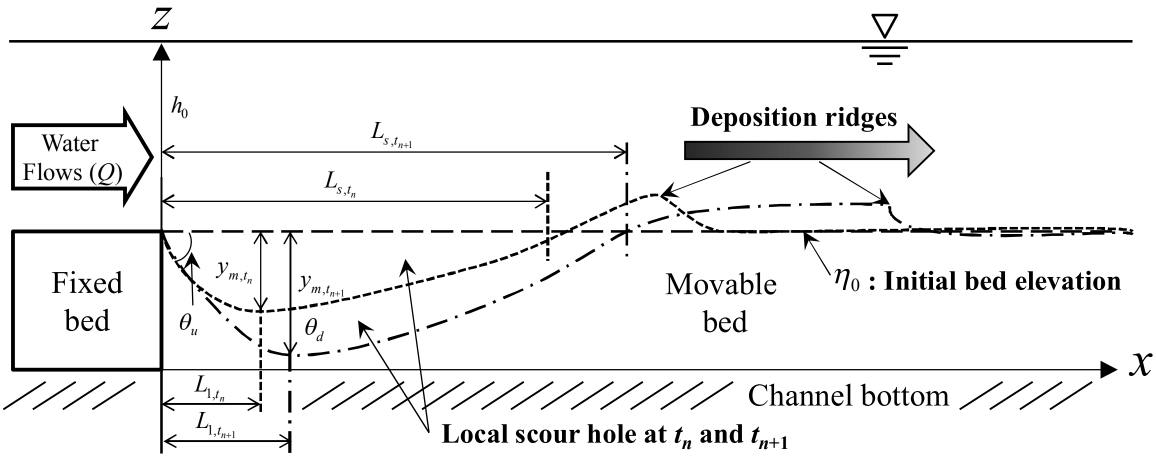

Q: water discharge from the upstream of the flume (m/s^3)
h_0: water depth at the tailgate of the flume (m)
η_0: initial bed elevation (m)
L_s: total length of scour hole (m)
y_m: maximum scour depth (m)
L_1: longitudinal distance from the longitudinal transition (x= 0) to the location of y_m (m)
θ_u: upstream scour slope (degree)
θ_d: downstream scour slope (degree)
t_n: time step (hour)

Figure 2.1 Conceptual Model of Local Scouring at the Downstream of Fixed Bed

2.1.2 Temporal Development

Based on the clear-water (no sediment supply from the upstream) scour experiments by Breusers (1966) and Dietz (1969), Zanke (1978) suggested four phases of the temporal evolution of maximum scour depth (Figure 2.2): an initial phase, a development phase, a stabilization phase and an equilibrium phase.

In the initial phase of local scour, the flow to the movable bed is mostly uniform in the longitudinal direction and erosion capacity in this phase is the most severe. Breusers (1966) showed that some bed material near the upstream scour slope goes into suspension at the beginning of the scour process. And most of the suspended particles follow convectional paths within the primary flow and remain in suspension due to the internal balance between the upward diffusive and the downward flux due to the gravity dominantly. Also some of the sediment particles will be settled and resuspended owing to the large scale and frequency of bursts of the turbulent flow near the movable bed, while some particles with a jump height smaller than a defined saltation or referece height are transported as the bed load.

In the development phase, dimensions of scouring increase considerably with same shape. In other words, ratios of L_1 and y_m at each time step in this phase are more or less constant. And values of θ_u reaches to the equilibrium state, but ones of θ_d changes slightly milder. Therefore, the values of the sediment transport in the upper part of the upstream scour slope is negligible, since the contribution of the sediment transport due to the instantaneous velocities in the downstream direction is approximately equal to the transport resulting from the instantaneous velocities in the upstream direction. Temporal change of normalized maximum scour depth was clearly revealed with power function in this phase.

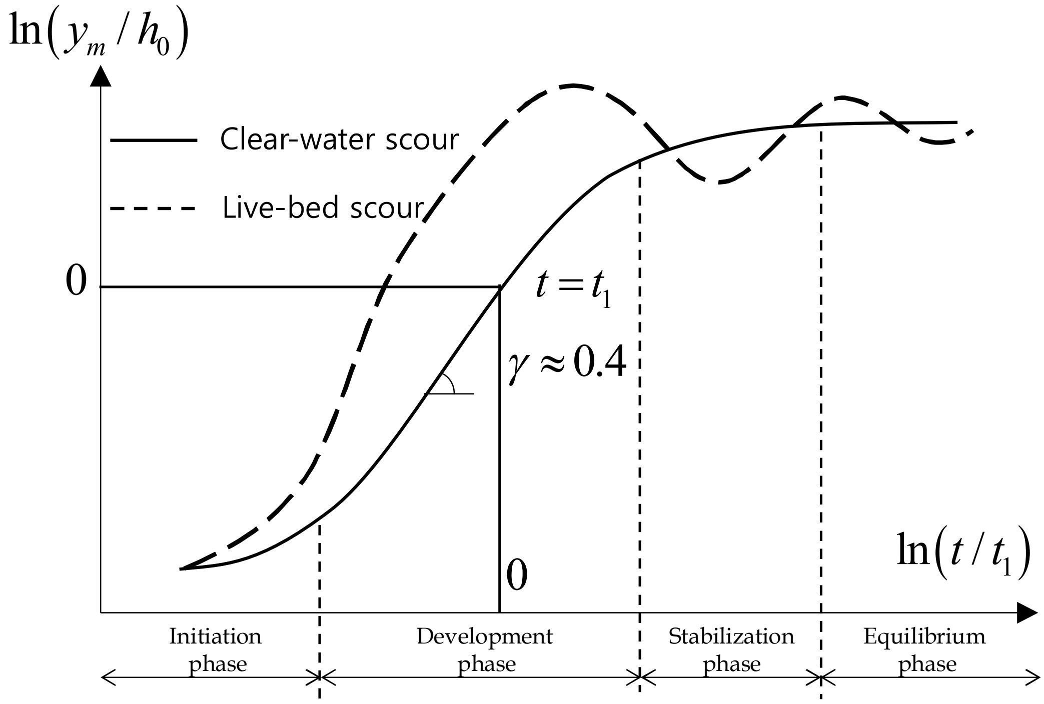

Figure 2.2 Temporal Phases of Normalized Maximum Scour Depth

(Hoffmans and Verheij, 1997)

In the stabilization phase the evolution rate of the maximum scour depth decreases gradually. The erosion capacity in the vicinity and upstream part of L_1 are much smaller than downstream of the point of reattachment, so that the values of L_s increase faster than those of y_m at each time step. In the stabilization and equilibrium phase both θ_u and y_m are mostly achieved. The equilibrium phase can be defined as the phase in which the dimensions of the socur hole do no longer change significantly (Zanke, 1978; Hoffmans and Verheij, 1997). However, each temporal phase does not have any quantatitive boundary, so that they can be defined only with the laboratory measurement and field observation.

In the stabilization phase the evolution rate of the maximum scour depth decreases gradually. The erosion capacity in the vicinity and upstream part of L_1 are much smaller than downstream of the point of reattachment, so that the values of L_s increase faster than those of y_m at each time step. In the stabilization and equilibrium phase both θ_u and y_m are mostly achieved. The equilibrium phase can be defined as the phase in which the dimensions of the socur hole do no longer change significantly (Zanke, 1978; Hoffmans and Verheij, 1997). However, each temporal phase does not have any quantitative boundary, so that they can be defined only with the laboratory measurement and field observation.

Since Breusers in 1966 conducted physical tests on local scour at the downstream of the fixed bed and suggested the temporal evolution of maximum scour depth in development phase, several hundreds of tests in which no sediment supply from the upstream were conducted by Mosonyi and Schoppmann (1968), Dietz (1969), van der Meulen and Vinjé (1975), Buchko et al. (1987), Hoffmans and Pilarczyk (1995), Balchandar and Kells (1997), and recently Termini (2011). Especially, Breusers (1966) suggested functional relationship between normalized maximum scour depth and time in developemtn phase as follows:

$$\frac{y_m(t)}{h_0} = \left(\frac{t}{t_1}\right)^{\gamma} \tag{2.1}$$

in which t and t_1 are elapsed time and characteristic time at which $y_m = h_0$ respectively. The maximum scour depth at t is denoted as y_m. And γ is the calibration exponent and also scouring rate (-). The left side of Eq. 2.1 is normalized length scale and right side of the upper equation is normalized time scale. Therefore each term in both sides of the equation 2.1 should have same units. Also values and ranges of calibration exponent (γ) have been previously estimated as 0.27-0.35 by Mosonyi and Schoppmann (1968), 0.34-0.40 by Dietz (1969), 0.4-0.8 by van der Meulen and Vinjé (1975), 0.2-0.4 by Hoffmans and Verheij (1997).

However, one of the limitations of Breuser's method is that it can be only applicable in the development phase of the temporal evolution of maximum scour depth (Hoffmans and Pilarczyk, 1995). Shortage on the prediction of scour development, because this method is drastically dependent on the calibration exponent. And also this method has an assumption that the length scale of largest eddy size is in the order of initial water depth, h_0. Therefore only the case, which equilibrium maximum scour depth is greater than the initial water depth, can use this method and acquire the reasonable accuracy on the prediction of it. Even the dimensions of largest eddy size for deep water conditions were suggested as those of the hydraulic structures, this method is not sufficient on most cases and problems of the local scouring and those prediction and appropriate characteristic length scale, which is dominant factor on local scouring near the transition, should be suggested (Hoffmans and Verheij, 1997).

Also the dependence of the characteristic time on the hydraulic conditions and material characteristics of channel bed has been investigated by several researchers (Breusers, 1966; Dietz, 1969; van der Meulen and Vinjé, 1975; Zanke, 1978; de Graauw and Pilarczyk, 1981). From those studies, t_1 could decribed by:

$$t_1 = \frac{K h_0^{\,2} \Delta^{1.7}}{\left(\alpha U_0 - U_c\right)^{4.3}} \tag{2.2}$$

in which K is 330 hrs $m^{2.3}/s^{4.3}$, α is turbulence coeficient (= $1+3r_0$), r_0 is depth-averaged relative turbulence intensity at the transition (=$\sqrt{k_0}/U_0$), k_0 is depth-averaged turbulent kinetic energy at the transition, U_c is critical mean velocity (=$u_{*,c}C/\sqrt{g}$, m/s), $u_{*,c}$ is critical shear velocity, which can be estimated from the Shields diagram, C is Chézy friction coefficient, g is gravitational acceleration (= 9.81 m/s^2), and D_r is relative density of bed materials.

$$t_1 = \frac{h_0}{U_0} \frac{K_1 D_r^{\,a}}{\alpha_u^{\,b} \mathrm{Fr}^c \, \mathrm{Re}^d} \tag{2.3}$$

Where, U_0 is cross-sectional velocity at the trsnsition (m/s), K_1 (=$g^{-1.43}\nu^{0.43}$) is coefficient (-), α_u is coeffcient (= $\alpha - U_c/U_0$), Fr and Re are Froude number (=$U_0\sqrt{gh_0}$) and Reynolds number (=$U_0 h_0/\nu$), ν is kinematic viscosity (= μ/ρ, 10^{-6} m^2/s in 20 ℃ water), μ and ρ_w are dynamic viscosity and density of water (= 1 t/m^3), and suggested values of empirical coefficients and exponents in equation 2.3 were compared in table 2.1.

Table 2.1 Empirical Coefficients and Exponents in Equation 2.2

(Hoffmans and Verheij, 1997)

Researchers	K_1	a	b	c	d
Breusers (1967)	0.94	1.62	4.0	2.70	0.30
Dietz (1969)	9.96	1.50	4.0	2.50	0.50
van der Meulen and Vinje (1975)	12.9	1.70	4.3	2.87	0.43
Zanke (1978)	-	1.33	4.0	2.67	0.33
De Graauw and Pilarczyk (1981)	17.1	1.70	4.3	2.87	0.43

2.1.3 Equilibrium State

Schematic diagram of equilibrium state of scour hole was described with concepts of the continuity equation in Figure 2.3. q_0 and $q_{m,e}$ are the discharge per unit width (m^2/s) at $x= 0$ and L_1, respectively. $h_{m,e}$ (= h_0 +$y_{m,e}$) is water depth at $x= L_1$.

Applying the continuity equation in the equilibrium state of the scoured hole,

$$U_0 h_0 = U_{m,e} h_{m.e} = U_{m,e} \left(h_0 + y_{m,e} \right) \tag{2.4}$$

where $U_{m,e}$ is cross-sectional mean velocity at $x= L_1$.

Assuming the equilibrium state with Eq. 2.4, and then Eq. 2.4 can be written as:

$$\frac{y_{m,e}}{h_0} = \frac{U_0 - U_{m,e}}{U_{m,e}} \tag{2.5}$$

Dietz (1969) applied $U_{m,e} = U_c / \alpha$ in Eq. 2.5 and suggested as follows:

$$\frac{y_{m,e}}{h_0} = \frac{\alpha U_0 - U_c}{U_c} \tag{2.6}$$

U_c in RHS of Eq. 2.6 can be estimated as follows:

$$U_c = 2.5\sqrt{\psi_c D_r g d_{50}} \ln\left(12 h_0 / k_s\right) \tag{2.7}$$

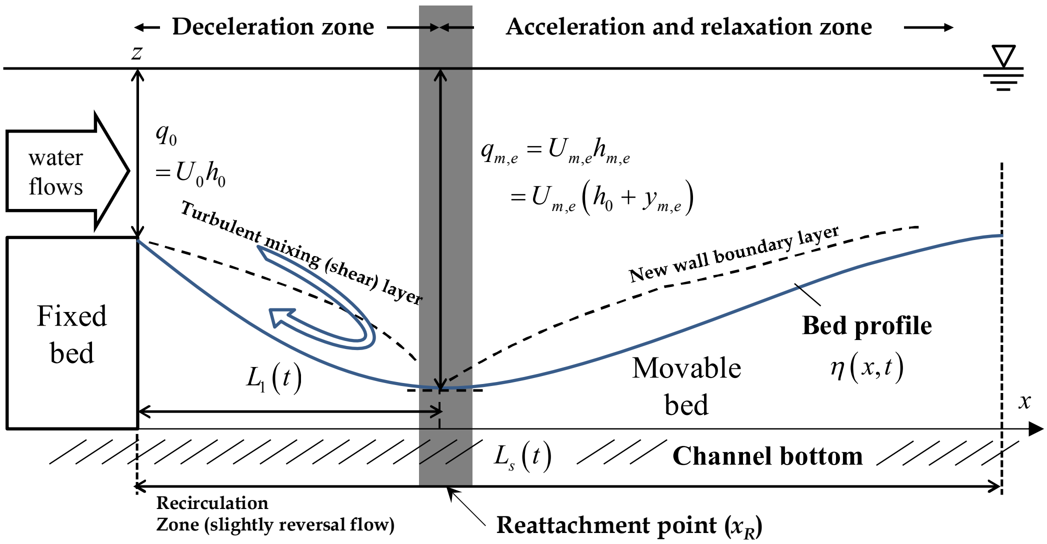

Figure 2.3 Equilibrium State of Maximum Scour Depth and Flow Characteristics

where ψ_c is Shields' parameter and k_s is Nikuradse equivalent roughness height (m) and can be calculated with consideration of hydraulic roughness as follows:

$$\mathrm{Re}_* = \frac{u_* k_s}{\nu} \tag{2.8}$$

where Re_* is the boundary Reynolds number and k_s equals to $3d_{90}$ (hydraulically rough, $\mathrm{Re}_*<4$) and k_s equals to $2d_{50}$ (hydraulically smooth, $\mathrm{Re}_*>100$), respectively.

Also Shields' parameter in Eq. 2.7 can be calculated from the Figure 2.4 with sedimentological diameter (D_*) as follows:

$$D_* = d_{50}\left(\frac{\Delta g}{\nu^2}\right)^{1/3} \tag{2.9}$$

Using Eq. 2.6, 2.7, 2.8, and 2.9, Maximum scour depth in the equilibrium state can be predicted.

Additionally turbulence coefficient, α in Eq. 2.6 depends mostly on the upstream geometric characteristics and can be interpreted as the erosion capacity. And several empirical expressions for α have been suggested (Table 2.2). A value of α can be calculated with depth-averaged relative turbulence intensity, r_0 which can be calculated with turbulence kinetic energy and depth-averaged flow velocity as follows:

$$r_0 = \frac{\sqrt{k_0}}{U_0} \tag{2.10}$$

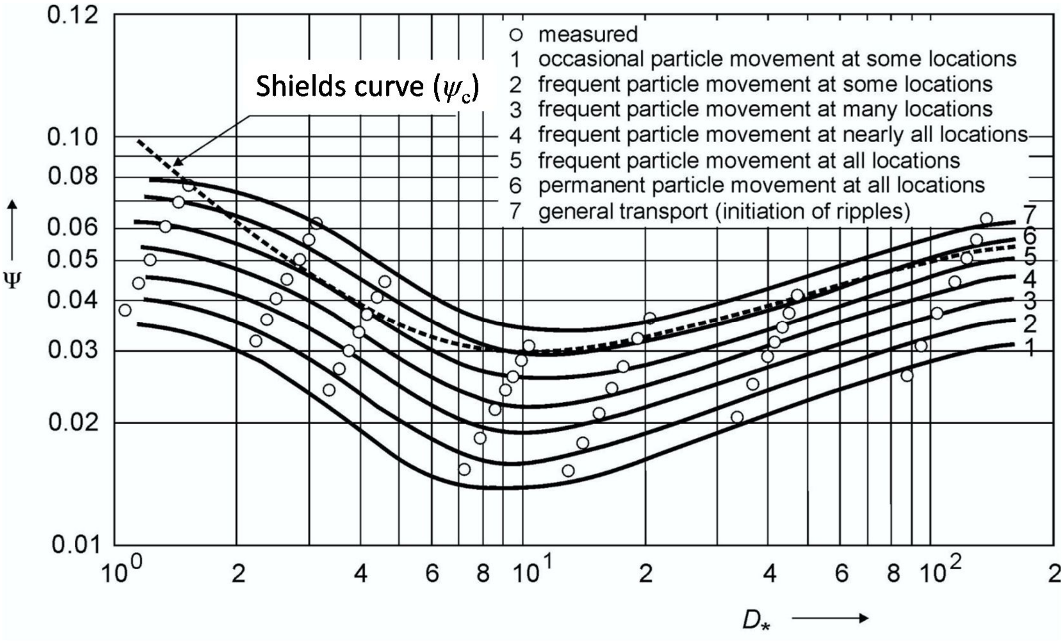

Figure 2.4 Shields Diagram (Revised by Hoffmans and Verheij, 1997)

Table 2.2 Turbulence Coefficient at the Transition (Hoffmans and Verheij, 1997)

Researchers	turbulence coefficient (α)
Dietz (1969)	$2r_0+2/3$ or $3\ r_0+1$
Popova (1981)	$0.87+3.25\mathrm{Fr}+0.3r_0$
Rossinsky (1956) & Blazejewski (1991)	1.05-1.7

where, k_0 is depth-averaged turbulence kinetic energy and can be calculated as follows:

$$k_0 = \frac{1}{h_0} \int_0^{h_0} k(z)\, dz \tag{2.11}$$

where, turbulence kinetic energy per mass (k) is usually defined as:

$$k = 0.5\left(\overline{u'}^2 + \overline{v'}^2 + \overline{w'}^2\right) \tag{2.12}$$

with three dimensional turbulence intensity:

$$k_x = \sqrt{\overline{u'^2}} \text{ (= stream-wise direction)} \tag{2.13-a}$$

$$k_y = \sqrt{\overline{v'^2}} \text{ (= span-wise direction)} \tag{2.13-b}$$

$$k_z = \sqrt{\overline{w'^2}} \text{ (= water-depth direction)} \tag{2.13-c}$$

Also three dimensional turbulence intensity can be calculated with difference from instantaneous flow velocity and time-averaged flow velocity as follows:

$$u = \overline{u} + u', \qquad v = \overline{v} + v', \qquad w = \overline{w} + w' \tag{2.14}$$

u, v, w are represented as stream-wise, span-wise, and water-depth directional flow velocity, respectively. And apostrophe denotes the standard deviation of 3-D flow velocity.

2.2 Mean and Turbulent Flow in Open Channel Flow

2.2.1 Bed Roughness Effects

a) Turbulent Boundary Layer

Bed roughness in open channel flow disrupts the laminar sublayer with frictional forces, which retard the motion of the fluid. The concept of a boundary layer is mostly due to Prandtl in 1904, who showed that the effects of friction within the fluid are significant only in a very thin layer close to the surface. The use of boundary layer theory has many important applications, such as the calculation of flow separation and skin friction drag.

Figure 2.5 presents a schematic showing the development of a vertical 2-D boundary layer on a smooth flat plate. The existence of the no-slip boundary condition at the wall retards the flow, resulting in a smooth stream-wise mean velocity profile $U(z)$, which smoothly merges into the external freestream velocity field, U_e. The boundary layer thickness $\delta(x)$ is considered to be the location above the surface at which the local mean velocity is 99% of the freestream value. Experimentally it is found that the $\delta(x)$ depends on the variables U, ρ, μ and the position x along the plate. And with those variables, δ is observed to be

$$\delta \sim \frac{\mu x}{\rho U} \sim \frac{x}{\sqrt{\mathrm{Re}_x}} \tag{2.15}$$

However, δ cannot be established with precision since the point separating the boundary layer from the zone of negligible viscous influence is not clearly separated.

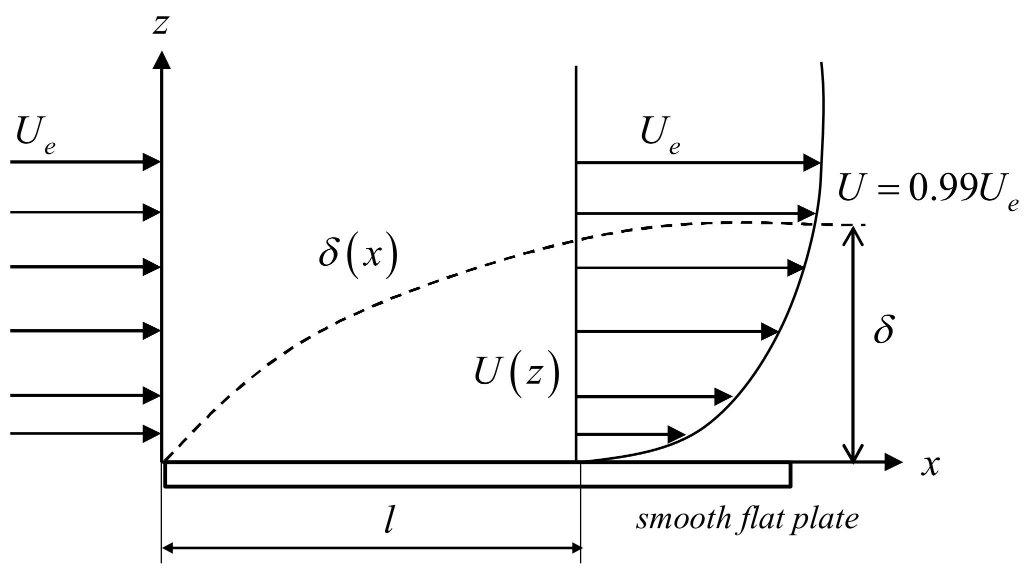

a) 2-D Tubulent Boundary Layer

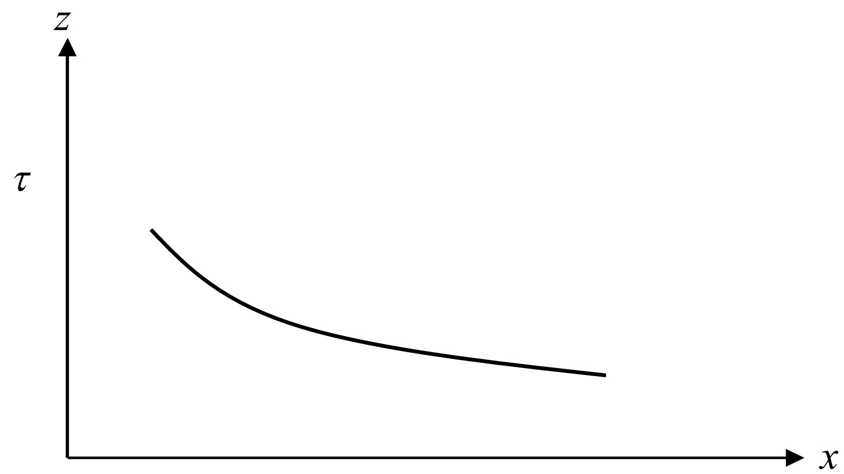

b) Shear Stress

Figure 2.5 Schematic Diagram of 2-D Tubulent Boundary Layer and Shear Stress on a Smooth Flat Plate (Daily and Harleman, 1966)

Therefore, apart from the boundary layer thickness, there are two other relevant length scales, namely, the displacement thickness, δ_* and momentum thickness, θ. The displacement thickness is the imaginary distance by which the wall would have to be displaced outward in a hypothetical frictionless flow so as to maintain the same mass flux as in the actual flow (Figure 2.6).

δ_* can defined as follows:

$$\rho U_e \delta_* = \rho \int_0^h \left(U_e - u \right) dz \tag{2.16-a}$$

$$\delta_* = \int_0^h \left(1 - \frac{u}{U_e} \right) dz \tag{2.16-b}$$

The flow retardation within δ also causes a reduction I the rate of momentum flux. It is useful to define a momentum thickness, θ as an imaginary layer of fluid of velocity U for which the momentum flux rate equals the reduction caused by the vertical distribution of velocity (Daily and Harleman, 1966; Kundu and Cohen, 2008).

θ is defined by

$$\rho \theta U_e^2 = \rho \int_0^h \left(U_e u - u^2 \right) dz \tag{2.17-a}$$

$$\theta = \int_0^h \frac{u}{U_e} \left(1 - \frac{u}{U_e} \right) dz \tag{2.17-b}$$

Upper length scales are caused by bed roughness, which can make a turbulent fluctuation from the bed and were described with respect to the bed roughness in detailed.

b) Bed Roughness

Bed roughness in open channel flow can be categorised as a complex boundary condition (Tachie et al., 2004). As mentioned earlier, the main effect of bed roughness is to increase the turbulence in vicinity of bed roughness elements. And the roughness properties such as friction coefficient, roughness height, and thickness of turbulent layer in uniform flow were widely researched by previous studies and mostly considered to analyze the mean and turbulent flow in open channel. However, no single formula cannot describe the velocity profiles over its total thickness, δ. Therefore, according to the value of Re_* (described in Eq. 2.8), hydraulical roughness can be catagorized in Figure 2.6. From the concept of the Prandtl's mixing length theory, distribution of universal velocity in smooth wall was developed as follows:

$$\frac{u(z)}{u_*} = \frac{1}{\kappa}\ln\left(\frac{u_* z}{\nu}\right) + C_s \tag{2.18}$$

where, κ is von Kármán coeffient (≈ 0.4) and C_s is a integral coefficient (approximately 5; ± 25 %).

Also, distribution of universal velocity in smooth wall was developed as follows:

$$\frac{u(z)}{u_*} = \frac{1}{\kappa}\ln\left(\frac{z}{k_s}\right) + C_r \tag{2.19}$$

where, C_r is a integral coefficient (approximately 8.5; ± 15 %).

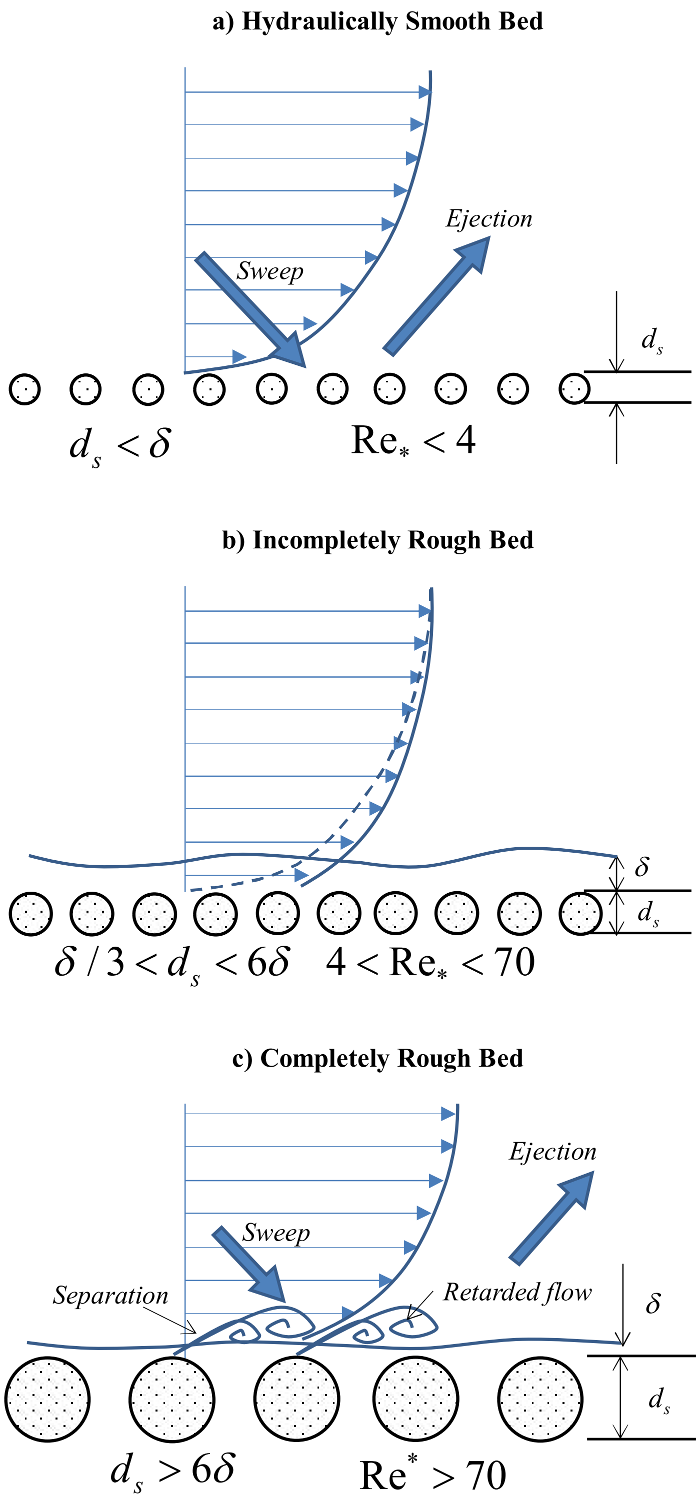

Figure 2.6 Classification of Hydraulic Roughness (Nezu and Nakagawa, 1993)

2.2.2 Initial Motion of Sediment

Initial condition of sediment particle movement is based on the balance of the total forces, i. e. drag force, weight of sediment particle, lift force, and resistance force on sediment particle in water flows. Also geometric characteristics of sediment particle such as shape factor (ratio of longest and shortest length of sediment particle), and specific weight and median size of it affect initiation of motion. Especially the concept of shear stress on sediment particle has played a major role in the initiation of sediment transport. Shields (1936) expressed the critical shear stress for the initiation of motion as a relation between the nondimensional shear stress, ψ_c (also called the Shields parameter or the Shields entrainment function) defined as:

$$\psi_c = \frac{u_{*,c}^2}{\Delta g d_{50}} \tag{2.20}$$

Several researches have modified Eq. 2.20 with more scatters from many laboratory experiments and field measurements (Simões, 2014; Figure 2.4).

In the case of sediment transport with hydraulic structures in rivers and stream, significant difference between bed protection and river bed with movable sediment particles. Neglecting the effects due to adaptation to a new flow pattern, the effective friction factor can be represented by an arithmetic average of the each friction factors, i.e.:

$$f_{eff} = \frac{f_{smooth} + f_{rough}}{2} \tag{2.21}$$

Several researches have been done for the flow with a serial roughness change. A smooth-to-rough change causes an overshoot in bed shear stress due to the stream-wise advection of water with a relative high velocity close to the bottom. And Vermaas (2008) have analyzed that a serial change in bed roughness gives caused to extra friction in comparison to the arithmetic mean friction factor calculated by equation 2.21 with experimental researches. Therefore, a serial roughness change is schematized here as an abrupt change (smooth to rough bed) in bed roughness in stream-wise direction (Figure 2.7). Substantially larger value of turbulent layer thickness will be appeared and cyclic motion of flow and turbulence will also appear in this layer.

2.2.3 Backward Facing Step Flow

Steady and uniform stream flow past an abrupt change of the bed elevation (i. e. backward-facing step flow) has been researched by many researchers, such as Nakagawa and Nezu (1987), and Malley et al. (1991). Nakagawa and Nezu (1987) found that the instantaneous reattachment zone, which has a log-law distribution of stream-wise velocity, occurred over a distance of 3 to 9 times the step height, and gradually decreased 5 as the Reynolds number becomes larger. Also Malley et al. (1991) revealed that the effective length scale of reattachment zone and step height and values of pressure from the transition to reattachment length scale were negative. To analyze the cyclic motion in the turbulent shear layer behind the step, both of these researches applied the *Kelvin-Helmholtz model* and *kolk-boil vortices*, respectively (Figure 2.8). Especially length scale of reattachment zone is 5-18 times of step height in the case of Re<10,000 and 5-8 times in the case of Re>20,000, respectively (Figure 2.9).

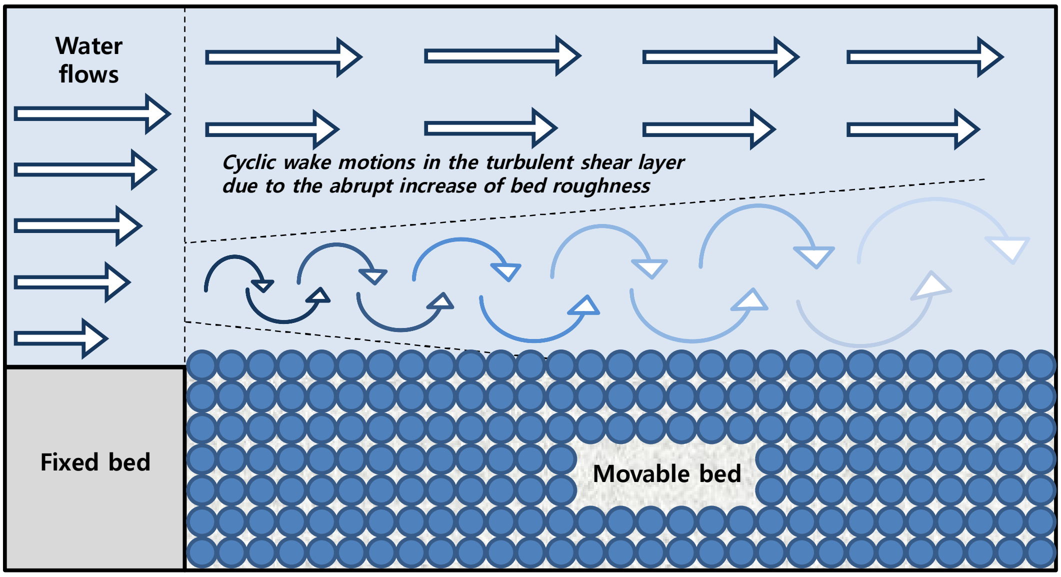

Figure 2.7 Flow Separation and Turbulent Shear Layer in Abrupt Change of Bed Roughness

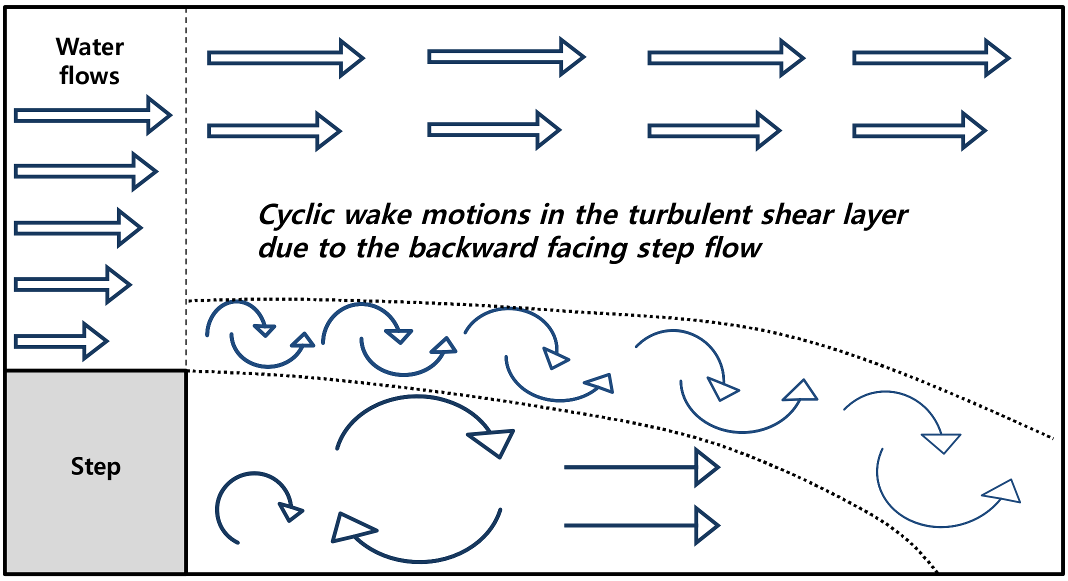

Figure 2.8 Flow Separation and Turbulent Shear Layer in Backward-facing Step Flow

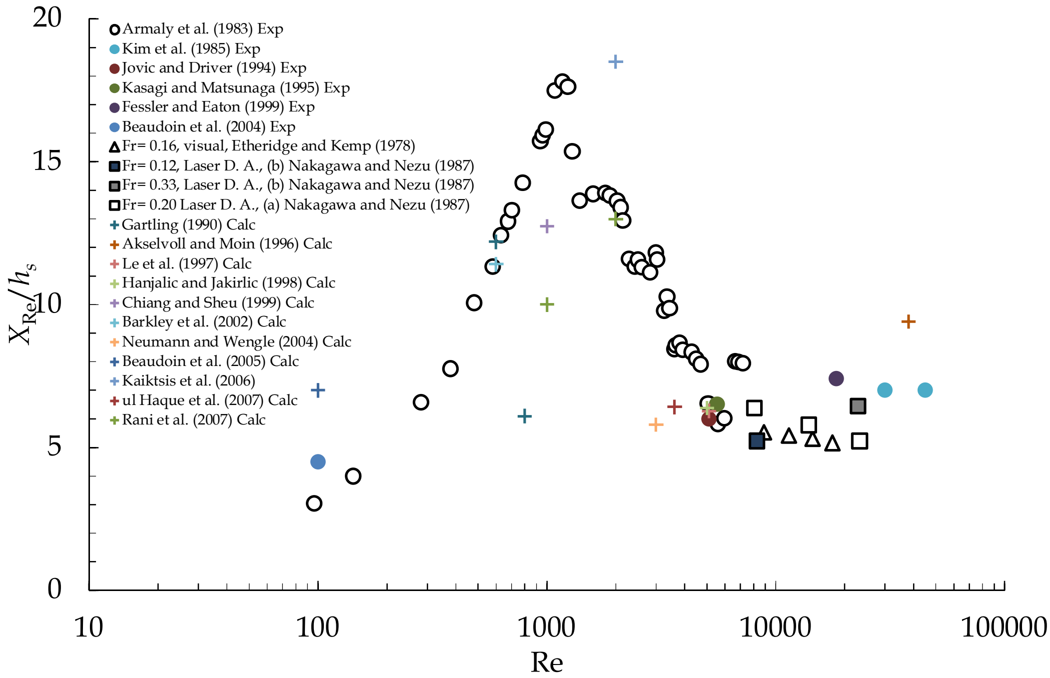

Figure 2.9 Variation of Normalized Reattachment length Scale and the Reynolds Number in Backward-facing Step Flow in Open Channel

2.3 Estimation of Flow and Turbulence Properties

2.3.1 Despiking Method

Due to the many reasons, such as mistake of configuration, capture of the undesirably moving particles, and rapidly varied flow conditions, single and multiple points of the spiked signals of velocity data can be acquired with Acoustic Doppler Velocimetry as invalid data. Several methods to overcome these problems were suggested previously (Goring and Nikora, 2002; Doroudin, et al., 2010; Jesson, et al., 2012). Measured velocity data in the invalid region of the velocity of this study were detected with the PST (Phase-Space Thresholding) method which was suggested by Goring and Nikora (2002). This method iterates until the number of good fittable data becomes constant (or, equivalently, the number of new points identified as spikes falls to zero). Each iteration has the following procedures:

- Calculate the surrogates for the first and second derivatives from the following equations:

$$\Delta u_i = \left(u_{i+1} - u_{i-1}\right)/2 \tag{2.22}$$

$$\Delta^2 u_i = \left(\Delta u_{i+1} - \Delta u_{i-1}\right)/2 \tag{2.23}$$

- Calculate the standard deviations of all three variables, σ_u, $\sigma_{\Delta u}$, and $\sigma_{\Delta^2 u}$, and then also estimate the expected maximum using the Universal criterion as follows:

$$E\left(\left|\xi_i\right|_{\max}\right) = \sqrt{2\ln n} = \lambda_U \quad (2.24\text{-a})$$

$$\lambda_U \hat{\sigma} = \sqrt{2\ln n}\hat{\sigma} \quad (2.24\text{-b})$$

- Calculate the rotation angle of the principal axis of $\Delta^2 u_i$ versus u_i using the cross correlation as follows:

$$\theta_r = \tan^{-1}\left(\sum u_i \Delta^2 u_i / \sum u^2{}_i\right) \quad (2.25)$$

- Here, it should be noticed that for $\Delta\, u_i$, u_i and for $\Delta^2\, u_i$ versus $\Delta\, u_i$ $\theta \equiv 0$ due to the symmetry.
- For each pair of variables, calculate the ellipse that has maxima and minima from 3 above. Thus, for Δu_i versus u_i the major axis is $\lambda_U \sigma_u$ and the minor axis is $\lambda_U \sigma_{\Delta u}$; for $\Delta^2 u_i$ versus Δu_i the major axis is $\lambda_U \sigma_{\Delta u}$ and the minor axis is $\lambda_U \sigma_{\Delta^2 u}$; and for $\Delta^2 u_i$ versus Δu_i the major and minor axes, a_m and b_m, respectively, can be shown by elementary geometry to be the solution as follows:

$$a_m{}^2 \cos^2\theta + b_m{}^2 \sin^2\theta = \left(\lambda_U \sigma\right)^2 \quad (2.26\text{-a})$$

$$a_m{}^2 \sin^2\theta + b_m{}^2 \cos^2\theta = \left(\lambda_U \sigma_{\Delta^2 u}\right)^2 \quad (2.26\text{-b})$$

For each projection in phase space, identify the points that lie outside of the ellipse and replace them. Eliminated data sets were replaced with the method of the cubic polynomial interpolation of best fit through the 12 data points on either side of the eliminated data.

2.3.2 Integral Time Scale and Ensemble Averaging

Most researches related to the capability of acoustic Doppler velocimeters to resolve the flow turbulence has focused on definition of the noise level present in the signal and how it can be removed by many researches (García et al., 2005). With consideration of integral time scale, it is known that undesired fluctuations of veloctity fluctuation can be stabilized in time domain.

A normalized autocorrelation function, $r(\tau)$ of single value, $u_i(t)$ at two times t and $t+\tau$ can be defined as follows:

$$r(\tau)=\frac{\overline{u_i(t)u_i(t+\tau)}}{\overline{u_i^2}} \tag{2.27}$$

The correlation coefficient, $r(\tau)$ specifies how correlated $u_i(t)$ and $u_i(t+\tau)$ are to each other. A typical autocorrelation plot is shown in Figure 2.10. Under normal conditions value of $r(\tau)$ goes to 0 as time lag, $\tau\rightarrow\infty$, because a process becomes uncorrelated with itself after a long enough time. A measure of the width of the correlation function can be obtained by replacing the measured autocorrelation distribution by a rectangular height 1 and width T_i, which is given by:

$$T_i \equiv \int_0^\infty r(\tau)\,d\tau \tag{2.28}$$

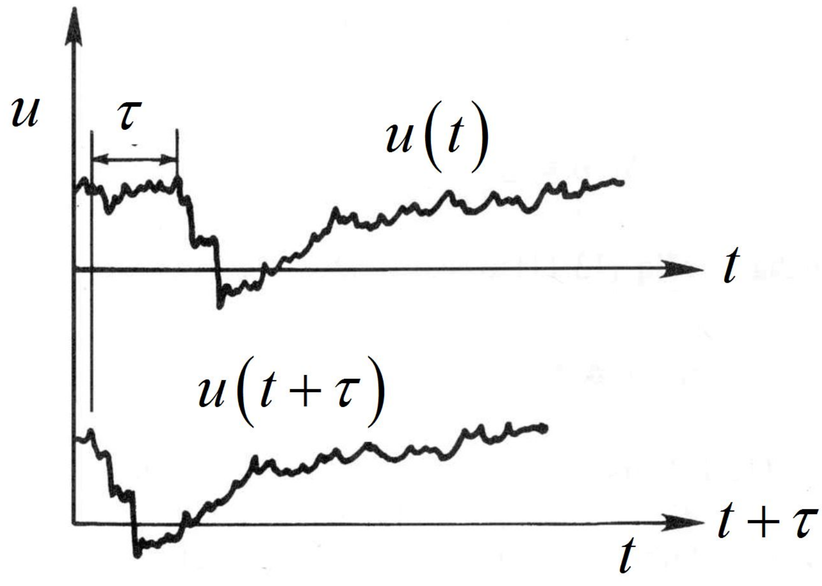

a) Auto-correlation function of instantaneous velocity data

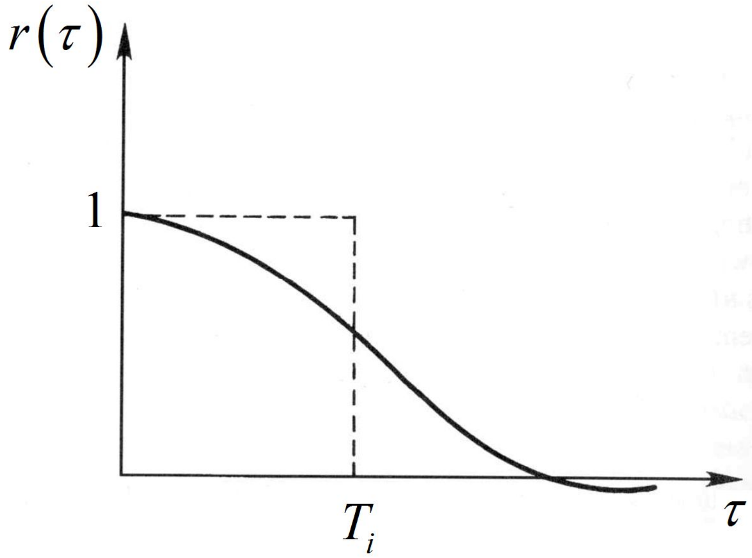

b) Auto-correlation coefficient and integral time scale

Figure 2.10 Auto-correlation and Integral Time Scale (Kundu and Cohen, 2008)

This is called as the integral time scale, which is a measure of the time over which is highly well-correlated with itself. In other words, T_i is a measure of the memory of the process (Kundu and Cohen, 2008). Obviously, $r(\tau)$ equals one. Because the estimated values of it are not zero, O'Neill et al. suggested and compared the determinations of the integral time as:

- Integration over the entire available domain (theoretical method);
- Integration only up to the value where the autocorrelation function is a minimum, if the autocorrelation function has a negative region (Tritton, 1988);
- Integration only up to the first zero-crossing (Katul and Parlange, 1995); or
- Integration only up to the value where the autocorrelation function falls to $1/e$ (Tritton, 1988).

And third method (Katul and Parlange, 1995) to determine the integral time scale was applied in this research. After determining values of integral time scales from total data of 3-D instantaneous flow velocity, data of instantaneous flow velocity can be ensemble averaged with based on maximum value of determined integral time scales in three dimensional direction of measuring sensor with assumption of ergodic state (Figure 2.11). This method can remove the totally-uncorrelated or despiked values of instantaneous flow velocity data from the mistake on mis-alignment of physical setup, velocity range, sampling volume, transmit length, and relatively low level of SNR of measuring sensor. Therefore it can also make us to avoid the excessive calculation of turbulence properties.

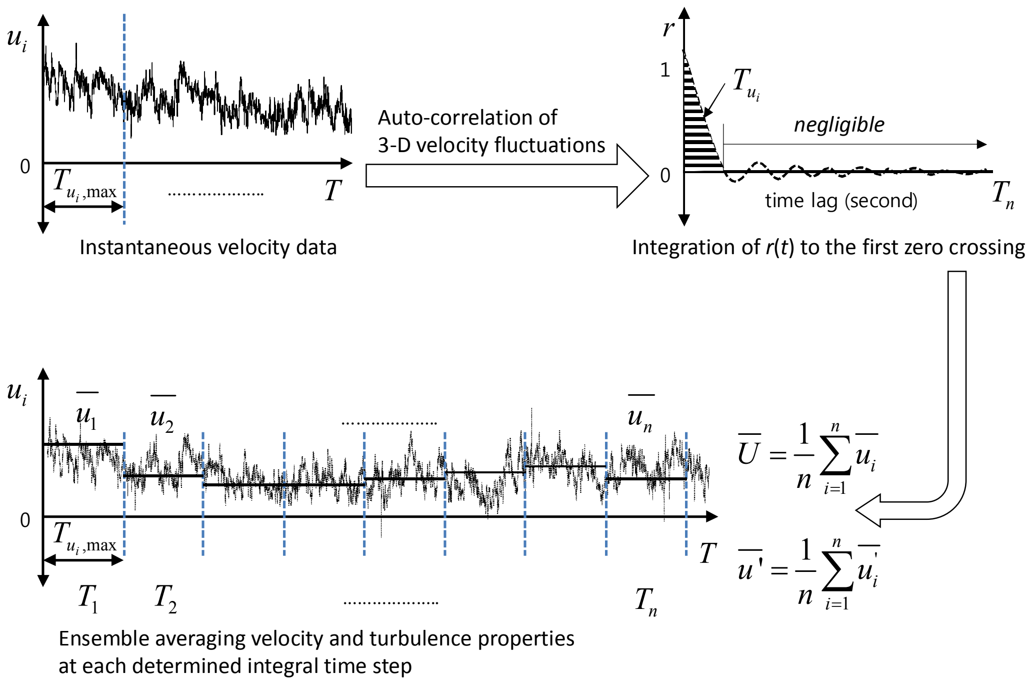

Figure 2.11 Schematic Diagram of Ensemble Averaging with Using Integral Time Scale

2.3.3 Mean and Turbulent Flow

a) Mean Continuity Equation

Analyzing the flow characteristics in scoured hole, an appropriate method of ensemble averaging was suggested in previous chapter. Spatial distribution of time averaged velocity should be satisfied with continuity equation as follows:

$$\overline{\frac{\partial}{\partial x_i}\left(U_i + u_i\right)} = \frac{\partial U_i}{\partial x_i} + \overline{\frac{\partial u_i}{\partial x_i}} = \frac{\partial U_i}{\partial x_i} + \frac{\partial \overline{u_i}}{\partial x_i} = 0 \qquad (2.29)$$

where U_i is time averaged velocity and u_i is turbulent deviation of the U_i. And subscript of i denotes the three dimensional direction. Using $\overline{u_i} = 0$, we can get:

$$\frac{\partial U_i}{\partial x_i} = 0 \qquad (2.30)$$

which is a condition of the continuity equation for the mean flow. And with Eq. 2.30, the following formula is also suggested (Kundu and Cohen, 2008).

$$\frac{\partial \overline{u_i}}{\partial x_i} = 0 \qquad (2.31)$$

Eq. 2.30 and 2.31 were used for the analysis of the time averaged values of mean flow and turbulence properties in the next chapter.

b) Turbulence Intensity

Nezu (1993) investigated the distribution of turbulent structure in smooth and rough bed open channel flows. Vertical distributions of normalized 3-D turbulence intensities with Eq. 2.13 were formulated in uniform flow condition as follows:

$$\frac{k_x}{u_*} = \frac{\sqrt{\overline{u'^2}}}{u_*} = \alpha_u \exp\left(-\frac{z}{h}\right) \tag{2.32-a}$$

$$\frac{k_y}{u_*} = \frac{\sqrt{\overline{v'^2}}}{u_*} = \alpha_v \exp\left(-\frac{z}{h}\right) \tag{2.32-b}$$

$$\frac{k_z}{u_*} = \frac{\sqrt{\overline{w'^2}}}{u_*} = \alpha_w \exp\left(-\frac{z}{h}\right) \tag{2.32-c}$$

where α_u, α_v, and α_w are coeffients (= 1.92, 1.34, 1.06, respectively). It is shown that the turbulent velocity fluctuations are order of bed shear velocity, u_*. The stream-wise turbulence intensities, k_z/ u_* are the largest, because the shear production initially feeds the energy into the *u*-component: the energy is subsequently distributed into the the other lateral components *v*, and *w* (Kundu and Cohen, 2008). The turbulent intensity initially rises as the wall in approached, however goes to zero right at the wall in a very thin wall layer as metioned in previous chapter.

c) Depth-averaged relative turbulence intensity

For smooth and rough channel flows, Graf (1998) defined the vertical distribution of turbulent kinetic energy per mass with Eq. 2.32 from Nezu's experimental relations as follows:

$$k(z) = 0.5\left[k_x^2(z) + k_y^2(z) + k_z^2(z)\right] = k_b \exp\left(-\frac{2z}{h}\right) \qquad (2.33)$$

with

$$k_b = 3.3u_*^2 \qquad (2.34)$$

where k_b is the turbulence energy at z^+ (= $u_* z/v$)= 70. For hydraulically smooth and uniform flow conditions, Nezu (1977) found

$$k_y(z) = \alpha_{uv} k_x(z) \qquad (2.35\text{-a})$$

$$k_z(z) = \alpha_{uw} k_x(z) \qquad (2.35\text{-b})$$

where α_{uv}= 0.71 and α_{uv}= 0.55. Hoffmans and Verheij (1997) combined Eqs. 2.32, 2.33, 2.34, 2.35 and suggested depth-averaged value of turbulence energy as follows:

$$k_0 = \frac{1}{h}\int_0^h k(z)dz = (\alpha_0 u_*)^2 \qquad (2.36)$$

$$\alpha_0 = \sqrt{0.5(1-\exp(-2))\cdot 0.5\alpha_u^2\left(1+\alpha_{uv}^2+\alpha_{uw}^2\right)} = 1.2 \qquad (2.37)$$

where α_0 is coefficient.

Normalized value of depth-averaged turbulence energy with Eq. 2.36 was suggested in Eq. 2.10 and can also be estimated with traditional bed roughness coefficient Chézy's C as follows:

$$r_0 = \frac{\sqrt{k_0}}{U_0} = \alpha_0 \frac{u_*}{U_0} = \alpha_0 \frac{\sqrt{g}}{C} \tag{2.38}$$

d) Reynolds Shear Stress

By averaging the Navier-Stokes equation with Eq. 2.29, 2.30 and 2.31,

$$\frac{\partial U_i}{\partial t} + U_j \frac{\partial U_i}{\partial x_j} = -\frac{1}{\rho}\frac{\partial P}{\partial x_i} - \frac{\partial}{\partial x_j}\overline{u_i' u_j'} + \nu \frac{\partial U_i}{\partial x_j \partial x_j} \tag{2.39}$$

which is known as Reynolds equation and P is pressure. This equation can be rewritten in the form of a general equation of motion for a fluid as follows:

$$\begin{aligned} &\frac{\partial}{\partial t}\rho U_i + \rho U_i U_j \frac{\partial}{\partial x_j} \\ &= \frac{\partial}{\partial x_j}\left[-P\delta_{ij} - \rho\overline{u_i' u_j'} + \mu\left(\frac{\partial U_i}{\partial x_j} + \frac{\partial U_j}{\partial x_i}\right)\right] \end{aligned} \tag{2.40}$$

Where δ_{ij} is the equivalent 3 × 3 matrix.

The first and second terms in LHS were represented the additional turbulent stress, i.e. the Reynolds shear stress. And for fully developed turbulence, the Reynolds shear stress approximately equals to vertical velocity gradient (= $\mu du/dz$).

2.3.4 Bed Shear Stress

Traditionally, to estimate the bed shear stress in open channel flow is one of the most important engineering works. Rashid (2010) suggested and compared six kinds of methods to estimate the bed shear stress from the data of flow velocity and turbulence characteristics in uniform open channel flow. In this study, 4 methods from the previous studies in uniform flow were introduced. And new concept of bed shear stress estimation was applied in non-uniform flow, i. e. flow condition in the scoured hole.

$$\tau_0 = -\rho_w \overline{u'w'} + \mu \frac{\partial u}{\partial z} \tag{2.41}$$

where the first term in the LHS represents the turbulent effect and the second one is based on the viscosity near the bottom of the channel.

a) LOW (Law of the Wall) method

With log-distribution of normalized stream-wise velocity Eq. 2.19 previously decribed, bed shear velocity can be estimated with consideration least-square method. In this method, practical ranges (z^+) of fitting were proposed previously, such as 30 or 70-500 or 2000 by Daily and Harleman (1966), 30-500 by Monin and Yaglom (1965), and 30-300 by Kundu and Cohen (2008) (Figure 2.12). The range of z^+ by Kundu and Cohen (2008) was selected in this study. LOW method have widely compared with newly-developed methods for the estimation of bed shear stress in many researches until now.

In this research, values of u_* and δ^* were calculated with this method and compared with the others, which were introduced in the following chapers.

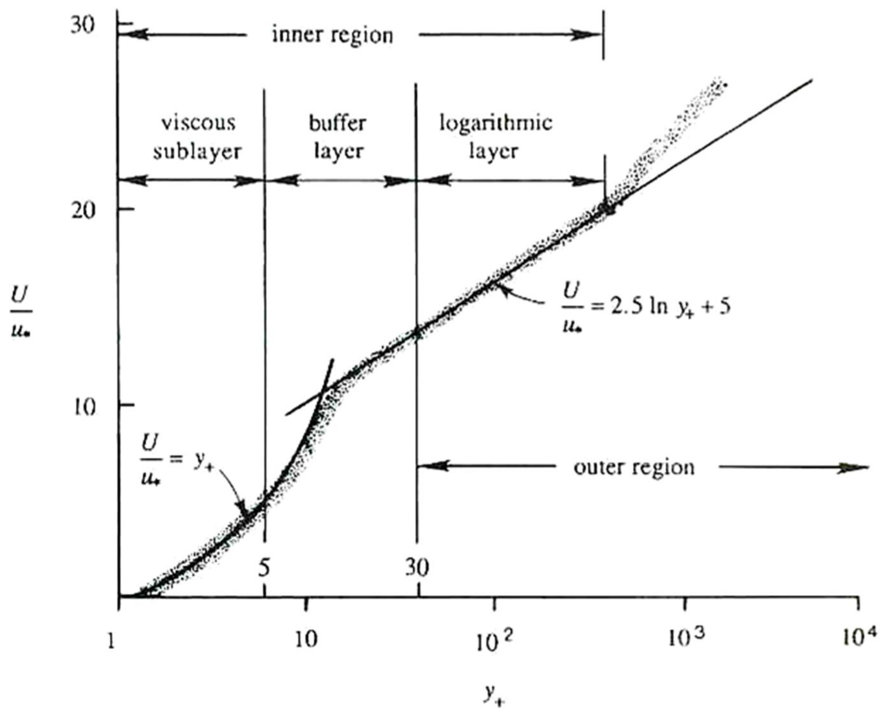

Figure 2.12 Functional Relationship between Dimensionless Stream-wise Velocity and Depth (Kundu and Cohen, 2008)

b) TKE (Turbulet Kinetic Energy) method

Graf (1998) suggested the Eq. 2.36 with using the results of Nezu and Nakagawa (1978). And Chézy coefficient can be also used to estimate the bed shear velocity with no experiment.

c) RSS (Reynolds Shear Stress) method

With experimental researches, vertical distribution of normalized Reynolds shear stress was proposed as follows:

$$\frac{\overline{u'w'}}{u_*^2} = \left(\frac{z}{h_0} - 1\right) \tag{2.42}$$

Bed shear stress can be extrapolated from the Eq. 2.41 with fitting the bed shear velocity. And if viscous shear stress,

$$\tau_{0,\mathrm{RSS}} = -\rho\overline{\left(u'w'\right)_{z\approx 0}} \tag{2.43}$$

d) SVE method

Three methods proposed previously, can be applied only in the case of uniform flow condition. Therefore new estimation method of bed shear stress and velocity, which is applicable in the case of non-uniform flow condition, such as in the scoured hole, was suggested. Graf and Song (1995) suggested methods to estimate bed shear stress from the Saint Venant equation. 1-D Continuity and momentum equation are as follows respectively:

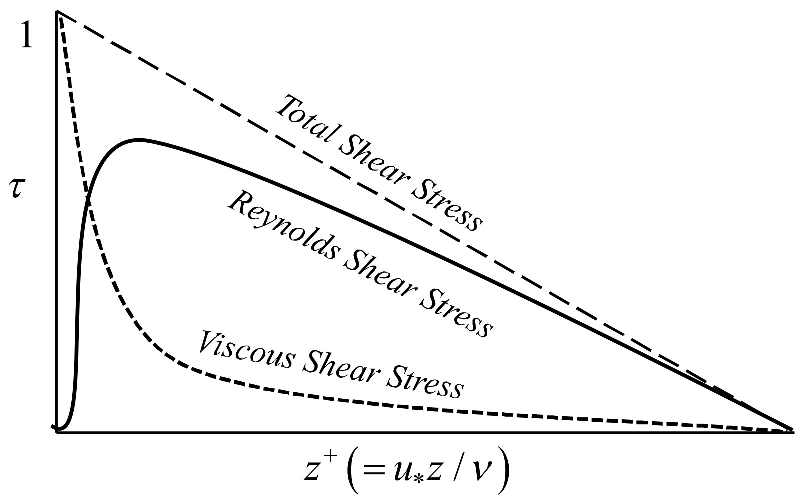

Figure 2.13 Vertical Distributions of Shear Stress in Open Channel Flow

$$\frac{\partial h}{\partial t}+U\frac{\partial h}{\partial x}+h\frac{\partial U}{\partial x}=0 \tag{2.44}$$

$$\frac{1}{A}\frac{\partial Q}{\partial t}+\frac{1}{A}\frac{\partial}{\partial x}\left(\frac{Q^2}{A}\right)+g\frac{\partial h}{\partial x}-g(S_0-S_f)=0 \tag{2.45}$$

Substituted $Q= AU$ into Eq. (2.41)

$$\frac{\partial U}{\partial t}+\frac{\partial U^2}{\partial x}+g\frac{\partial h}{\partial x}-gS_0+gS_f=0 \tag{2.46}$$

Divided by g

$$\frac{1}{g}\frac{\partial U}{\partial t}+\frac{U}{g}\frac{\partial U}{\partial x}+\frac{\partial h}{\partial x}-S_0+S_f=0 \tag{2.47}$$

Substituted $\tau_0= \gamma R_h S_f= \rho g h S_f$

$$\frac{1}{g}\frac{\partial U}{\partial t}+\frac{U}{g}\frac{\partial U}{\partial x}+\frac{\partial h}{\partial x}-S_0+\frac{\tau_0}{h\rho g}=0 \tag{2.48}$$

Multiplied gh to both sides of equation

$$\frac{h\partial U}{\partial t}+Uh\frac{\partial U}{\partial x}+gh\frac{\partial h}{\partial x}-ghS_0+\frac{\tau_0}{\rho}=0 \tag{2.49}$$

Substituted $\tau_0 = \rho u_*^2$ and then can be rewritten as follows:

$$u_*^2 = -\frac{h\partial U}{\partial t} - Uh\frac{\partial U}{\partial x} - gh\frac{\partial h}{\partial x} + ghS_0 \tag{2.50}$$

Substituted $\mathrm{Fr} = U_0 / \sqrt{gh_0}$ and then can be rewritten as follows with Eq. (2.40) by Graf and Song (1995)

$$u_*^2 = ghS_0 - gh\frac{\partial h}{\partial x}\left(1-\mathrm{Fr}^2\right) + \left(U\frac{\partial h}{\partial t} - h\frac{\partial U}{\partial t}\right) \tag{2.51}$$

With an assumption of steady state ($\partial h/\partial t = \partial U/\partial t = 0$) in the stabilized scoured hole (or at equilibrium state), third term in the right hand of Eq. (2.51) can be negligible as follows

$$u_*^2 = ghS_0 - gh\frac{\partial h}{\partial x}\left(1-\mathrm{Fr}^2\right) \tag{2.52}$$

Assuming that variation of the water surface is negligible,

$$S_0\left(x_i\right) = \frac{\Delta\eta_i}{\Delta x_i} = \frac{\eta_i - \eta_{i-1}}{x_i - x_{i-1}} \tag{2.53-a}$$

$$
\begin{aligned}
\frac{\partial h}{\partial x}(x_i) &= \frac{h(x_i)-h(x_{i-1})}{x_i - x_{i-1}} \\
&= \frac{h_0+\eta_0-\eta(x_i)-\left(h_0+\eta_0-\eta(x_{i-1})\right)}{x_i - x_{i-1}} \\
&= \frac{\eta(x_{i-1})-\eta(x_i)}{x_i - x_{i-1}} = -S_0
\end{aligned}
\tag{2.53-b}
$$

Substituted Eq. (2.53-a, b) into Eq. (2.52),

$$
u_* = \sqrt{ghS_0\left(2-\mathrm{Fr}^2\right)} \tag{2.54}
$$

Therefore, bed shear velocity at each longitudinal position in the stabilized scoured hole ($\Delta\eta/\Delta x > 0$ and $\mathrm{Fr}^2 < 2$) is as follows:

$$
u_{*,i} = \sqrt{g\frac{\Delta\eta_i}{\Delta x_i}\left(h_{0,i}+y_{s,i}\right)\left(2-\frac{U_0^{\ 2}}{g\left(h_0+y_{s,i}\right)}\right)} \tag{2.55}
$$

e) Modified RSS method

LOW, RSS method are not applicable to the non-uniform flow condition due to the assumption. Therefore to estimate the bed shear velocity near the scoured bed, modified RSS method was suggested with considering the change of bed elevation in the scoured hole as follows:

$$
\tau_{0,\mathrm{MRSS}} = \rho\overline{\left(u'w'\right)_{z\approx 0}} / \cos\theta_{x_i} \tag{2.56}
$$

CHAPTER 3

LABORATORY EXPERIMENTS

3.1 Experimental Setup

3.1.1 Experimental Flume

Laboratory experiments of this research were carried out in a glass-walled flume with tiliting devices. Dimensions of the whole flume are 17.5 m long, 0.6 m wide, and 0.8 m deep in the Hydraulic and Coastal Engineering Laboratory of Seoul National University (Figure 3.1). Head tank for stabilization of water supply with dimensions of 2.9 m long, 1.2 m wide, and 1.5 m high has been connected to the beginning of the channel and two perforated panels and submerged wall, which can effectively remove any rotational flow and irregular water surface undulation induced from the circulating pipeline, so that the stabilized flow can be supplied in the flume have been setup (Figure 3.2). Both sides of wall and partial part of channel bottom have been made of 8 mm and 12 mm thick glasses, respectively. A pair of sump tanks for water supply, storage and sediment entrapment were installed below the flume bottom and channel end, respectively and they were connected with a closed conduit (Figure 3.3). Especially transparent glassed bottom allowed the laser sheet to be shone from below the flume bottom. The flume was reinforced and supported by painted steel frameworks. Open channel for measurement was made with dimensions of 15.0 m long, 0.6 m wide, and 0.8 m wide. At the end of the channel, sluice gate which is made of a steel plate has been setup for controls of water surface elevation with motor operating system (Figure 3.4).

Figure 3.1 A photo of Flume from the Head Tank

a) Side View of Head Tank

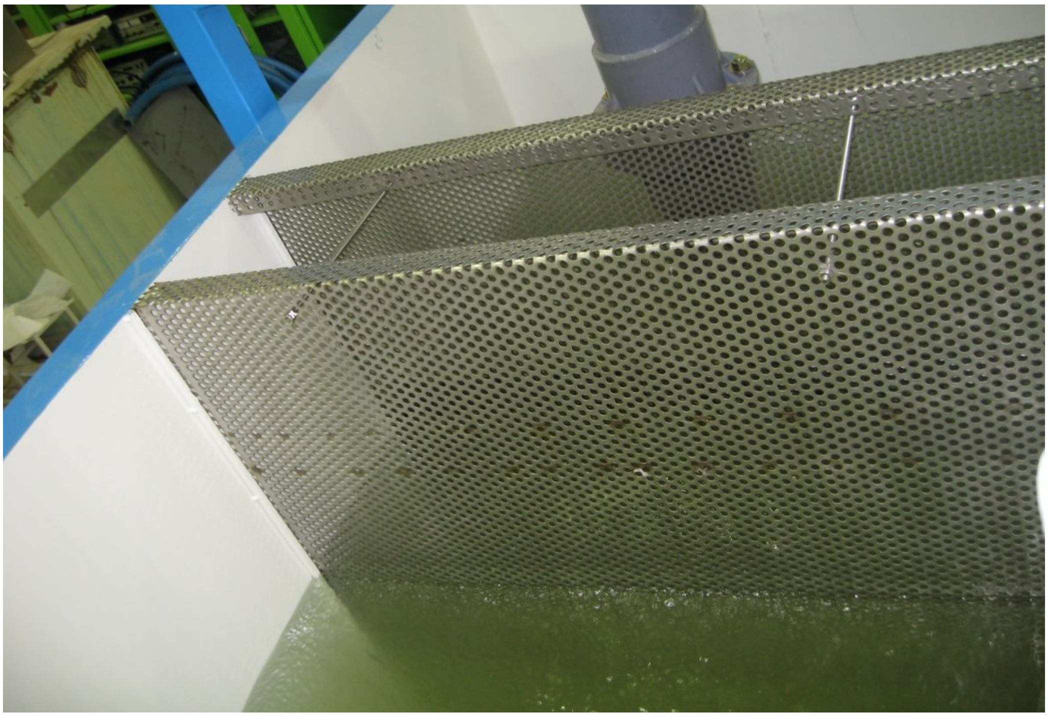

b) Perforated Panels in the Head Tank

Figure 3.2 Photos of Head Tank

a) A View from Right Side of Tail Gate

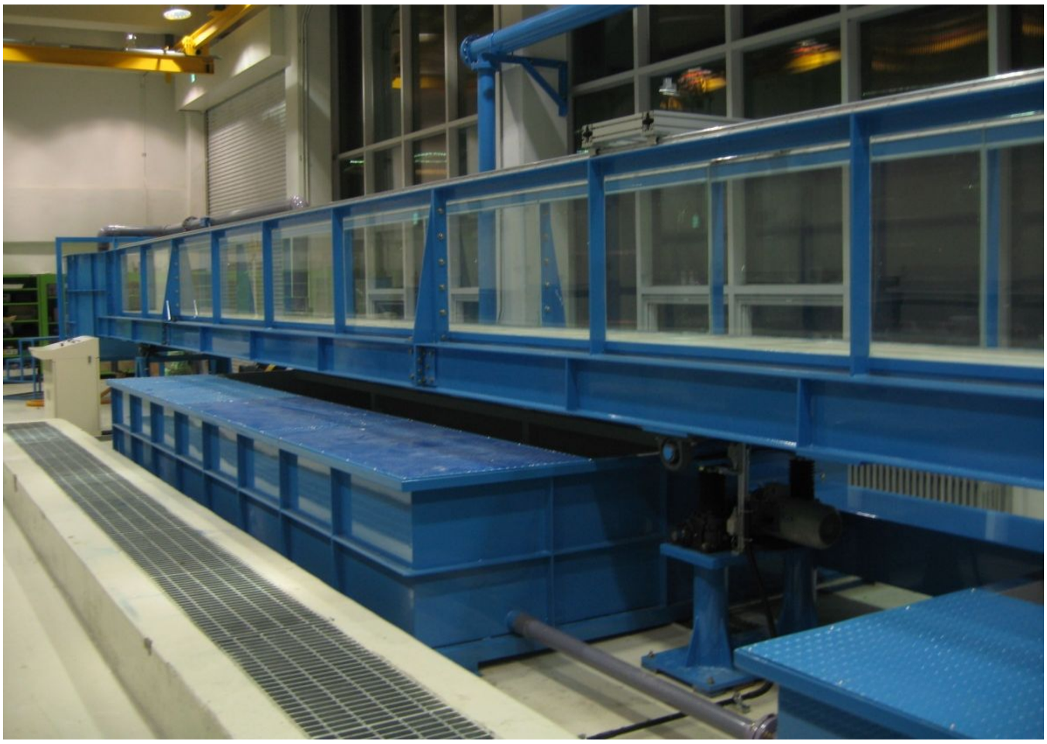

b) A View from left side of Tail Gate

Figure 3.3 Photos of Flume from the Tail Gate

Figure 3.4 A Photo of Tailgate at the End of the Flume

Figure 3.5 indicated the water supply and re-circulation system from the sump tanks into the test section of the flume. And information of the specific setup were described in detailed in following chapter. Additionally carriage on rails of the walls was setup for moving and mounting experimental appratus. And the auto-traverse system for positioning spanwise and water depth direction was mounted on the carriage. The two-axis autotraverse system can be controlled with the digital panel, which is connected with personal computer and the carriage can be moved and fixed manually. Also the autotraverse has the riveting plate for the positioning measuring apparatus (Figure 3.6).

3.1.2 Water Supply and Control

Water discharge for experiments is totally circulating as follows: Water from the first water supply tank is supplied by a water supply pump through the trumpet-shaped suction pipe and the ultrasonic flowmeter has been setup in the middle of the water supply pipe (Figure 3.7). Three phased power pump can supply upto 0.04 cms of water discharge steadily (Figure 3.8). A perforated pipe which has been setup in the head tank, can supply stabilized discharge of water through a pair of perforated paneles and low weirs. Passing the channel, discharge of water can be caught in the second water supply tank and be delievered to the first water supply tank through the conneting rectangular culvert which has been setup 0.5 m high from the bottom of the tank. The ultrasonic flowmeter in the middle of 10 mm diameter pipe has ±15 m per second measuring range and ± 0.5 % or less accuracy and acquired value of velocity can be displayed on the integrated control panel with real time. On the control panel, flow and slope display, control valve of water discharge and control button of slope, and termination button were installed (Figure 3.9).

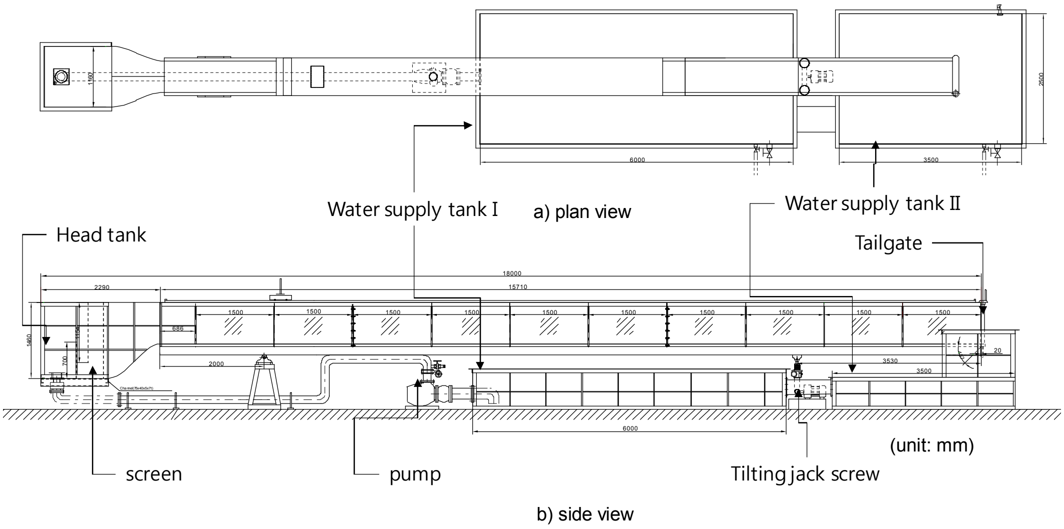

Figure 3.5 Schematic Diagram of Experimental Flume

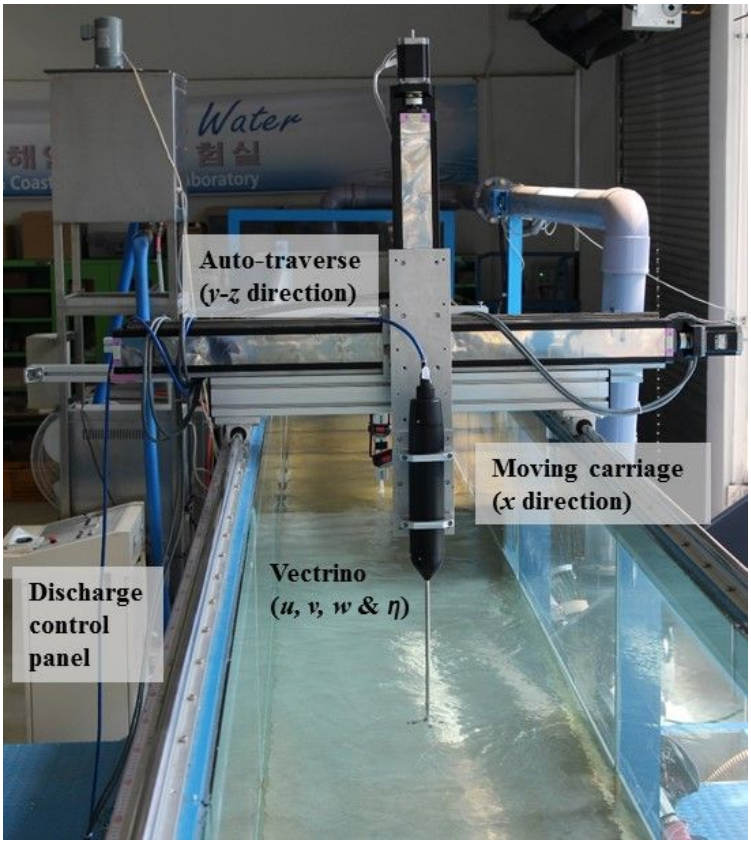

Figure 3.6 A Photo of Carriage and Auto-traverse System

Figure 3.7 A Photo of Ultrasonic Flowmeter (Ultraflux, France)

Figure 3.8 A Photo of Water Supply Pump

Figure 3.9 A Photo of the Control Panel and Display

3.2 Experimental Measurement

3.2.1 Measuring Appratus

a) Velocimeter

Single-point measurements of flow velocity and bed elevation change were conducted with down-looking Vectrino with rigid stem (Nortek™). The Vectrino uses the Doppler Effect to measure flow velocity and turbulence with 4-beam down-looking probes. The Doppler effect (or Doppler shift) is the change in frequency of a wave (or other periodic event) for an observer moving relative to its source. It is named after the Austrian physicist Christian Doppler, who proposed it in 1842 in Prague. It is commonly heard when a vehicle sounding a siren or horn approaches, passes, and recedes from an observer. Compared to the emitted frequency, the received frequency is higher during the approach, identical at the instant of passing by, and lower during the recession (Figure 3.10).

For the 3-D flow data acquisition, a pulse is transmitted from the centre transducer, and the Doppler shift introduced by the reflections from suspended particles in the water, is picked up by the four receivers (Figure 3.11). Sweet spot of the flow observation is 50 mm from the central transducer of the sensor with based on the maximum values of correlation and SNR (sound to noise ratio, dB). Especially, the reliable values of 3-D flow velocity data can be acquired with adequate combination of velocity range (from 0.03 to 4.00 m/s), sampling volume (from 2.5 to 8.5 mm), and transmit length. Inadequate combination of them can make the spiked values of flow velocity data (Figure 3.12; Table 3.1; Nortek, 2009). Alignment of the sensor on the auto-traverse system was described in Figure 3.6 and configuration of it was explained in following chapter 4.

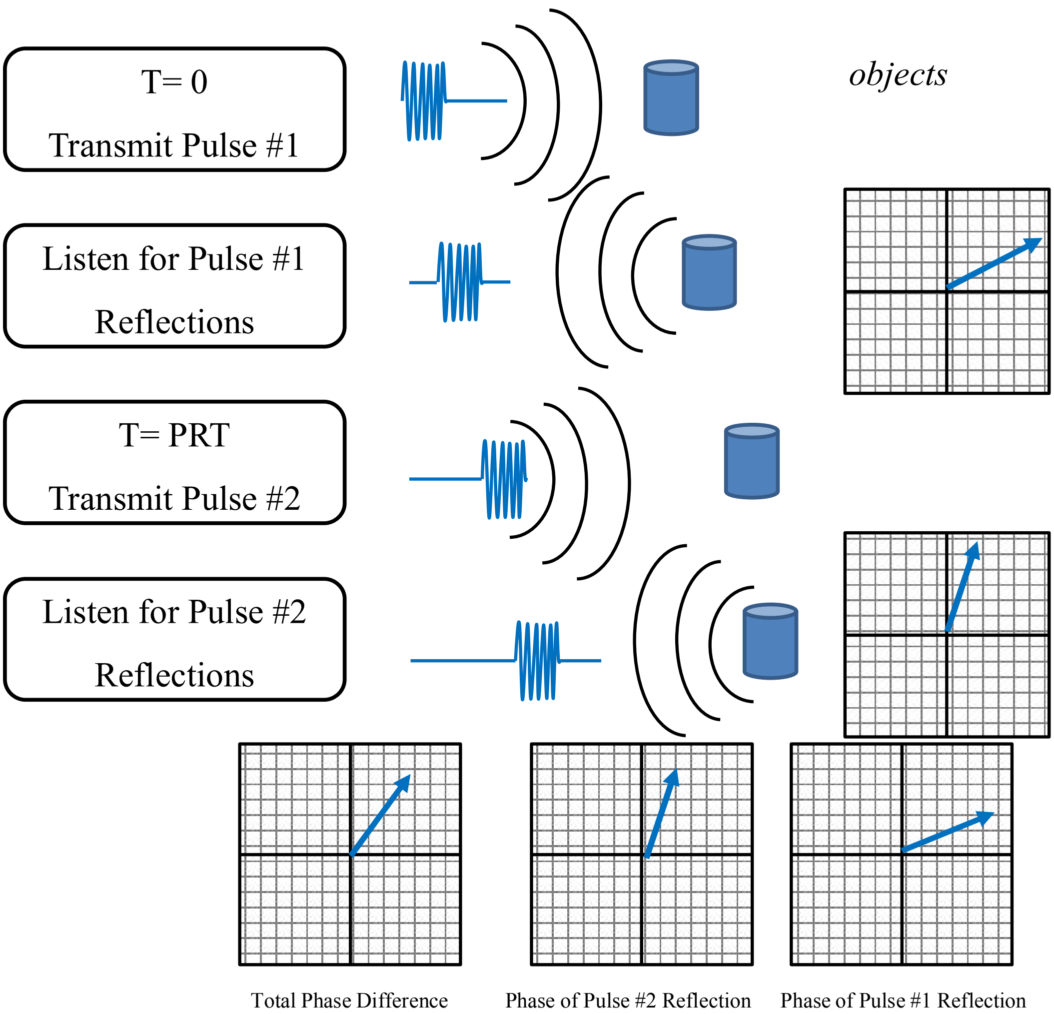

Figure 3.10 Schematic Diagram of the Pulse Coherent Processing of micro-ADV

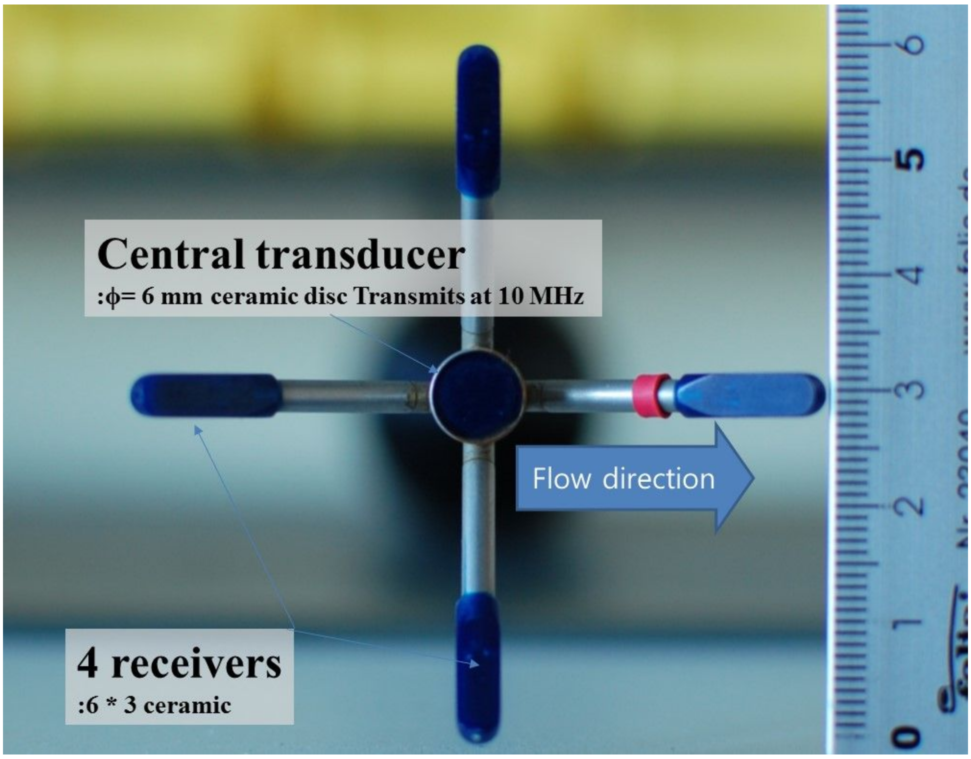

Figure 3.11 Bottom View of Vectrino Velocimeter (Nortek, 2009)

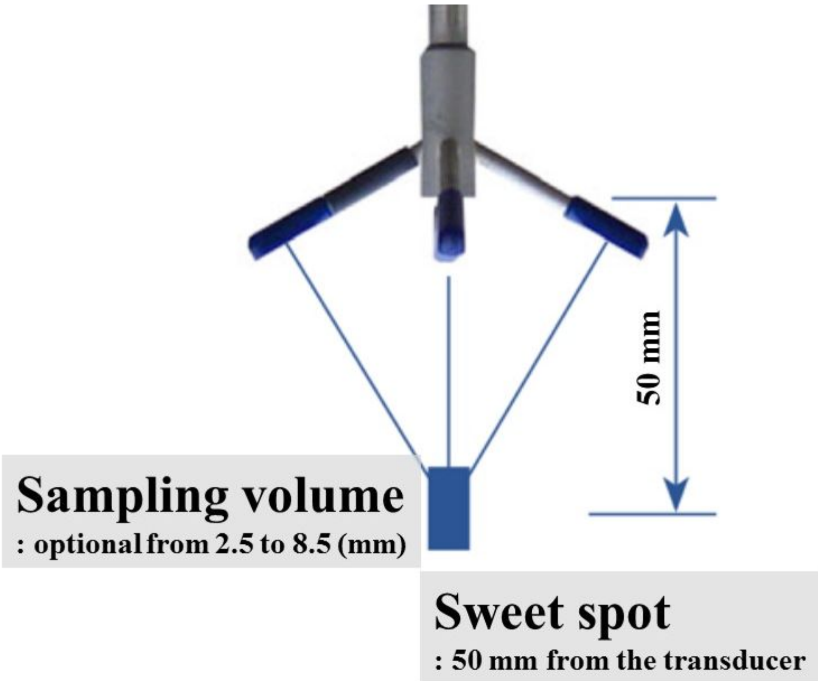

Figure 3.12 Schematic Diagram of Sweet Spot of the Vectrino (Nortek, 2009)

Table 3.1 Specification of Measuring Apparatus (Nortek, 2009)

Specifications		values
Sampling volume	Distance from the probe	50 mm (fixed value)
	Diameter	6 mm
	Cell size	-
Velocity range		± 0.01 ~ 4 m/s
Sampling rate		1 ~ 200 Hz
Accuracy		± 0.5 % of measured value ± 1 mm/s
Temperature		-4 ~ 40 ℃

b) PIV Measuring System

Particle Image Velocimetry, or PIV is an optical method to visualize fluid flows. PIV can measure the velocity of fluids and reveal fluid properties. Essentially for PIV measurement, the standard planar PIV system should be considered. PIV has been oftenly applied in aerodynamics and hydrodynamics to research how organisms swim, fly, and conduct fluids in the body and to design aircraft, submarines, cars, prosthetic hearts, etc. PIV refers to one of methods used in experimental fluid mechanics to determine instantaneous fields of the vectors by measuring the displacements of numerous fine tracer particles that accurately follow the motion of the fluid. Fundamental theory of the particle image capturing was schematized in Figure 3.13-a (Stella et al., 2001; Adrian and Jerry, 2010).

It consists of a double-pulsed laser, light-sheet-forming optics, particle seeding, a monoscopic (single-lens) camera, image digitization hardware, and a computer for data storage and analysis (Figure 3.13-b). For visualization of flow near step, four components have been used. A laser supply is 135 mJ dual Nd:YAG, specified with 532 nm wavelength and 15 Hz pulse rate. A digital camera with 2M resolution can capture the fluid motion with relatively large size of interrogation area. All of components can be synchronized for exchanging the signals of capturing commands and images with the synchronizer. Specification of components has been described in Figure 3.14-17.

In this research, PIV measurement was applied for flow visualization and turbulent thickness estimation in the backward facing step flow. Laser supply was setup on the carriage of the flume wall and CCD camera capture the particle movement on the platform. Injected laser became the planar laser sheet through the filtering optics. Laser sheet met the mirror and changed route to the top of the flume and then laser can emphasize motions of the reflected particles in water (Figure 3.18).

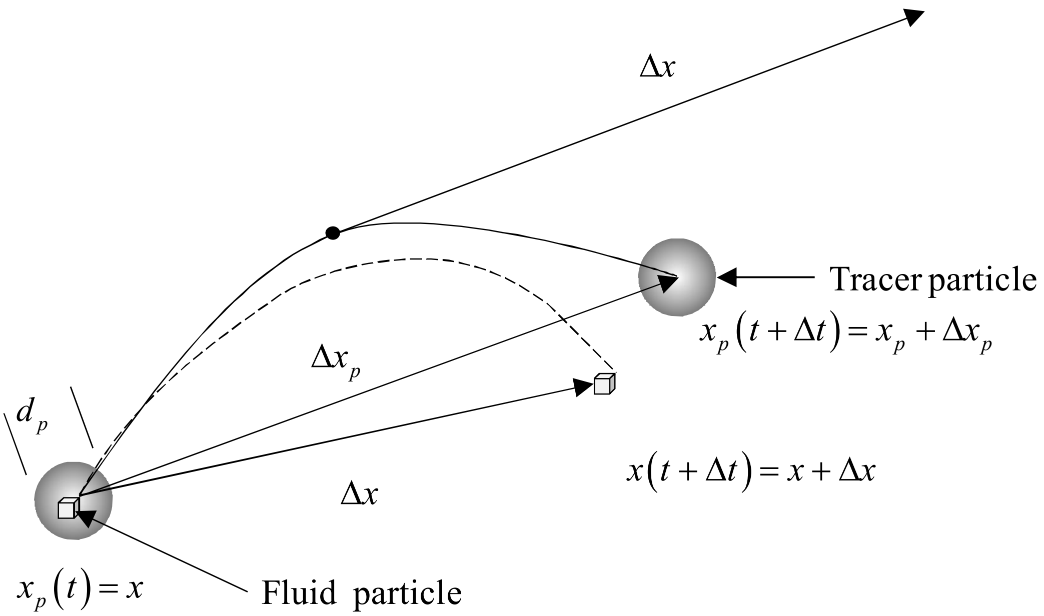

a) Displacement of Marked Particle (Adrian and Jerry, 2010)

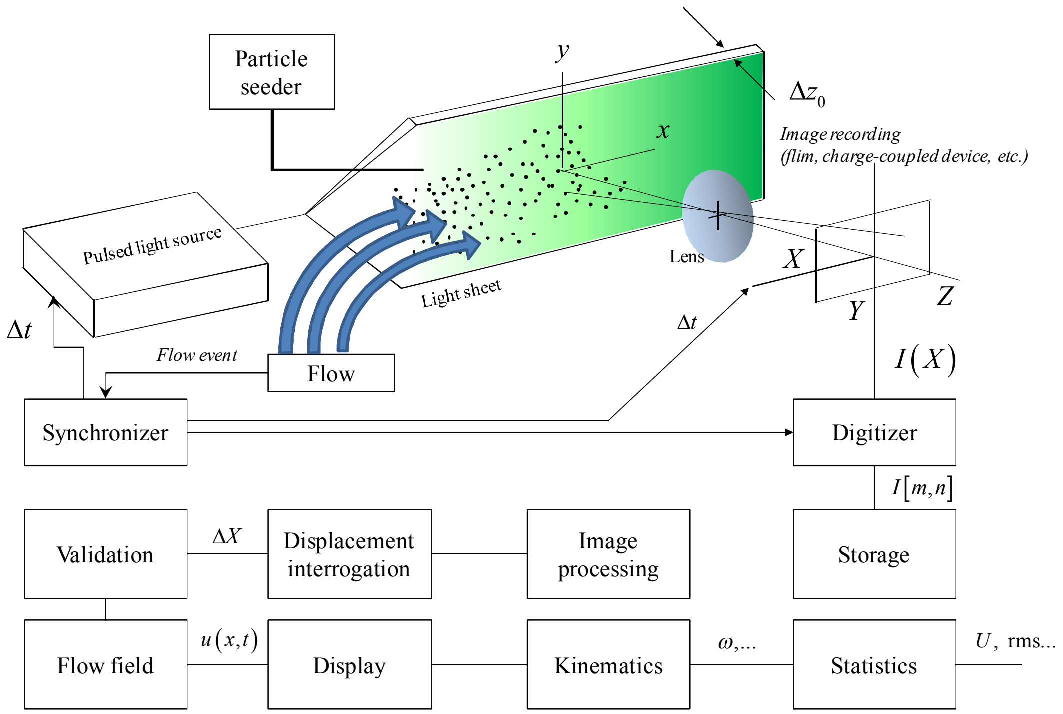

b) Elements and Processes in a Planar Two-dimensional Particle Image Velocimetry

Figure 3.13 Schematic Diagram of the PIV Measurement and Its Processing

Specification: Wavelength(532 nm); Energy (135 mJ); Repetitation Pulse Rate (15 Hz); Pulse Duration (6~9 ns); Energy Stability (±3%); Timing Jitter (±2 ns); Beam Diameter (5 mm)

Figure 3.14 Photo and Specifications of PIV Laser Supply

Specification: Spherical Lens (FL= 500mm & 1000mm); cylindrical lenses (FL= -25 & -15 mm); Divergence angle (14, 25 degrees)

Figure 3.15 Photo and Specifications of Laser Filtering Optics

Specification: Computer control; External standalone type; Time Resolution(1 ns); Time Base (100MHz); External Trigger (TTL input: for phase-locked or single-trigger events); Communication (RS-232 to computer)

Figure 3.16 Photo and Specifications of PIV Synchronizer

Specification: Resolution (4M pixel resolution: 2048 x 2048); Pixel Size (7.4um x 7.4um); CCD Temperature (40°C); Dynamic Range (12-bit); Frame Rate (16 fps in Frame Straddling Mode); Frame Straddling Time (200 ns); Spectral Range (350 to 740nm); Quantum Efficiency (57 %); Binning Factor (1 to 12, horizontal and vertical); Protection Mask (Integrated protection mask for the CCD output circuit); Camera Interface (64-bit camera link); Included Lens(F-mount, Nikon 50mm F1.8 lens), Interface cables

Figure 3.17 Photo and Specifications of CCD Camera

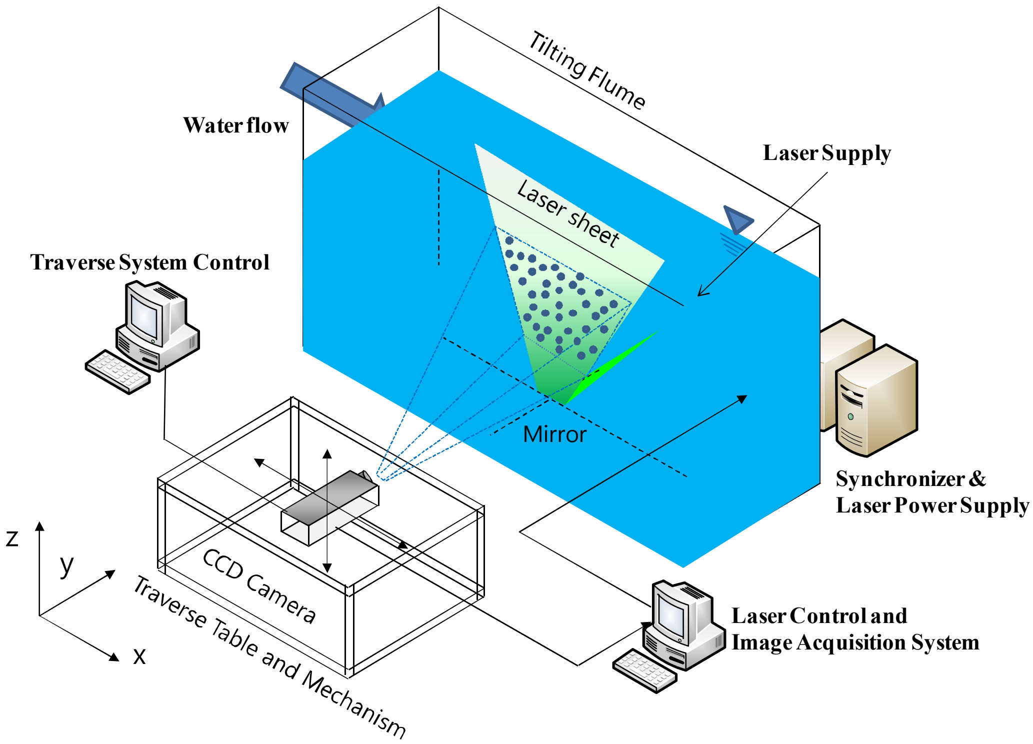

Figure 3.18 Schematic Diagram of PIV Arrangement and Measurement

3.2.2 Experimental Conditions

The experimental conditions were consisted of two parts. The first part is preliminary test of flow measurement with abrupt change of bed elevation and roughness. Second one is scour test with no sediment supply from the upstream with two median sizes of sediment particle (0.6 and 1.2 mm). Additional information of each experimental conditions were explained in following chapters in detailed. Flow conditions of all experimental cases were described in Table 3.2.

3.2.3 Experimental Procedure

During scour tests, bed profiles at each time step were measured with Vectrino along the centerline of the flume. Measuring grid sizes of stream-wise direction were from 2 to 10 cm with consideration of noticeable change of bed elevations. Especially in the region of abrupt change of bed elevation, such as deposition ridge, grid sizes were smaller than in the region of gradually changed bed elevation. Dimensions of scoured hole, which were described in previous chapter 2, were converted from the data of bed profiles and continuously were measured until minimum value of bed elevation equals flume bottom elevation or gradient of minimum value of bed elevation nearly equals zero. At the moment of the upper condition (η_{min}= -$\eta_{initial}$ or $\Delta\eta\approx 0$), 3-D flow velocity werer measured along the centerline. Measuring grid sizes of water-depth direction were 2 to 100 mm with based on the velocity fluctuation. 2-D mean flow velocity were used to describe the flow separation and recirculation in the scoured hole. And also distribution of turbulent properties were used to describe the turbulent shear layer and reattachment length scale in the scoured hole.

Table 3.2 Experimental Conditions of Scour Test

case number	Q (m^3/s)	h_0 (m)	d_{50} (mm)	U_0 (m/s)	Fr (-)	Re ($*10^5$)	T (hr.)
Q20h120d12	0.020	0.120	1.2	0.28	0.30	0.24	345
Q30h150d12	0.030	0.150	1.2	0.33	0.34	0.33	314
Q30h120d12	0.030	0.120	1.2	0.42	0.45	0.36	434
Q35h120d12	0.035	0.120	1.2	0.49	0.53	0.42	142
Q35h144d12	0.035	0.144	1.2	0.41	0.42	0.39	510
Q30h145d12	0.030	0.145	1.2	0.35	0.35	0.34	717
Q20h125d06	0.020	0.125	0.6	0.27	0.24	0.24	700
Q35h120d06	0.035	0.120	0.6	0.49	0.53	0.42	120
Q35h150d06	0.035	0.150	0.6	0.39	0.32	0.39	330
Q32h120d06	0.030	0.150	0.6	0.44	0.49	0.38	200

In addition, as mentioned in chapter 2.3, three dimensional flow velocity near the scoured bed (z= 2 mm) were measured to calculate the bed shear stress. Data of Reynolds shear stress ($\overline{u'w'}$) from were converted into the bed shear stress ($-\rho\overline{u'w'}$) and also compared with critical shear stress from the Shields diagram.

Meanwhile, all data of the 3-D mean and turbulent flow were estimated with using ensemble averaged with based on the maximum values of integral time scale, which can be caluculated with auto-correlation function of instantaneous velocity data as mentioned in chapter 2. As mentioned previously, undesired cyclic fluctuation and despiked values of instantaneous flow velocity could be stabilized and converted into the reliable data (Figure 3.19).

Size of particle in this experiments were selected with consideration of field conditions in 4 major river basins. Lee and Son (2011) measured the hydrological conditions and hydraulic characterstics in 4 major river basins (18 rivers and 37 sites) and estimated values of tractive forces. Median size of the bed materials in 15 sites (41 %) from 37 sites was in the ranges of ± 50 % and the values of the sedimentological diameter (D_*) of 25 sites (67.6 %) in 37 sites were in the ranges from 1 to 200. And the results of the sieve analysis of used bed materials in this study were in the ranges of distributions of Lee and Son (2012) (Figure 3.20).

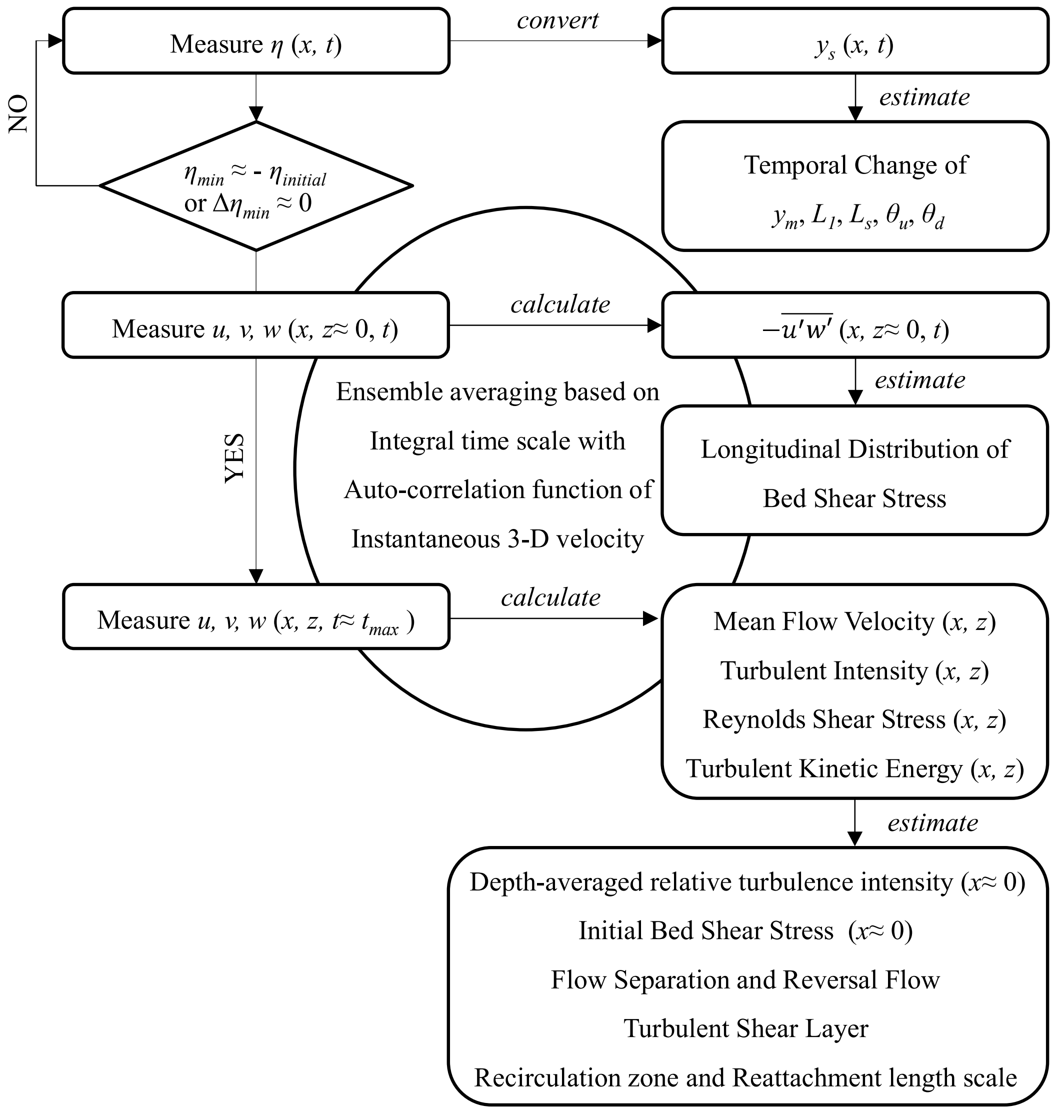

Figure 3.19 Flow Chart of Data Acquisition

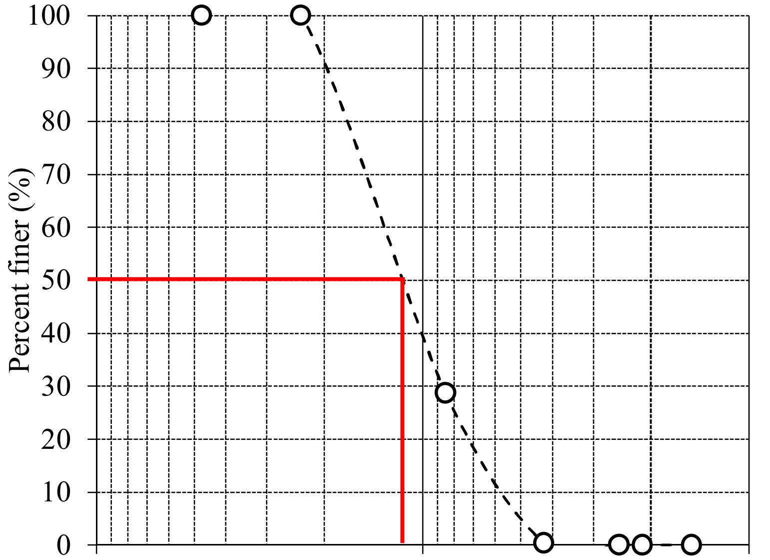

a) case B (d_{50}= 1.2 mm)

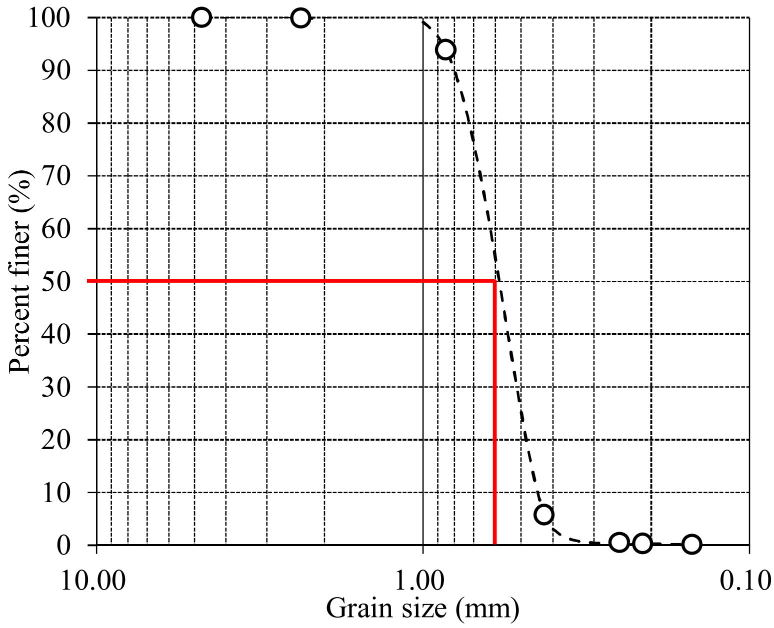

a) case C & D (d_{50}= 0.6 mm)

Figure 3.20 Results of the Sieve Analysis

CHAPTER 4

EXPERIMENTAL RESULTS AND ANALYSIS

4.1 Flow and Turbulence Structures at the Transition

4.1.1 Characteristics of Mean and Turbulent Flow

To analyze the dominant factors on local scouring, which were previously revealed, appropriate analysis of flow and turbulent characteristics with variation of bed elevation. In this chapter, preliminary test in the backward-facing step flow was conducted with single point measurement along the centerline. Sampling frequency of ADV and total duration of flow measurement were 50 Hz and 30 seconds, respectively at each measuring point. And then 3-D flow and turbulence at the stream-wise direction transition (x= 0 m) were measured and analyzed with previously suggested methods.

a) Preliminary Test with Step Models

An acryllic model of backward-facing step flow was setup in flume. 3-D flow velocity at 4 sections were measured (Figure 4.1-a). Heights of the first step and second one were 0.035 m and 0.2 m, respectively. ADV was setup on the transversely middle of the auto-tranverse system and measuring position of the sensor was controlled with the value of the distance from the transimitter (Figure 4.1-b). Flow conditions of this preliminary test were described in Table 4.1. A value of water depth at the section 4 were same as 0.4 m and water discharge of Run-2 was two time as that of Run-1. Therefore values of cross sectional velocity and Froude number of Run-2 were two times as those of Run-1.

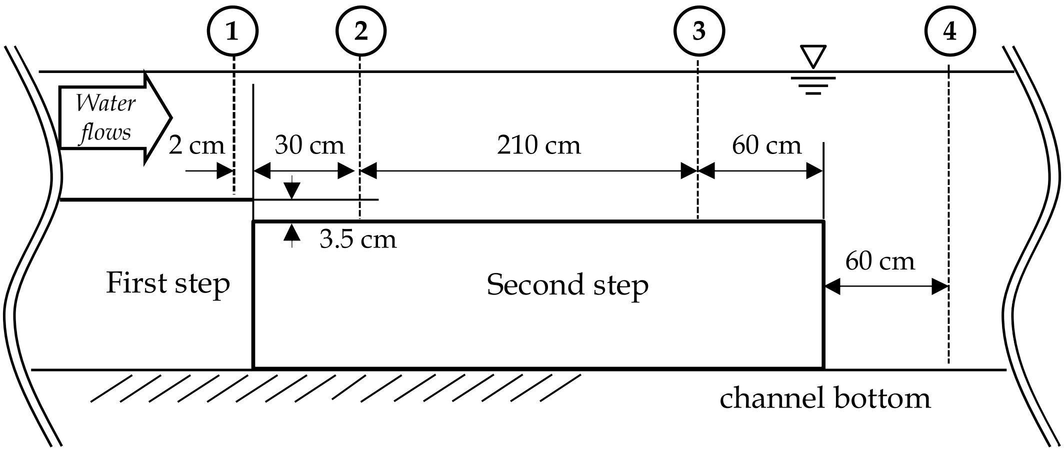

a) **Step Model and Measuring Sections**

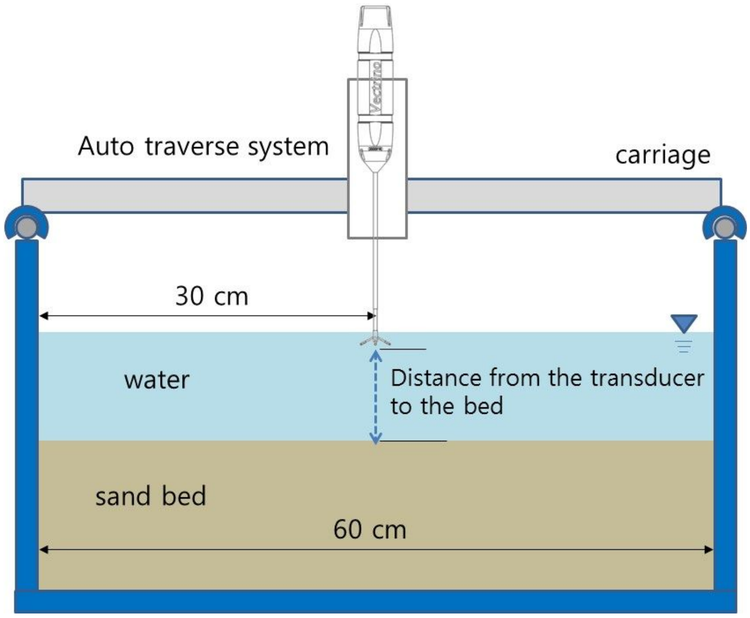

b) **Measuring Setup (Front View)**

Figure 4.1 Schematic Diagram of Step Model and Measuring Setup

Table 4.1 Hydraulic Condition of Step Model Test

Cases	Water discharge from the upstream (m^3/s)	Water depth at the tailgate (m)	Cross sectional velocity (m/s)	Froude number (-)
RUN-1	0.010	0.20	0.167	0.059
RUN-2	0.020	0.20	0.330	0.119

For appropriate analysis of the 3-D flow velocity, vertical distribution of the integral time scale based on the auto-correlation function were determined in Table 4.2. Vertical distance from the bottom, where the largest value were estimated, at section 1 and 2 were mostly near the maximum value of the vertical position. Meawhile maximum values of integral time scale at section 3 were estimated in the middle of the vertical distribution such as from 0.03 to 0.12 m. In case of Run-1, range of the integral time scales were from 0.687 to 8.42 seconds and ranges of Run-2 were estimated from 0.840 to 10.93 seconds (Table 4.2). Integral time scale of stream-wise direction were nearly the maximum among the 3-D direction due to the magnitude of velocity fluctuation.

The first zero crossing time scale and integral time scale were compared in Figure 4.2. And linear relationship between the time to the first zero crossing and integral time scale were decribed as follows:

$$T_i = a_t t_0 + b_t \tag{4.1}$$

where t_0 is time to the first zero crossing from the auto-correlation function of 3-D flow velocity data. And a_t (0.03-0.22) and b_t (0.0003-0.002) were the calibration coefficients. With this values and distributions of integral time scale, we can decide how long enough measure the instantaneous flow velocity data with consideration of turbulence fluctuations and undesired excessive values of flow velocity, such as over 10 times of spatial mean velocity suddenly or over 10 times of negative values of stream-wise velocity. Also mentioned previously, mis-alignment and configuration of ADV can be modified with this consideration. In this study, 1500 samples in 30 second measuring duration is long enough than 5-10 times of the integral time scale at least.

Table 4.2-a) Estimation of Integral Time Scale (Run1_section1)

depth (m)	Integral time scale (s)			Time to the first zero crossing (s)		
z	T_u	T_v	T_w	t_u	t_v	t_w
0.003	0.591	0.213	0.044	10.26	1.54	0.14
0.005	0.420	0.977	0.082	7.14	9.46	0.56
0.01	1.09	7.45	0.299	8.94	50.2	1.5
0.015	2.96	0.452	0.317	19.7	2.74	1.38
0.02	0.751	1.020	0.328	4.86	12.9	1.44
0.025	3.86	0.273	0.273	31.7	1.04	2.04
0.03	1.216	0.270	0.261	8.78	0.98	1.16
0.035	1.33	1.681	0.252	9.58	17.3	1.66
0.04	3.11	1.002	0.240	19.74	11.58	0.82
0.045	2.08	0.315	0.271	12.96	1.12	1.76
0.05	2.01	0.287	0.198	18.66	1.34	0.6
0.06	1.875	0.304	0.273	16.3	1.24	1.34
0.07	7.91	0.263	2.76	41.9	1.26	26.7
0.08	0.280	0.305	0.415	1.28	1.36	1.42
0.09	0.315	6.75	0.899	1.2	49.6	5.74
Max.	7.91	7.45	2.76	41.9	50.2	26.7

Table 4.2-b) Estimation of Integral Time Scale (Run1_section2)

depth (m)	Integral time scale (s)			Time to the first zero crossing (s)		
z	T_u	T_v	T_w	t_u	t_v	t_w
0.003	1.371	0.592	0.332	7.1	3.46	1.82
0.005	1.224	0.498	0.354	9.36	2.12	1.86
0.01	0.770	0.454	0.351	4.08	1.7	2.04
0.015	1.176	0.276	0.349	10.14	1.12	1.96
0.02	0.888	0.314	0.285	5.4	1.24	0.98
0.025	0.612	0.206	0.297	1.82	0.72	1.2
0.03	1.193	0.233	0.273	7.2	0.8	0.98
0.035	0.692	0.258	0.260	2.24	1.06	1.24
0.04	0.729	0.197	0.224	3.98	0.84	0.76
0.045	0.997	0.246	0.242	5.22	0.98	0.84
0.05	0.922	0.253	0.255	5.6	1.32	1.04
0.06	1.411	0.299	0.282	8.08	1.12	1
0.07	1.534	0.278	0.225	9.34	1.12	0.9
0.08	0.635	0.251	0.244	4.32	1.82	1
0.09	1.906	0.281	1.410	10.6	1.78	8.98
0.1	0.944	0.249	0.482	6.6	0.96	2.36
0.11	1.757	0.225	0.756	9.26	0.94	6.96
0.12	1.204	0.948	2.165	10.66	11.16	17.8
0.13	1.436	1.668	1.771	11.74	20.3	12.52
Max.	1.906	1.668	2.165	11.74	20.3	17.8

Table 4.2-c) Estimation of Integral Time Scale (Run1_section3)

depth (m)	Integral time scale (s)			Time to the first zero crossing (s)		
z	T_u	T_v	T_w	t_u	t_v	t_w
0.003	3.14	0.709	0.222	16.34	7.52	1.18
0.005	3.97	0.981	0.231	35.32	5.32	1.1
0.01	3.13	0.468	0.229	13.5	3.68	1.94
0.015	2.26	0.641	0.242	8.48	7.74	1.96
0.02	1.421	0.461	0.183	6.92	2.52	0.7
0.025	4.29	0.394	0.215	28.2	1.84	1.08
0.03	8.43	0.421	0.204	38.7	1.42	0.98
0.035	3.27	0.317	0.233	16.5	1.34	1.24
0.04	3.64	0.687	0.361	19.8	4.62	2.38
0.045	2.85	0.336	0.306	15.66	1.30	1.68
0.05	8.09	0.325	0.435	30.7	1.34	5.16
0.06	1.280	0.321	0.346	6.44	1.92	1.68
0.07	7.70	0.306	0.611	28.3	1.32	4.26
0.08	3.71	0.314	0.700	18.5	1.76	5.68
0.09	7.76	0.279	0.303	32.5	1.44	1.06
0.1	5.92	0.297	0.380	24.5	1.42	2.82
0.11	3.85	0.208	0.388	22.4	0.84	2.04
0.12	8.27	0.372	0.293	50.4	2.3	1.06
0.13	7.75	0.301	0.385	28.7	1.44	1.76
Max.	8.43	0.687	0.700	50.4	4.62	5.68

Table 4.2-d) Estimation of Integral Time Scale (Run2_section1)

depth (m)	Integral time scale (s)			Time to the first zero crossing (s)		
z	T_u	T_v	T_w	t_u	t_v	t_w
0.003	0.033	0.047	0.027	0.46	0.9	0.38
0.005	0.032	0.352	0.050	0.5	5.42	0.82
0.01	0.096	2.48	0.112	0.8	24.4	1.26
0.015	0.140	1.491	0.070	1.62	18.36	0.66
0.02	0.103	0.437	0.069	0.78	5.82	0.8
0.025	0.109	1.721	0.068	0.94	20.7	0.98
0.03	0.210	0.237	0.064	3.22	2.56	1
0.035	0.174	0.451	0.064	1.36	6.66	0.52
0.04	0.840	1.152	0.073	12.52	14.12	0.62
0.045	0.123	0.205	0.124	1.04	2.32	2.64
0.05	0.586	0.198	0.066	10.96	2.12	0.64
0.06	0.155	0.137	0.260	2	0.78	3.74
0.07	0.260	0.157	0.458	4.48	0.64	6.1
0.08	0.123	0.119	0.323	1.96	0.5	3.46
0.09	0.112	0.894	1.215	1.12	10.54	13.18
Max.	0.840	2.48	1.215	12.5	24.4	13.18

Table 4.2-e) Estimation of Integral Time Scale (Run2_section2)

Depth (m)	Integral time scale (s)			Time to the first zero crossing (s)		
z	T_u	T_v	T_w	t_u	t_v	t_w
0.003	0.288	0.237	0.114	1.28	1.42	0.62
0.005	0.342	0.191	0.163	3.06	1.02	1.32
0.01	0.316	0.105	0.167	5.12	0.84	1
0.015	0.160	0.074	0.263	1.38	0.54	3.66
0.02	0.166	0.062	0.159	1.36	0.54	1.2
0.025	0.160	0.059	0.146	1.14	0.58	0.78
0.03	0.141	0.054	0.132	1.14	0.44	0.62
0.035	0.190	0.051	0.146	1.06	0.56	0.56
0.04	0.183	0.044	0.130	1.38	0.38	0.52
0.045	0.187	0.068	0.129	1.04	0.6	0.5
0.05	0.220	0.051	0.114	1.78	0.34	0.46
0.06	0.425	0.067	0.144	4.1	0.7	0.76
0.07	0.813	0.097	0.380	12.88	0.54	5.24
0.08	1.384	0.114	0.215	21.4	0.54	1.14
0.09	1.565	0.137	1.905	15.02	0.9	17.06
0.1	1.143	0.120	1.443	12.48	0.74	14.92
0.11	1.008	0.105	0.662	11.3	0.64	7.22
0.12	0.848	0.146	0.622	11.62	1.2	6.82
0.13	0.335	0.867	0.310	3.68	12.4	3.48
Max.	1.565	0.867	1.905	21.4	12.4	17.06

Table 4.2-f) Estimation of Integral Time Scale (Run2_section3)

Depth (m)	Integral time scale (s)			Time to the first zero crossing (s)		
z	T_u	T_v	T_w	t_u	t_v	t_w
0.003	1.946	0.454	0.071	11.18	2.82	0.72
0.005	0.618	1.403	0.076	3.28	19.44	0.62
0.01	3.29	0.881	0.093	19.38	9.46	0.72
0.015	2.34	1.805	0.104	10	19.62	0.74
0.02	4.64	0.373	0.256	23.1	3.38	2.78
0.025	1.600	3.12	0.301	13.1	23.5	4.52
0.03	4.35	3.99	0.441	26.0	36.5	8.62
0.035	1.968	0.285	0.380	8.72	1.2	4.94
0.04	1.942	0.206	0.306	8.84	1	4.22
0.045	4.42	0.181	0.402	23.8	1.06	3.72
0.05	10.93	0.226	3.04	57.8	1.12	46.1
0.06	3.67	0.188	0.607	37.2	0.74	6.76
0.07	9.56	0.202	1.410	47.0	0.96	17.74
0.08	3.90	0.162	1.339	14.8	0.8	12.92
0.09	4.48	0.152	0.208	26.6	1.3	1.22
0.1	3.58	0.165	0.244	24.1	0.92	1.7
0.11	5.90	0.128	1.286	27.9	0.56	14.1
0.12	3.26	0.177	0.178	17.2	1.06	0.76
0.13	1.064	0.145	0.162	6.24	0.68	0.72
Max.	10.93	3.99	3.04	57.8	36.5	46.1

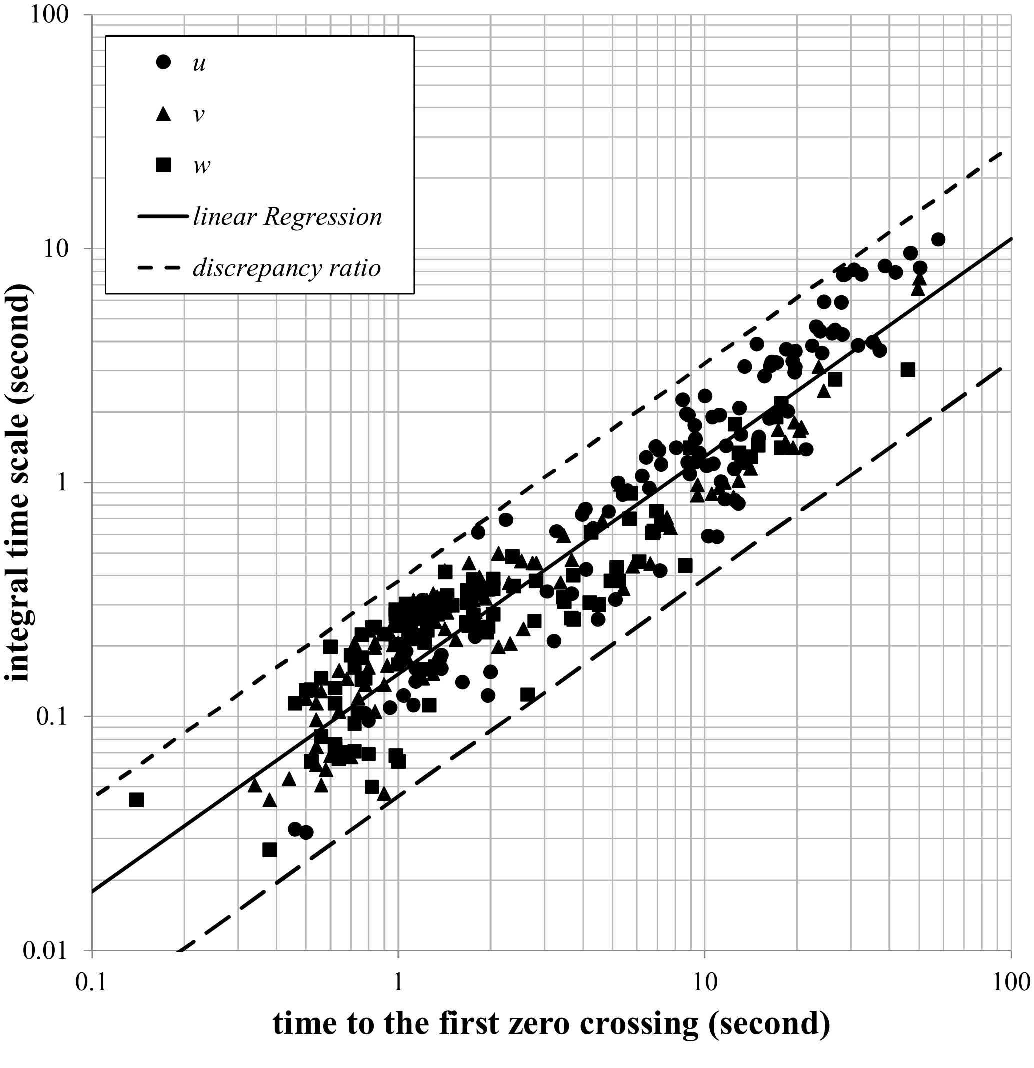

Figure 4.2 Linear Regression between the First Zero Crossing and Integral Time Scale

Ensemble time-averaged values of 2-D (stream-wise and water-depth directional) were plotted with vector arrows in Figure 4.3. Vertical variation of vectors at the first step (height= 0.035 m) were relatively smaller than the other larger step (height= 0.2 m). Because section 2 is not in the range of recirculation zone from the first step due to the longitudinal distance of section 2 (0.3 m) is larger than X_{Re} (0.035*6= 0.21 m). On the other side, section 4 is in the range of recirculation zone from the second step, due to X_{Re} of the second step is approximately 1.2 m. Reversal and backward flow pattern were occurred at the section 4 only. However the magnitude of flow is drastically smaller than vertical upper layer from the channel bottom (Figure 4.3). Additionally largest size of vortex due to the backward facing step, can be developed longitudinally from 6 to 17 times of water depth (Jovic and Driver, 1995; Jovic, 1996).

Figure 4.3 showed water-depth directional variation of the stream-wise direction velocity at each 4 sections. u values were normalized with cross-sectional averaged velocity U_0 at each sections and U_0 value of the Run-1 is mostly half of Run-2. At the beginning of the step model, i. e. section #1, distributions of u showed a relatively large difference between Run-1 and 2 along the water depth. From the section #2, vertical distributions were getting similar firstly near the bed. Variations of the upper part along the water depth (z> 0.07 m) were larger than lower part of the water depth (z< 0.07 m). Behind the biggest step, i. e. at section #4, values of u/U_0 were shown mostly same along the water depth, even there were backward flow. Variation of water-depth direction velocity, w were relatively not larger than those of stream-wise velocity (Figure 4.5). Values of normalized water-depth direction velocity, w/U_0 were slightly negative at section #1, and mostly negative at section #2 and #3. And relatively larger negative values of w/U_0 were observed at section #4. Values of w/U_0 (z) made reversal flow with u/U_0 as plotted in Figure 4.3 and mentioned previously.

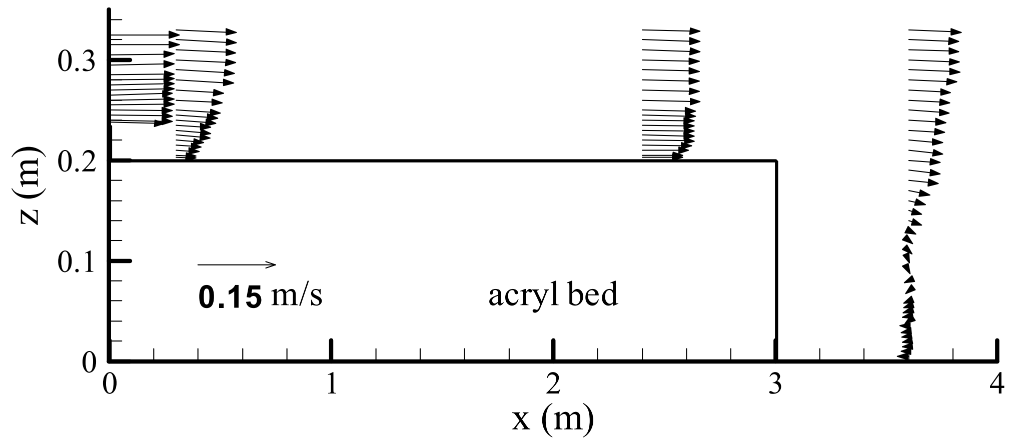

a) Run-1

(Q= 0.01 m^3/s, h_0= 0.4 m)

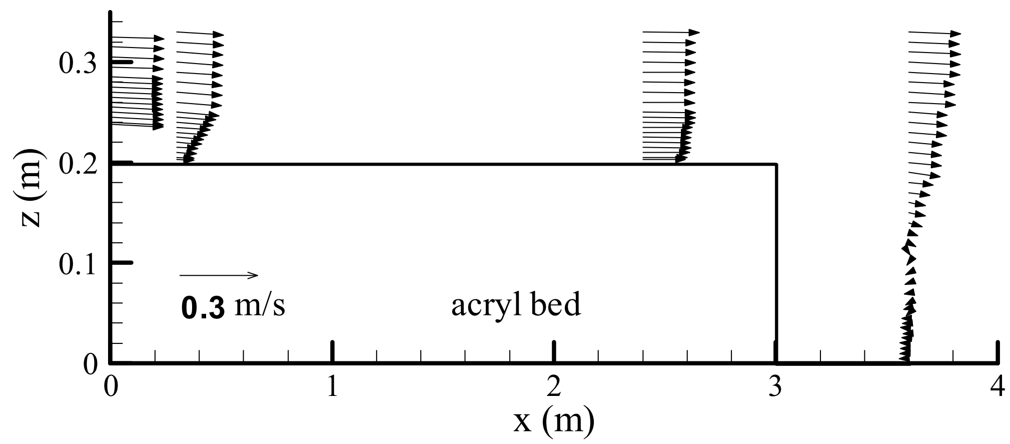

b) Run-2

(Q= 0.02 m^3/s, h_0= 0.4 m)

Figure 4.3 Two-dimensional Vector Profiles in Backward-facing Step Flow

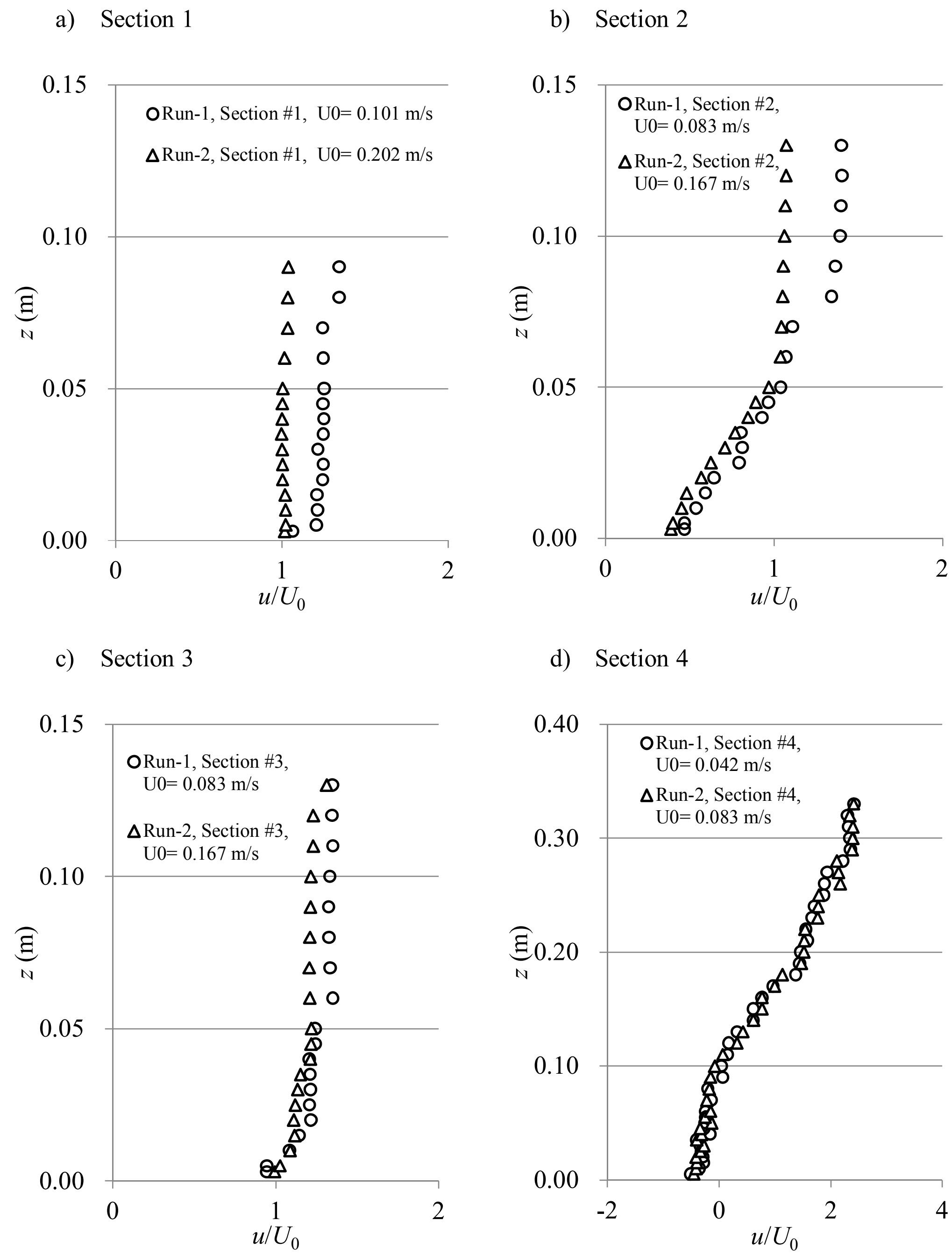

Figure 4.4 Vertical Distributions of Stream-wise Direction Velocity in Backward-facing Step Flow

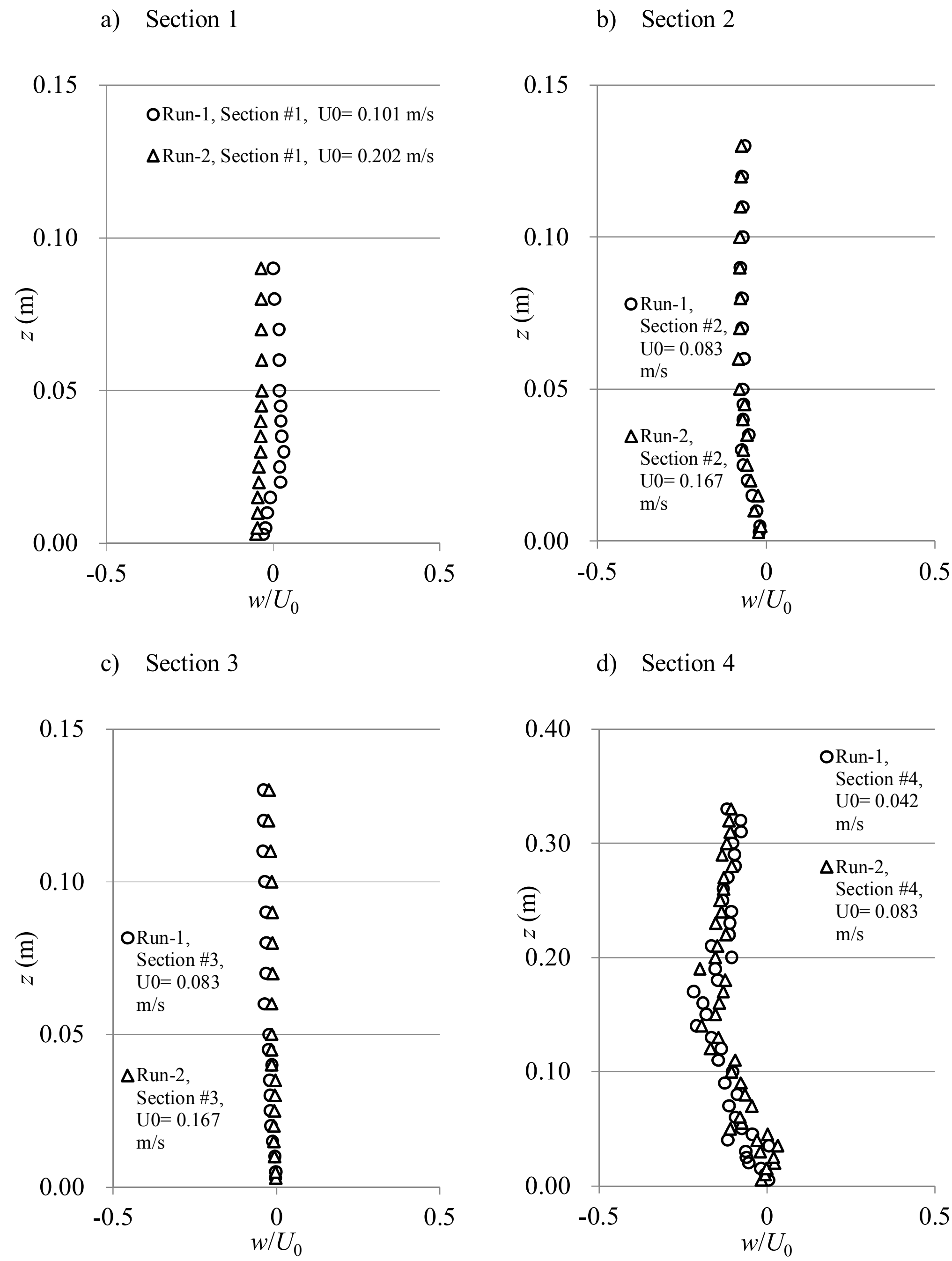

Figure 4.5 Vertical Distributions of Water-depth Direction Velocity in Backward-facing Step Flow

With data of stream-wise directional velocity, LOW method (Eq. 2.19) were applied to estimate the shear velocity at each sections of two cases. Values of estimated shear velocity of Run-2 at each sections were mostly twice of those of Run-1. And also values of calibration coefficient were varied from 2.0 to 7.0 with logarithmic distribution of normalized velocity and distance from the channel bed.

Figure 4.7 and 4.8 showed the vertical distributions of stream-wise and water-depth directional turbulence intensity, which were normalized with U_0, respectively. As mentioned in previous chapter, k_x/U_0 and k_z/U_0 at section #2 were not well-distributed due to the location of recirculation zone of the first step. And those values at section #3 were shown that the turbulence was only due to the bed roughness. As resulted previously, the location of section #4 was in the recirculation zone of the second step. Therefore location of maximum values of k_x/U_0 and k_z/U_0 were occurred in the middle of water depth, 0.17 m from the channel bed (43 % from the bed) and gradually decreased toward the water surface and channel bed. Because values of turbulent kinetic energy is dominantly affected by the stream-wise direction turbulence intensity, Distributions of k/U_0 showed a similar distributions of k_x/U_0 (Figure 4.9). And values of k/U_0 of Run-2 showed approximately twice of those of k/U_0 of Run-2 along the water depth. Especially turbulent shear layer in the vicinity of the second step could revealed with excessive values of k/U_0 of Run-1 and Run-2. Figure 4.10 showed the comparisons of Reynolds Shear Stress, which were normalized with negative values of U_0 at each sections. Values of $-\overline{u'w'}/U_0$ at section #1 were represented with opposite direction of water flow, due to the approaching flow, but those of the other sections were not. Figure 4.11 showed the estimation of bed shear velocity with RSS method (Eq. 2.38 and 2.39). And the estimated values of bed shera velocity were compared in Table 4.3 and Figure 4.11.

a) Run-1 (*Q*= 0.010 cms)

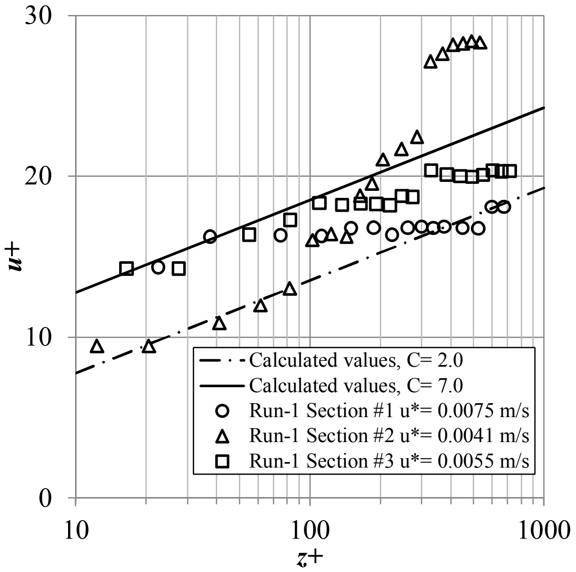

b) Run-1 (*Q*= 0.020 cms)

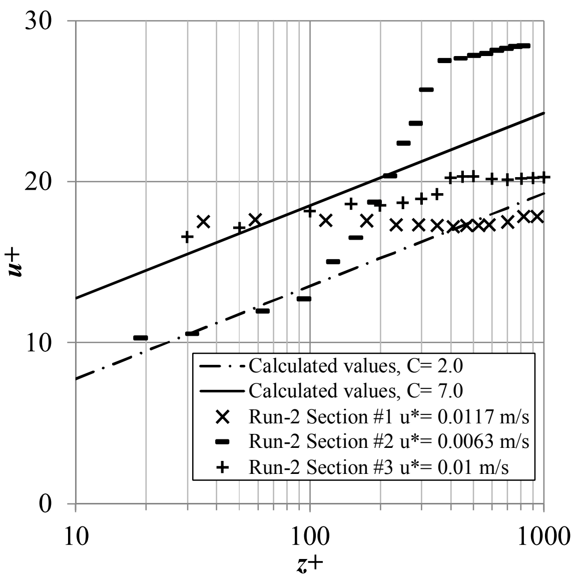

Figure 4.6 Estimation of Bed Shear Stress with LOW Method

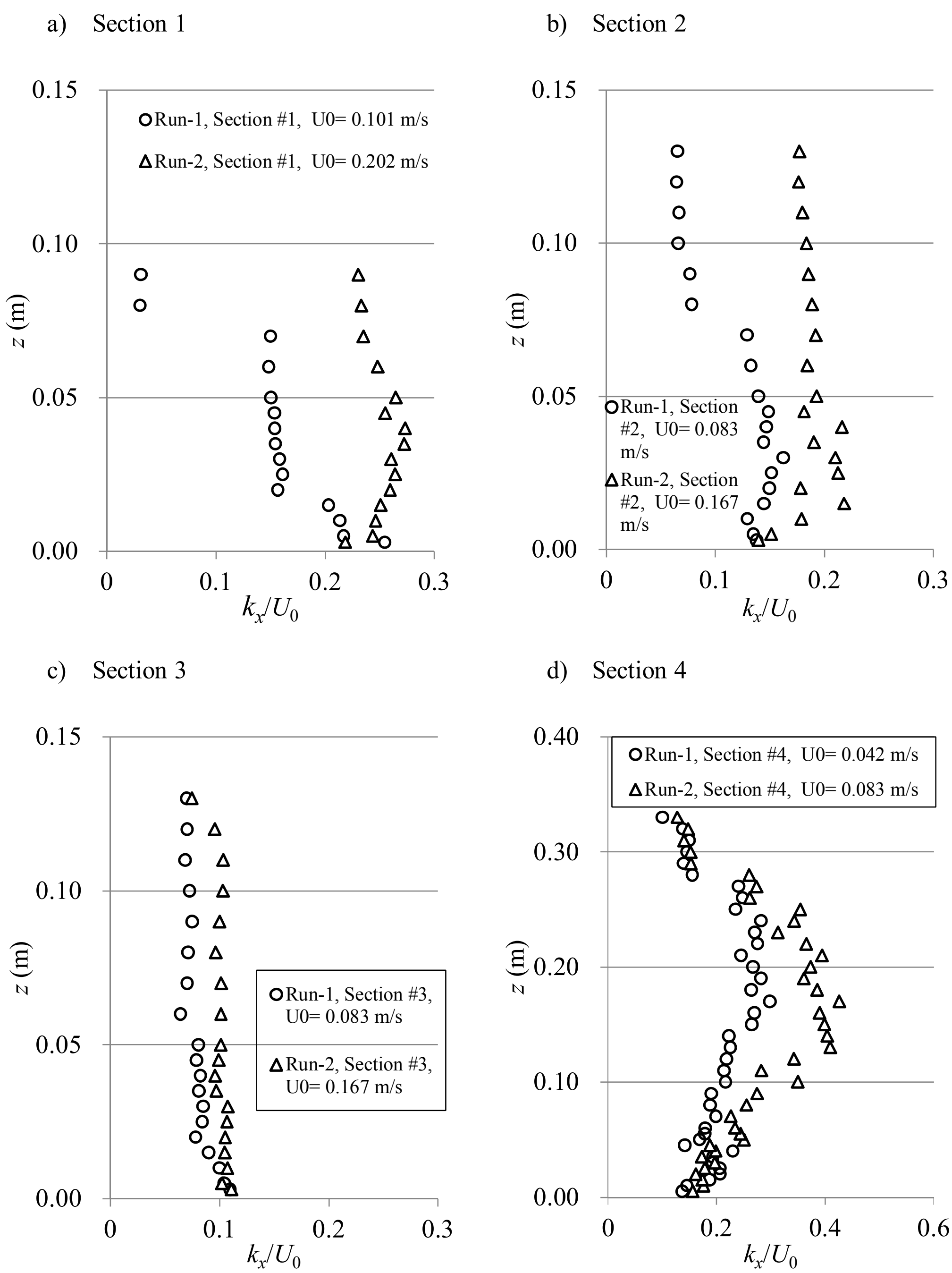

Figure 4.7 Vertical Distributions of Stream-wise Turbulence Intensity in Backward-facing Step Flow

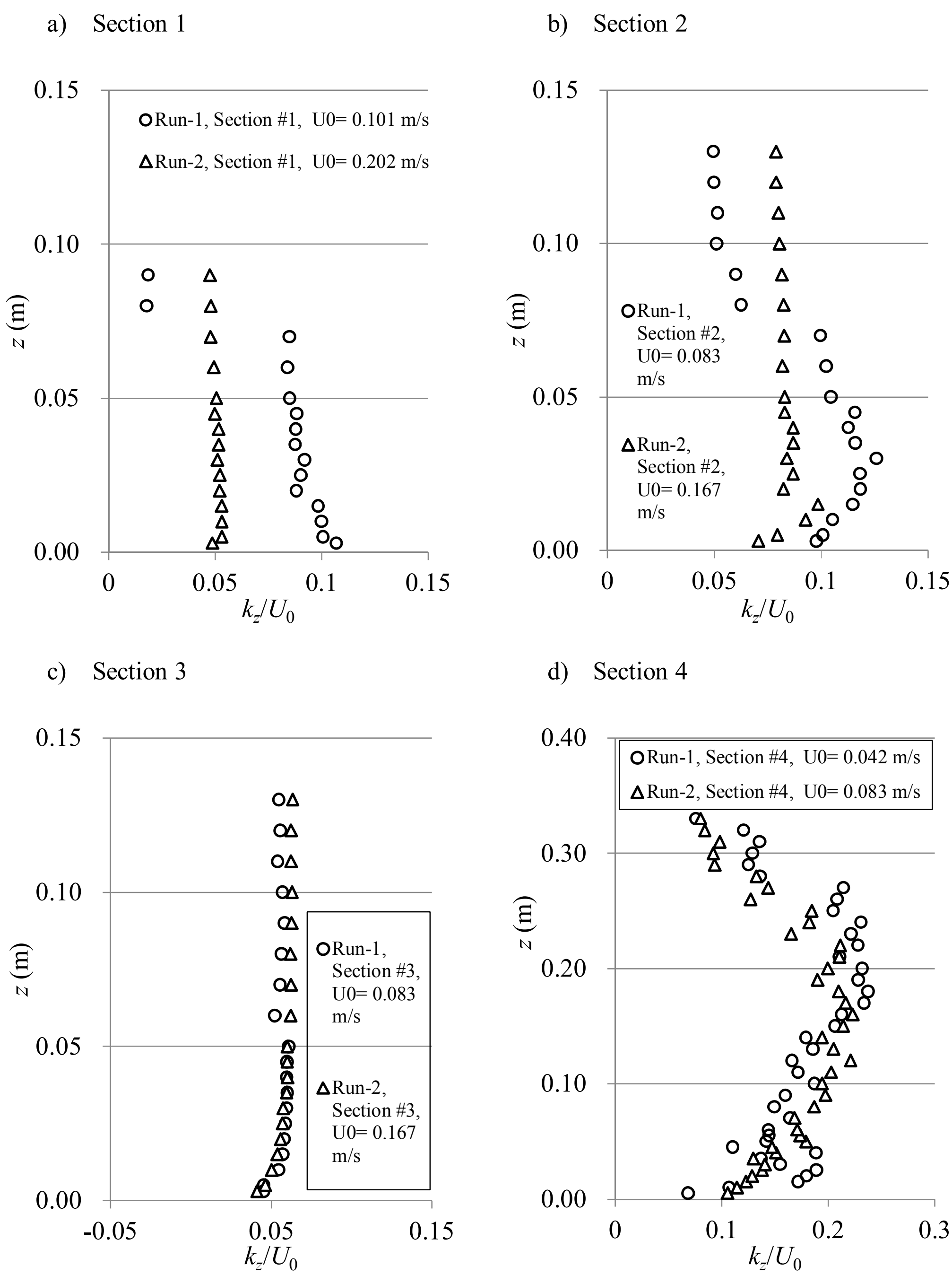

Figure 4.8 Vertical Distributions Water-depth direction Turbulence Intensity in Backward-facing Step Flow

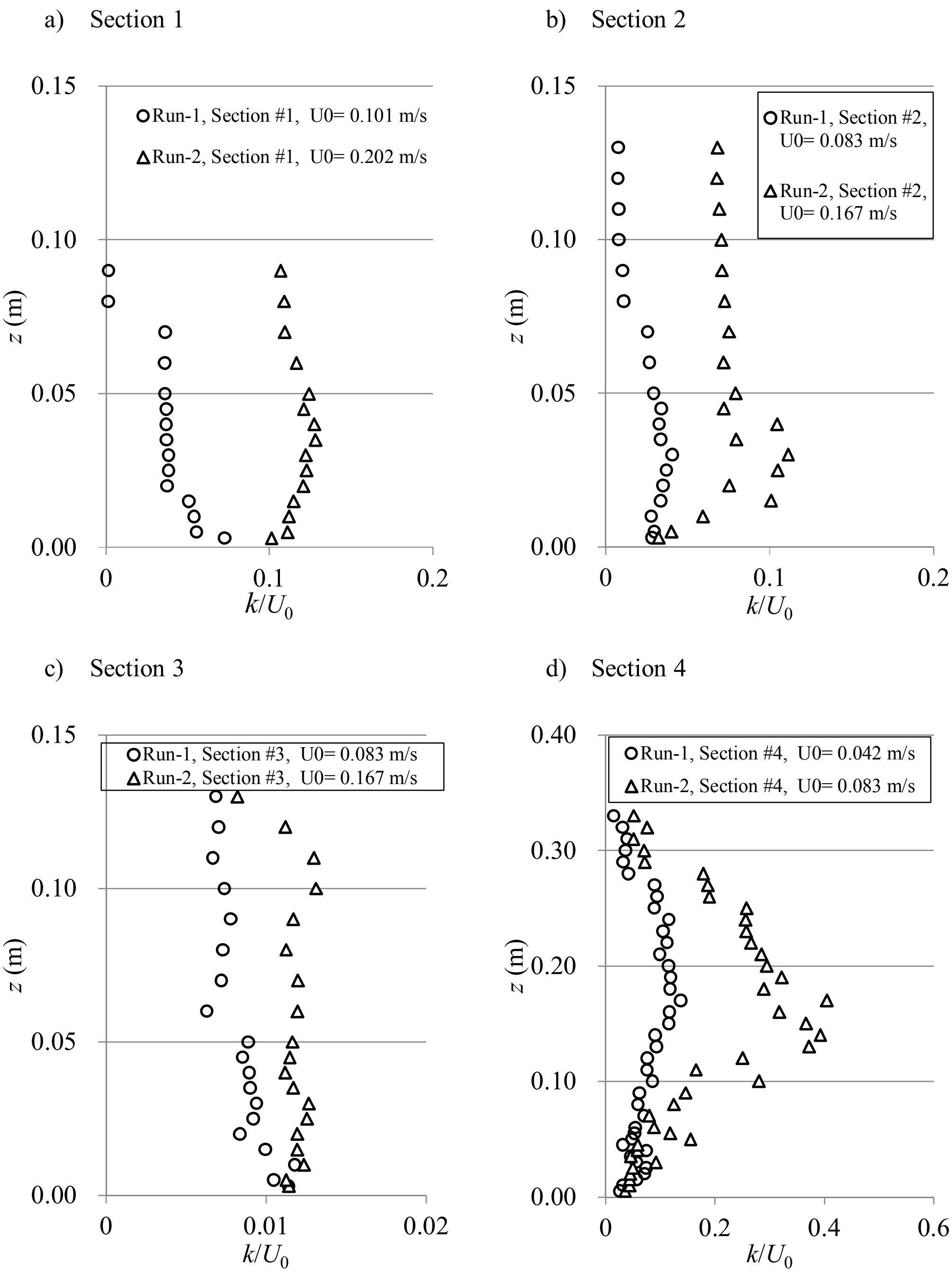

Figure 4.9 Vertical Distributions of Turbulent Kinetic Energy in Backward-facing Step Flow

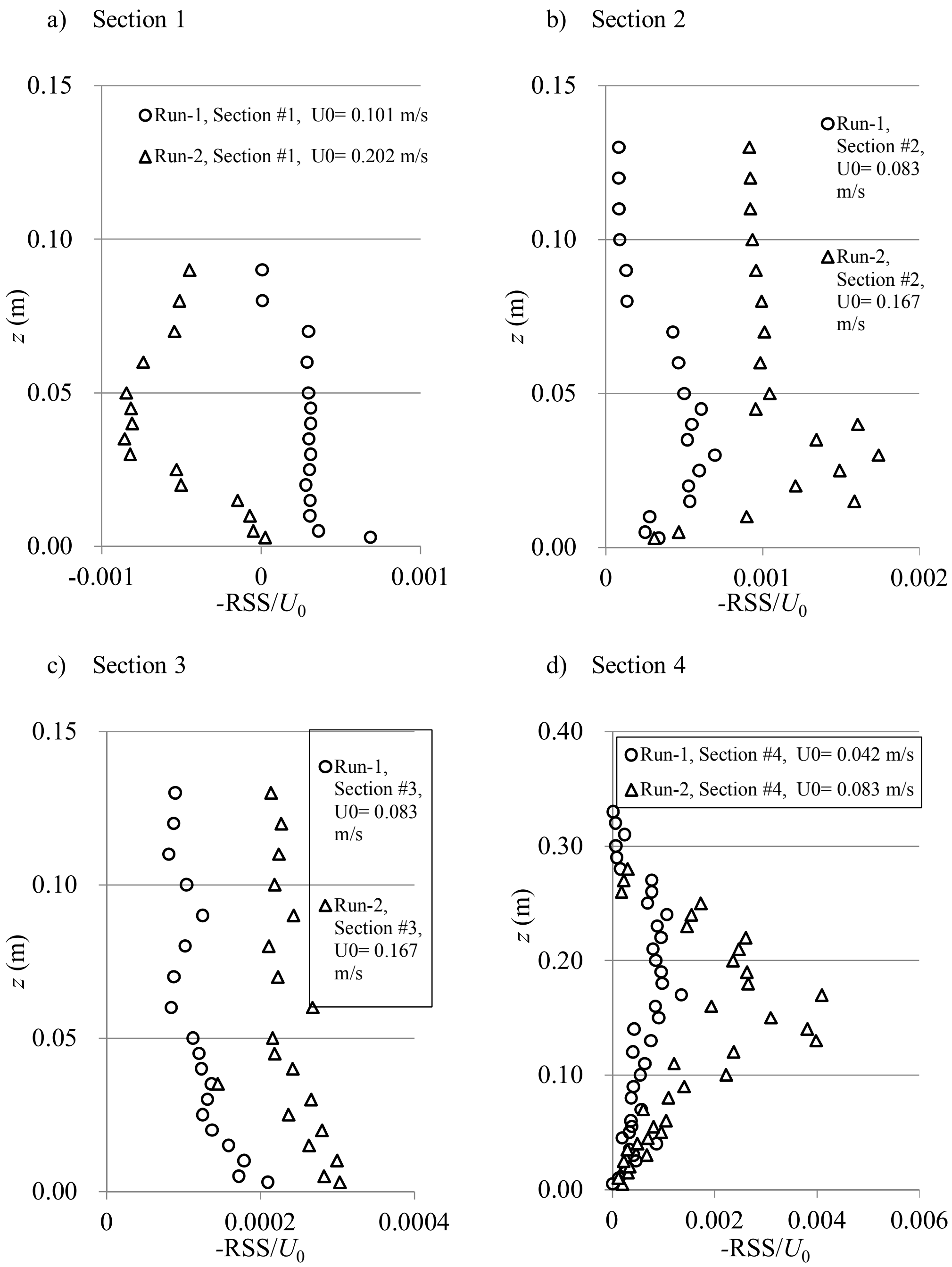

Figure 4.10 Vertical Distributions of Reynolds Shear Stress in Backward-facing Step Flow

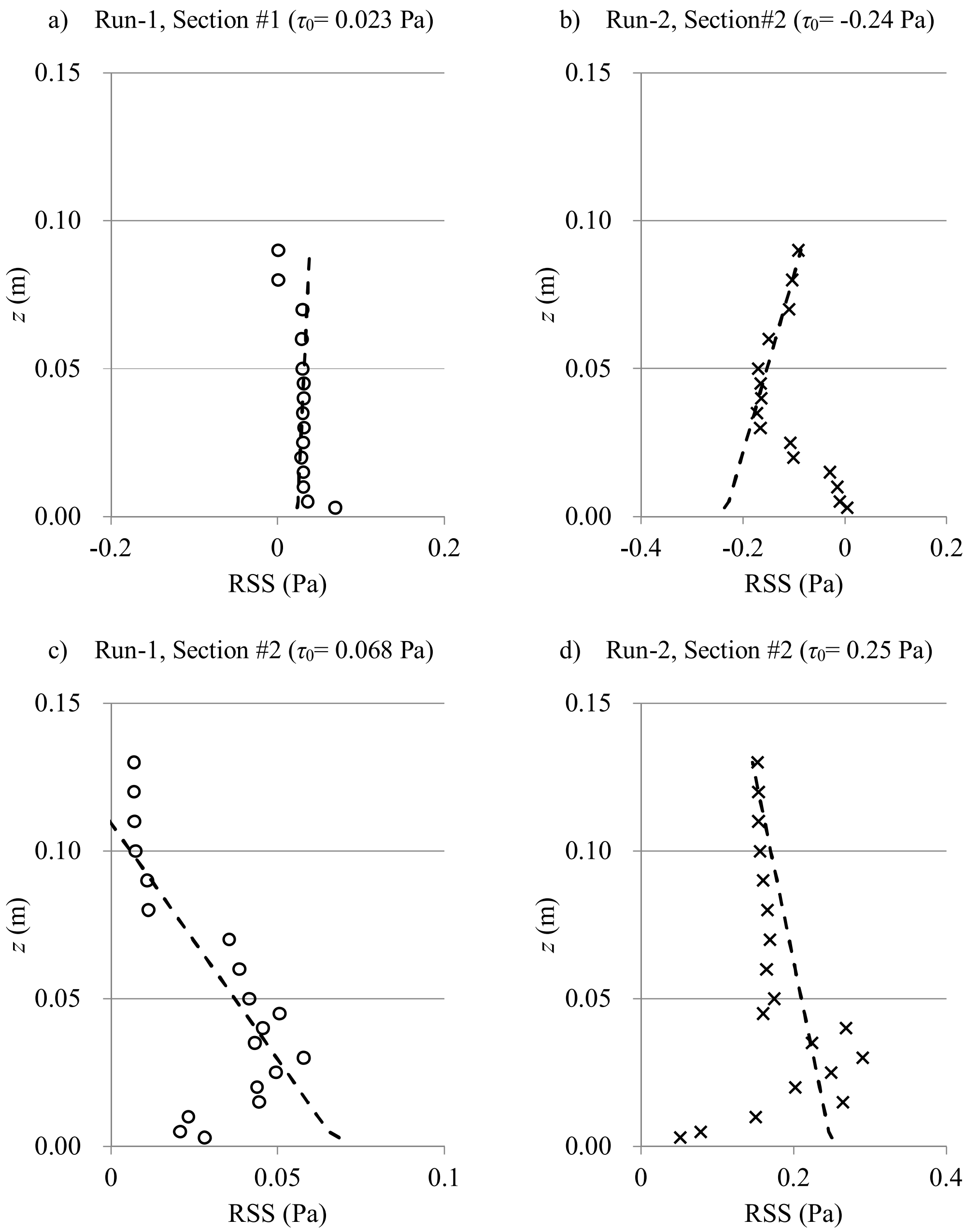

Figure 4.11 Estimation of Bed Shear Stress with RSS method (Run-1) in Backward-facing Step Flow

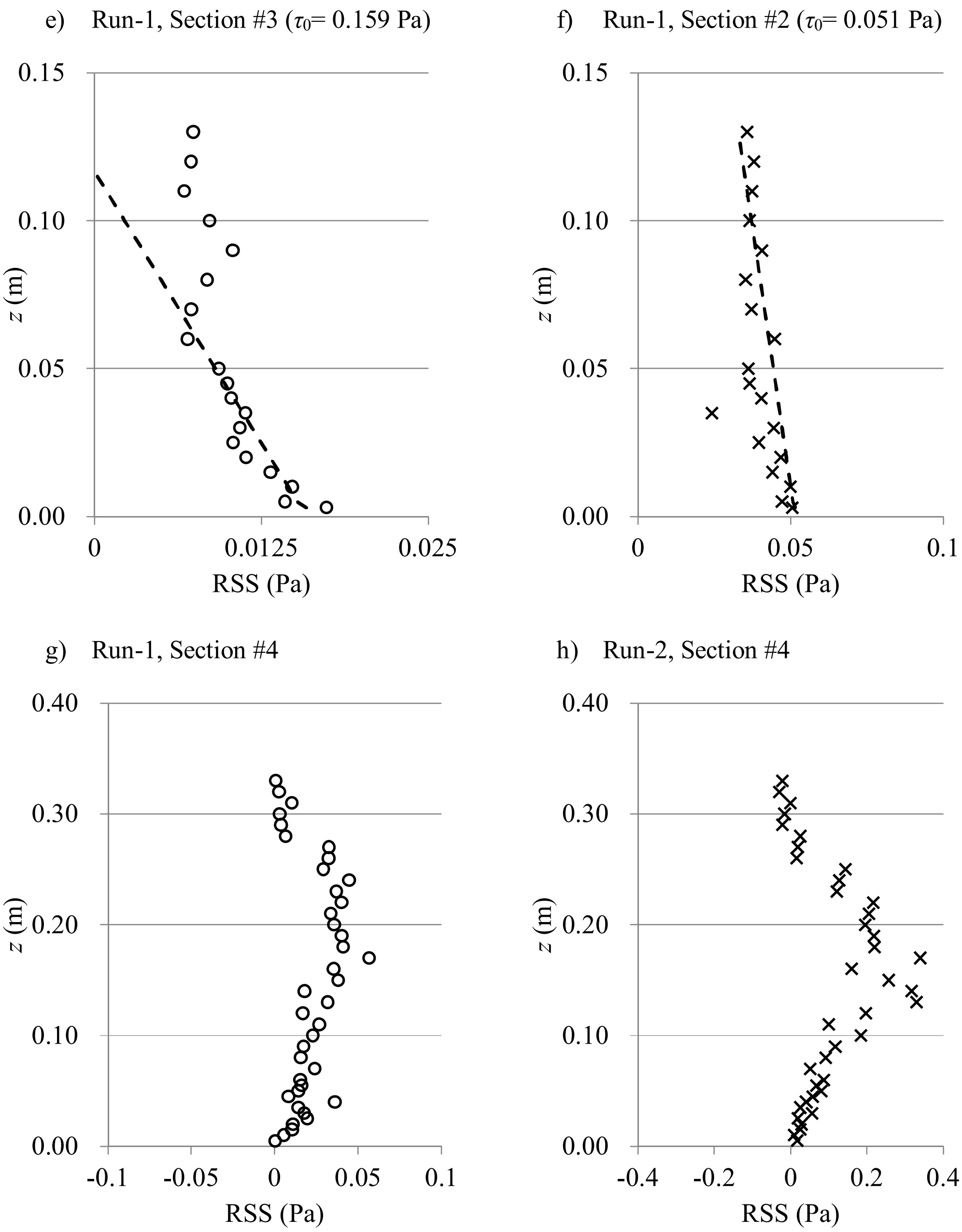

Figure 4.11 Continued

Table 4.3 Comparison of Bed Shear Stress with two Methods in Backward-facing Step Flow

x (m)	Reynolds Shear Stress method (Pa, extrapolation of $-\rho\overline{u'w'}$)		Log Law method (Pa, using shear velocity)	
	Run-1	Run-2	Run-1	Run-2
-0.002	0.023	-0.24	0.0548	0.1369
0.3	0.070	0.25	0.0169	0.0397
2.4	0.159	0.051	0.0305	0.100
3.6	-	-	-	-

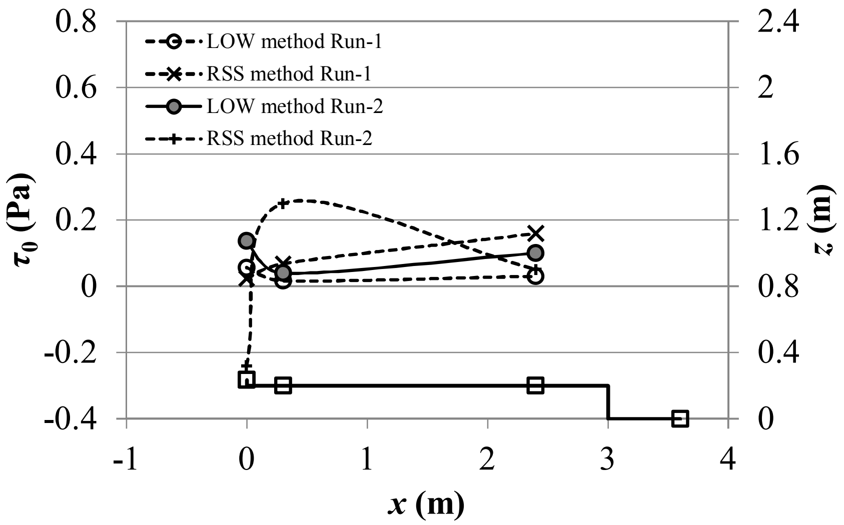

Figure 4.12 Longitudinal Distribution of Bed Shear Stress on Backward Facing Step

b) Mean and Turbulent Flow at the Longitudinal Transition

It is known that the one of the most important dominant factors on local scouring is distribution of mean and turbulent flow at the longitudinal transition (x= 0 m). Especially depth-averaged relative turbulence intensity, r_0 has the properties of flow and turbulence characteristics, which can be determined by the bed roughness or geometry of hydraulic structures at the upstream. Therefore, measurement of 3-D flow velocity of each 10 cases at the longitudinal transition were conducted with using the Vectrino and analyzed (Table 4.4). Configurations of measurement were same as the preliminary test with step models. And experimental setup was schematized in Figure 4.13. A size of measuring interval (Δz) is 2 mm and total range of measurement is from 2 mm to 36 mm from the bed.

Figure 4.14 showed the vertical variation of the stream-wise direction velocity based on the logarithmic distribution. And normalized values of stream-wise direction velocity were plotted in Figure 4.15 with values of coefficient, C, which was varied from 4 to 9 in Eq. 2.19. Normalized values of turbulent kinetic energy (= TKE/u_*^2) were plotted in Figure 4.16. All of the cases were good fit with Eq. 2.34 (Figure 4.17). Also Normalized values of Reynolds shear stress (= -RSS/u_*^2) were plotted in Figure 4.18. And maximum value of each cases were distributed from 4 to 10 % of water depth (Figure 4.19).

c) Initial Bed Shear Stress

The values of bed shear velocity at each cases were estimated by using the Eq. 2.19, 2.34, and 2.38, respectively. And bed shear stress (=ρu_*^2) were calculated and compared with those of different estimating method. Values of those with using the LOW method were represented the reliable data against the others. Also LOW method were used for extrapolation of free surface flow velocity, U_{free} and estimation of turbulent layer thickness,

Table 4.4 Experimental Conditions of Flow Test at Longitudinal Transition

case number	Q (m^3/s)	h_0 (m)	U_0 (m/s)	Fr (-)	Re ($*10^5$)
Q15h320	0.020	0.120	0.208	0.192	0.250
Q20h320	0.030	0.150	0.278	0.256	0.333
Q20h350	0.030	0.120	0.222	0.183	0.333
Q30h320	0.035	0.120	0.417	0.384	0.500
Q30h345	0.035	0.144	0.345	0.289	0.500
Q30h350	0.030	0.145	0.333	0.274	0.500
Q32h320	0.020	0.120	0.444	0.410	0.533
Q35h320	0.035	0.120	0.486	0.448	0.583
Q35h344	0.035	0.150	0.405	0.341	0.583
Q40h320	0.030	0.150	0.556	0.512	0.667

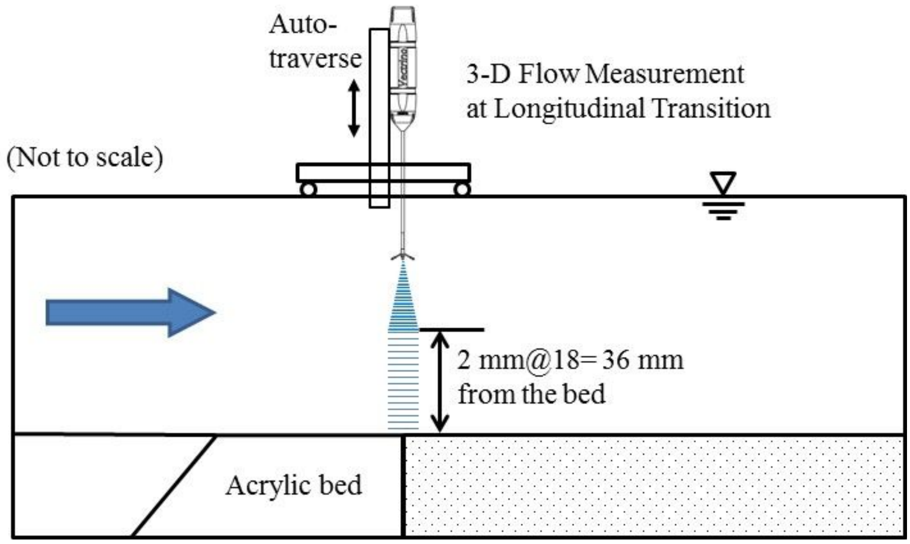

Figure 4.13 Schematic Diagram of 3-D Flow Measurement at Longitudinal Transition

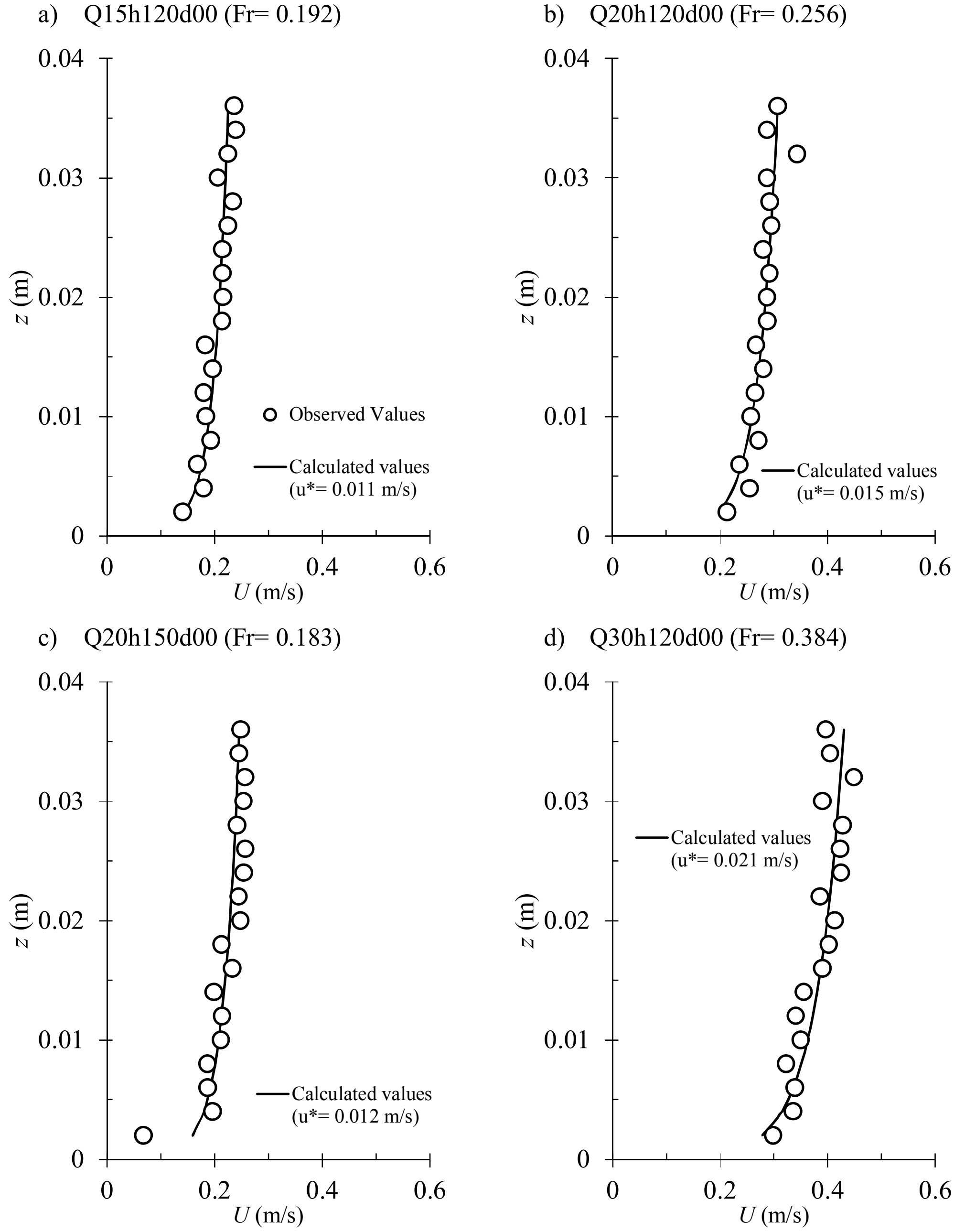

Figure 4.14 Vertical Distribution of Stream-wise Velocity at Longitudinal Transition

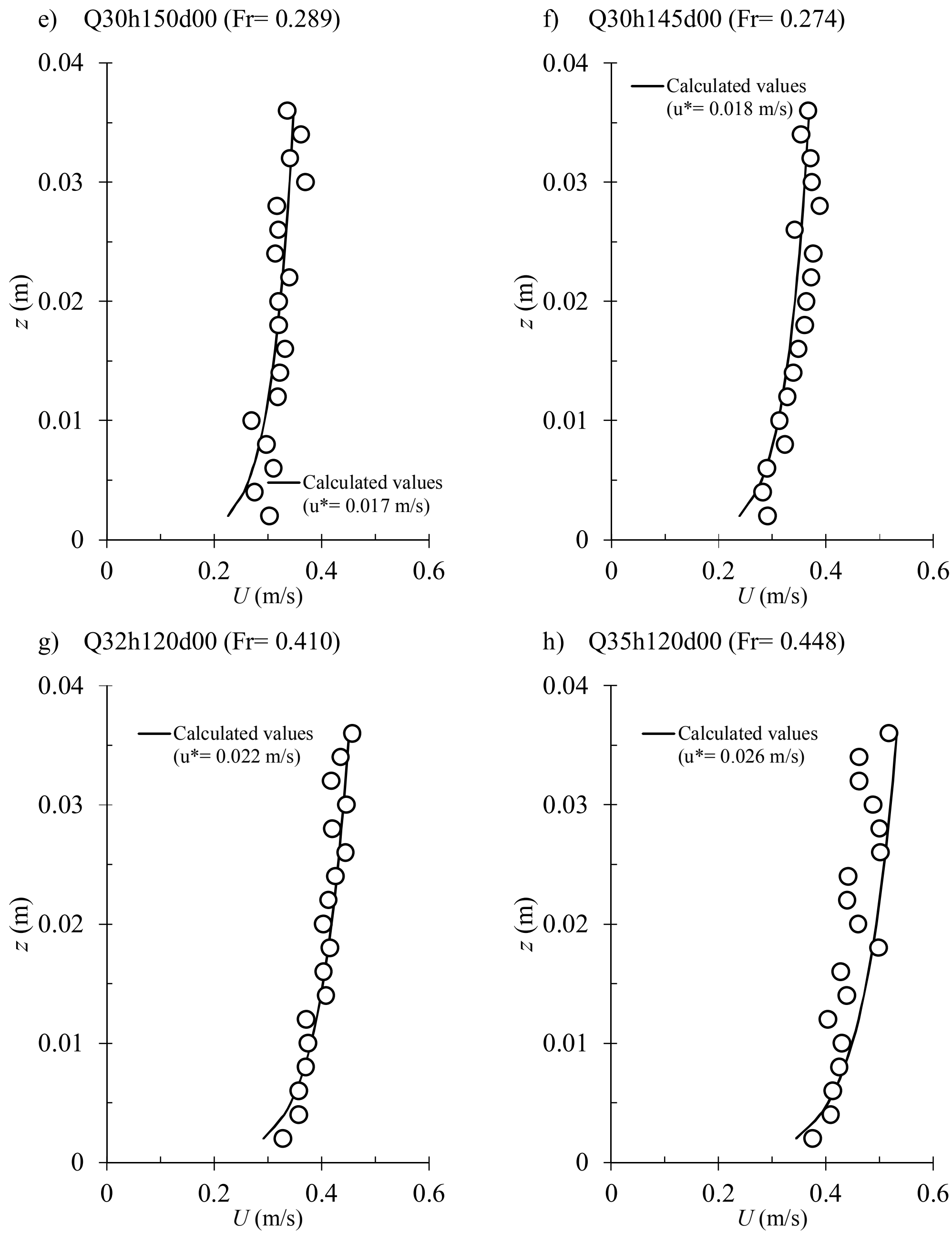

Figure 4.14 Continued

i) Q35h144d00 (Fr= 0.341) j) Q40h120d00 (Fr= 0.512)

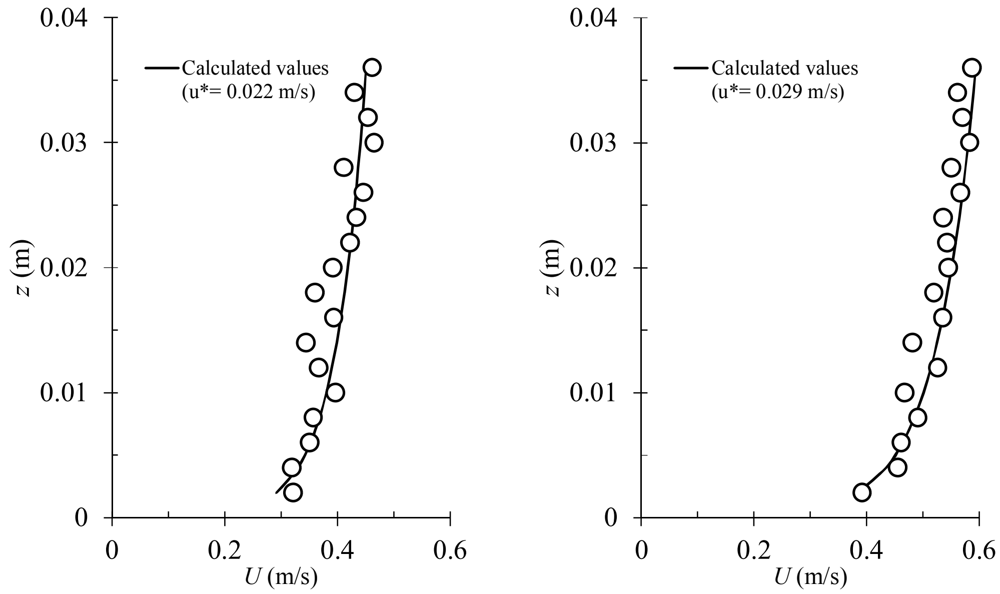

Figure 4.14 Continued

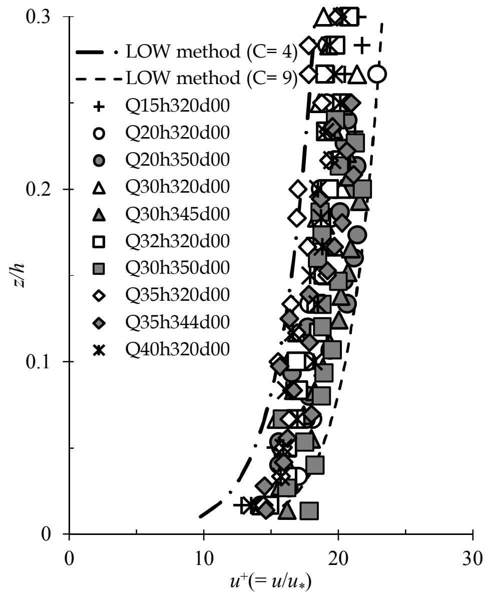

Figure 4.15 Comparisons between Measured and Calculated Values of Normalized Stream-wise Velocity Distribution at Longitudinal Transition

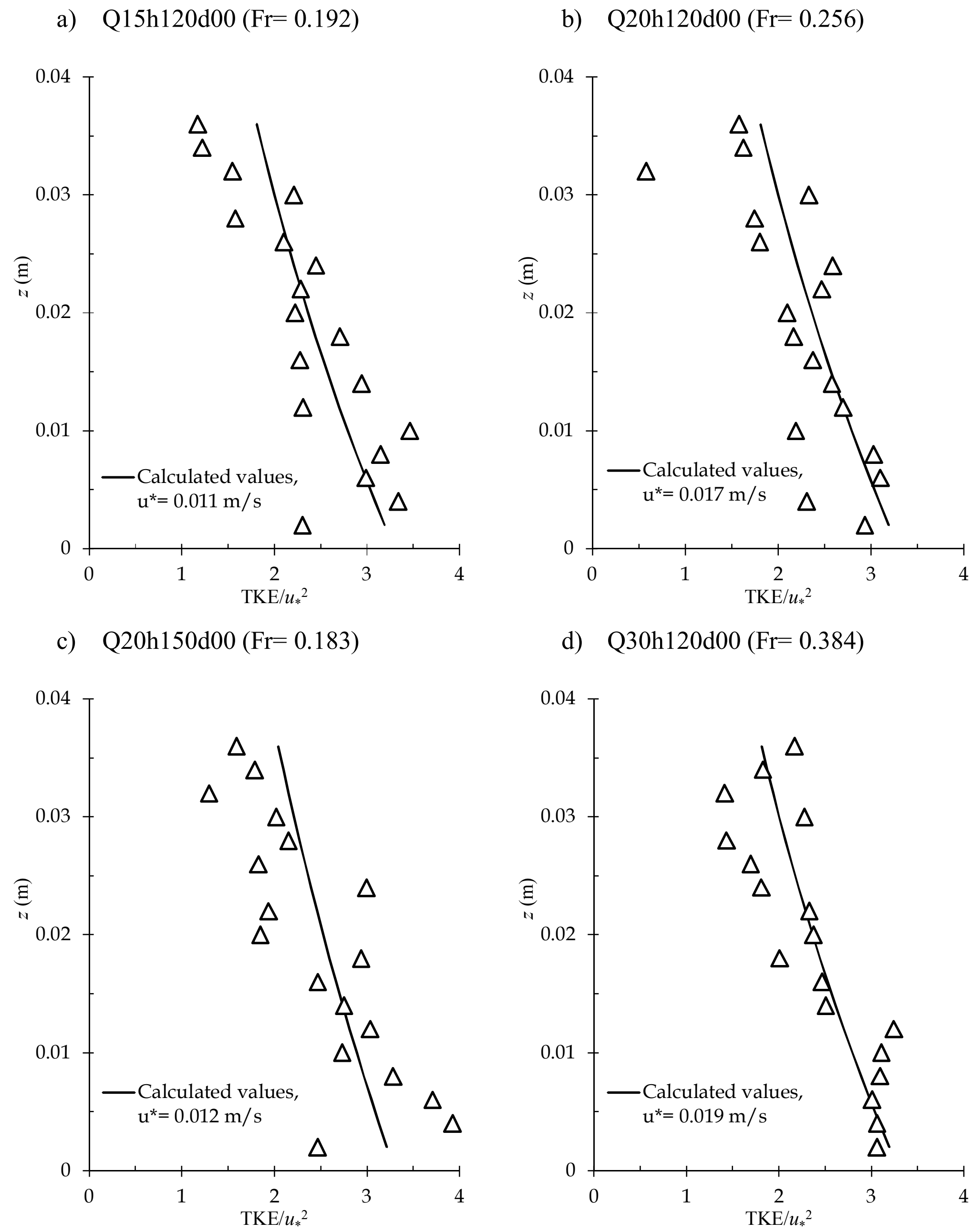

Figure 4.16 Vertical Distribution of Normalized Turbulence Kinetic Energy at Longitudinal Transition

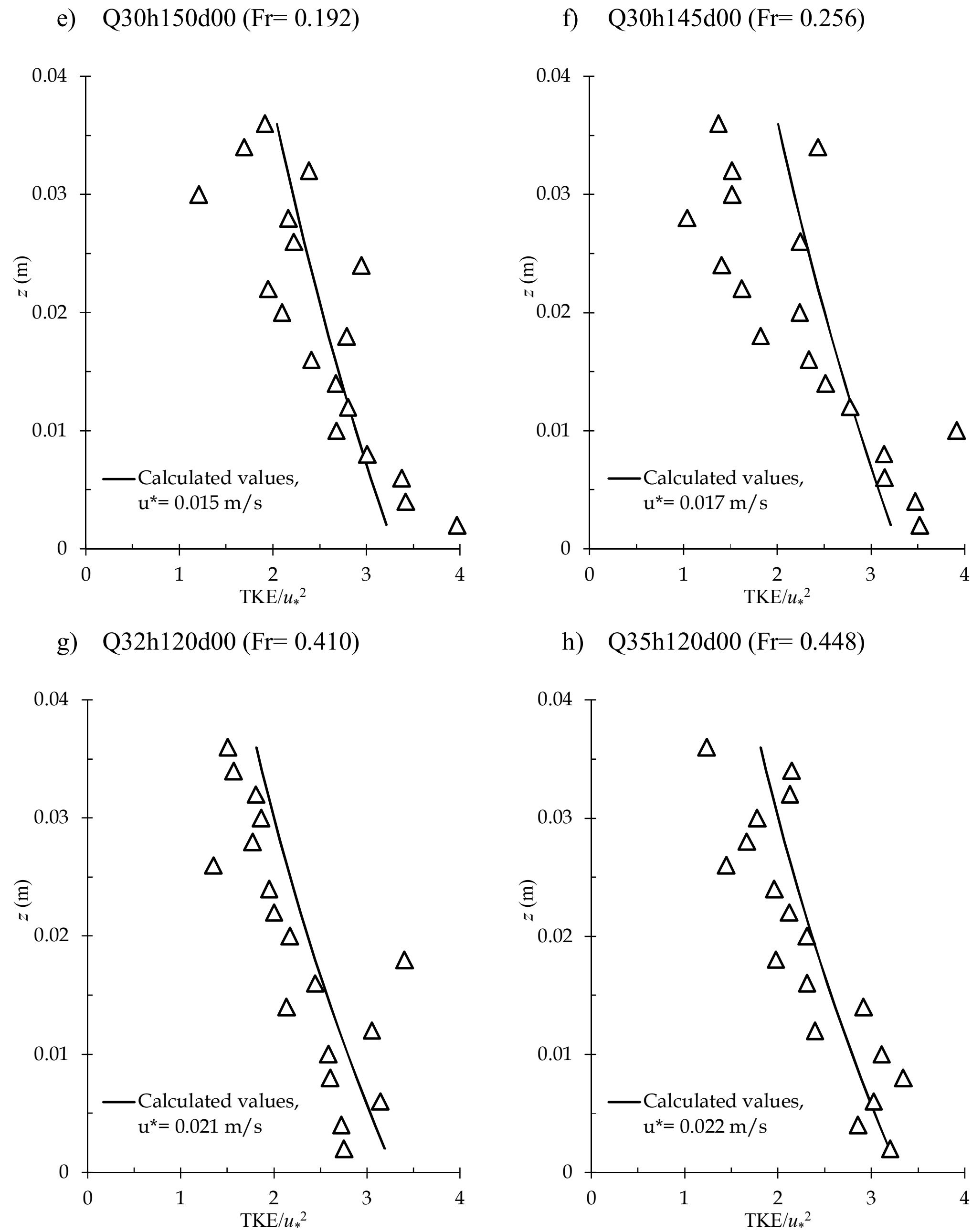

Figure 4.16 Continued

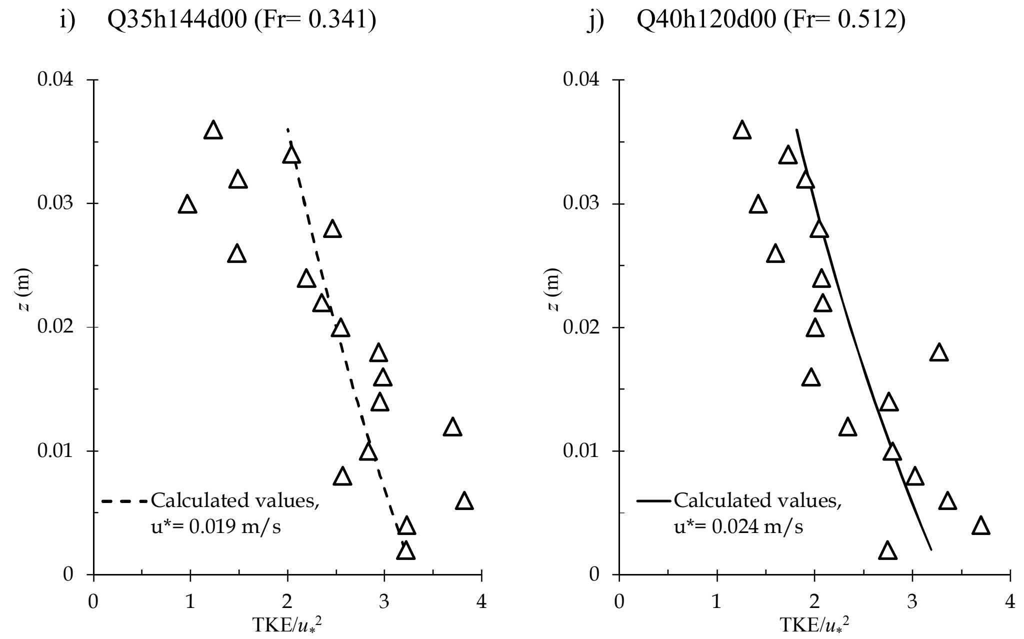

Figure 4.16 Continued

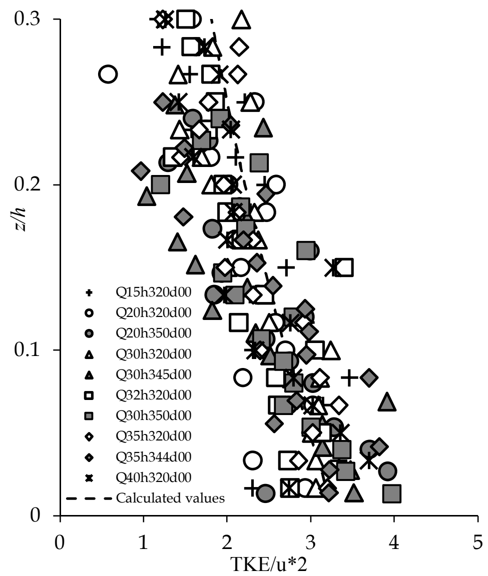

Figure 4.17 Comparisons between Measured and Calculated Values of Normalized Turbulent Kinetic Energy Distribution at Longitudinal Transition

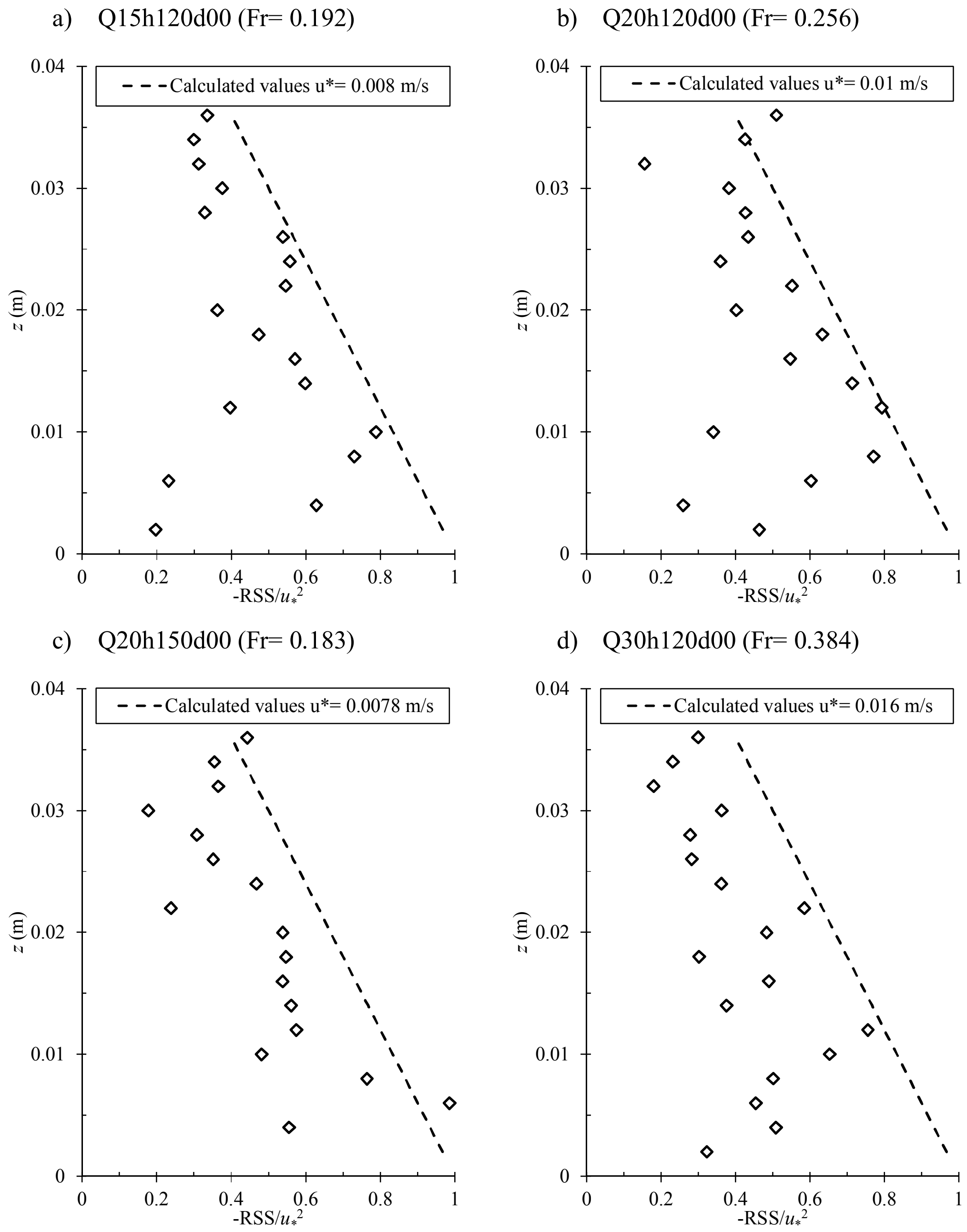

Figure 4.18 Vertical Distribution of Normalized Reynolds Shear Stress at Longitudinal Transition

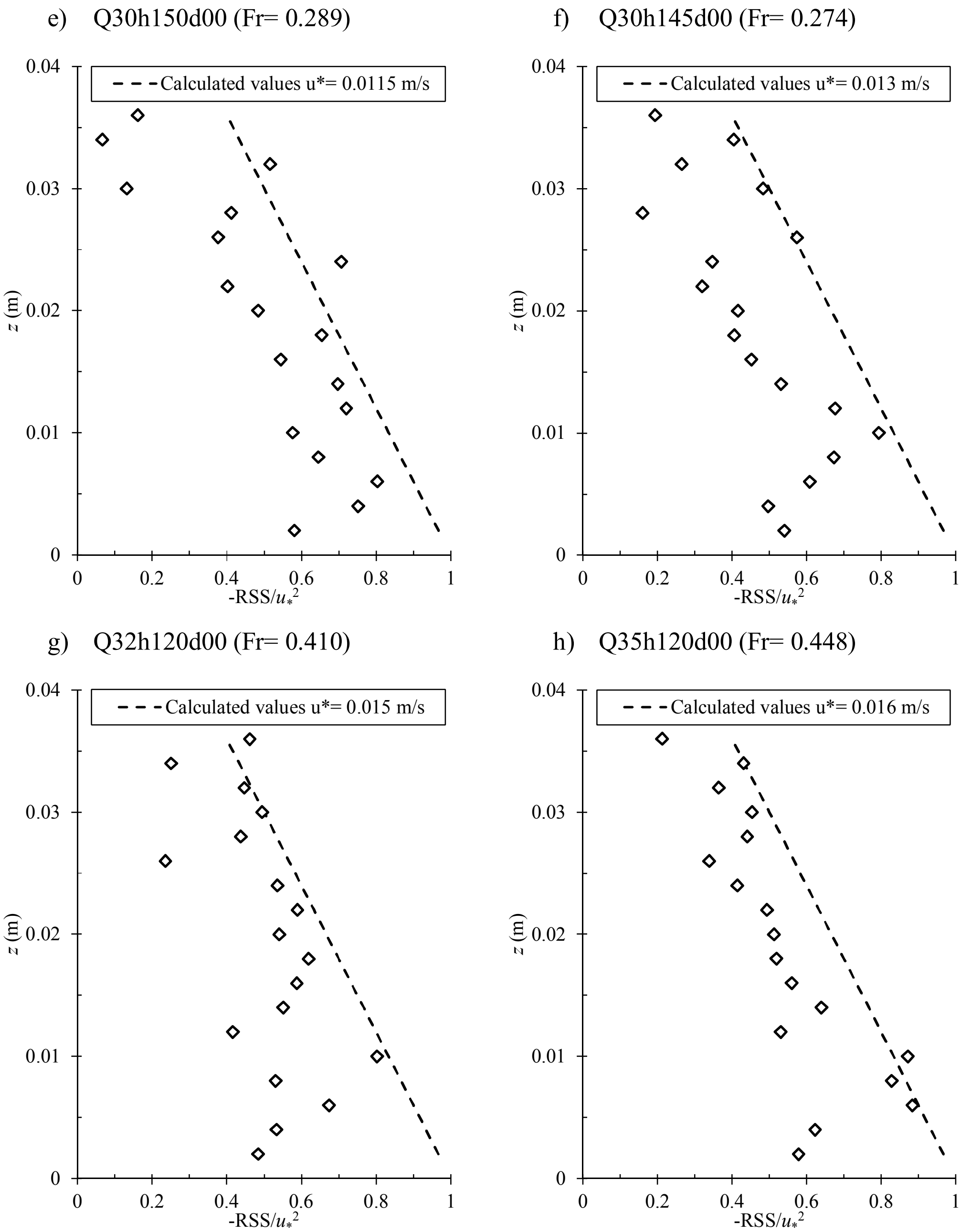

Figure 4.18 Continued

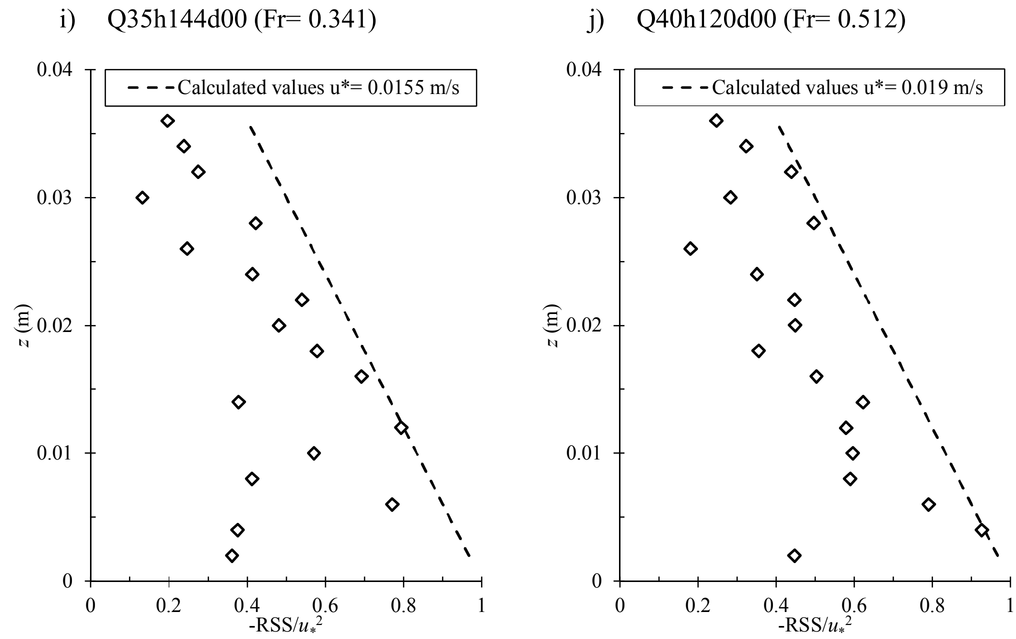

Figure 4.18 Continued

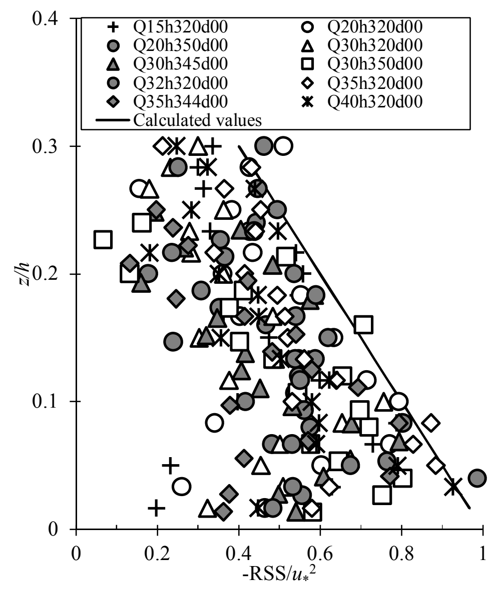

Figure 4.19 Comparisons between Measured and Calculated Values of Normalized Reynolds Shear Stress at Longitudinal Transition

δ_* from the differences between U_{free} and local velocity. Estimated values of bed shear velocity and stress by using three methods at the transition were determined and compared with different hydraulic parameters (mean flow velocity, Froude number, and depth-averaged relative turbulence intensity) in Table 4.5.

Estimated values of bed shear stress with LOW method were compared with those of TKE and RSS methods with using the definitnition ($=\alpha_0 u_*/U_0$) in Figure 4.20. Consequently, values of TKE method were distributed closer to LOW method than those of RSS method from the plots. Also it can be said that the values of RSS method should be modified with approariate coefficient. Calculated and modified values of estimated r_0 of LOW and RSS method, respectively were plotted with coefficient, α_0, which is suggested as 1.2 in Graf (1998) in Figure 4.21. Using TKE method, r_0 were calculated and relationships of Fr and Re_* against r_0 were plotted in Figure 4.22. Functional relationships are as follows:

$$r_0 = \alpha_1 \mathrm{Fr}^{\beta_1} \tag{4.2-a}$$

$$r_0 = \alpha_2 \,\mathrm{Re}_*^{\beta_2} \tag{4.2-b}$$

where, α_1 and α_2 are the calibration coefficients, which are varied from 0.040 to 0.056 and from 0.144 to 0.19, respectively. β_1 and β_2 are the calibration exponents (-0.22). Also a linear relationship between Fr and Re_* from the result of Figure 4.22 and Eq. 4.2 is

$$\mathrm{Fr} = \alpha_3 \,\mathrm{Re}_* \times 10^{-3} \tag{4.3}$$

where α_3 is the calibration coefficient (from 1.44 to 2.16) from the results in Figure 4.23.

Table 4.5 Comparisons of Hydraulic Conditions and Bed Shear Stress with Various Estimation Methods at Longitudinal Transition

case	U_0 (m/s)	Fr (-)	LOW method				TKE method		RSS method
			τ_0 (Pa)	δ_* (mm)	U_{free} (m/s)	Re_* $*10^{-3}$ (-)	τ_0 (Pa)	r_0 (-)	τ_0 (Pa)
Q15h320	0.21	0.δ192	0.121	8.4	0.26	0.092	0.121	0.063	0.081
Q20h320	0.28	0.26	0.23	7.8	0.35	0.116	0.29	0.073	0.121
Q20h350	0.22	0.183	0.144	8.7	0.28	0.104	0.144	0.065	0.081
Q30h320	0.42	0.38	0.44	9.0	0.49	0.189	0.36	0.055	0.22
Q30h345	0.35	0.29	0.29	8.1	0.43	0.138	0.29	0.059	0.144
Q30h350	0.33	0.27	0.32	8.6	0.41	0.155	0.23	0.054	0.112
Q32h320	0.44	0.41	0.48	9.0	0.52	0.197	0.44	0.057	0.20
Q35h320	0.49	0.45	0.68	11.2	0.61	0.290	0.48	0.054	0.24
Q35h344	0.41	0.34	0.48	10.1	0.53	0.223	0.36	0.056	0.21
Q40h320	0.56	0.51	0.84	10.6	0.69	0.308	0.58	0.051	0.35

a) TKE method

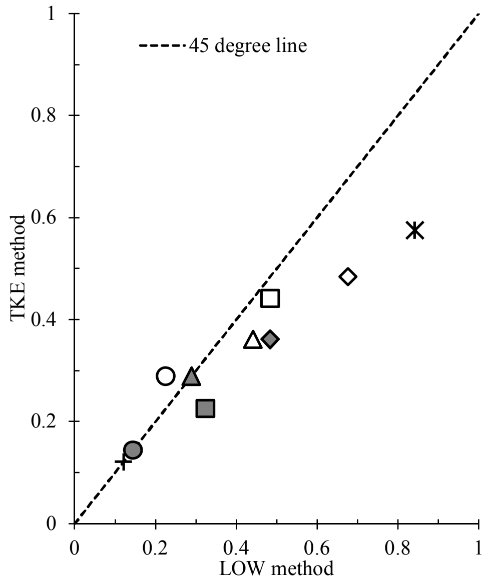

b) RSS method

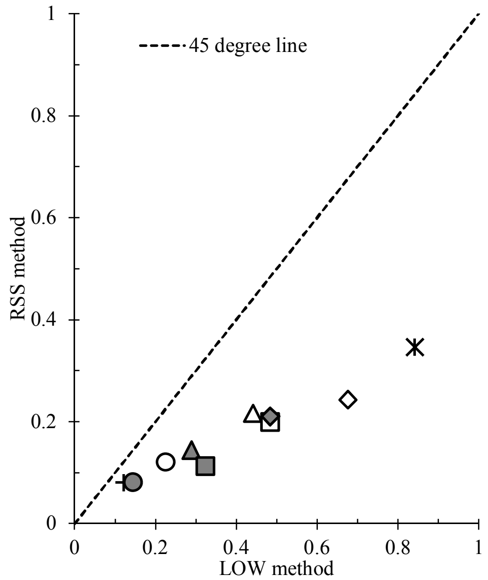

Figure 4.20 Comparisons of Bed Shear Stress

with Various Estimation Methods at Longitudinal Transition

a) LOW method (Calculated by α_0= 1.2)

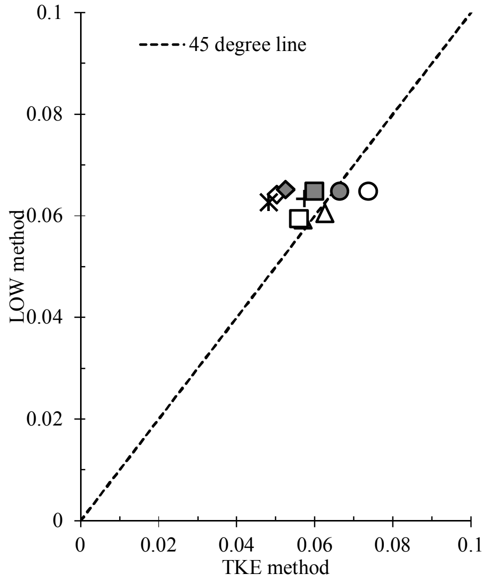

b) RSS method (Calculated by α_0= 1.6)

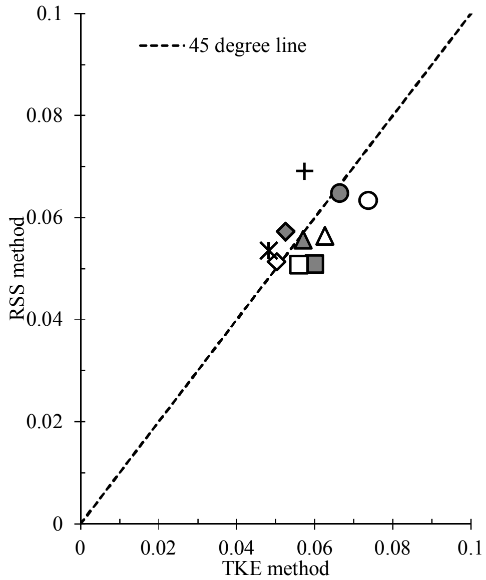

Figure 4.21 Comparisons of Depth-averaged Relative Turbulence Intensity with Various Estimation Methods at Longitudinal Transition

a) Froude number

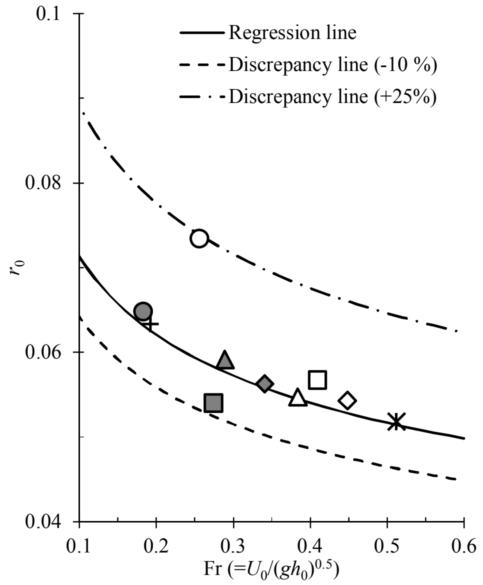

b) Boundary Reynolds Number

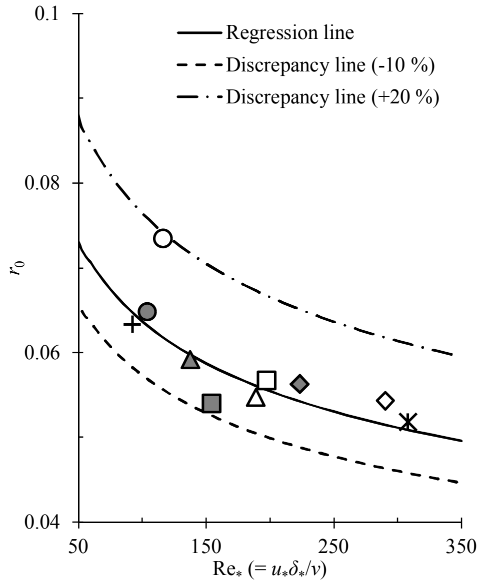

Figure 4.22 Relationship between Hydraulic Parameters and Depth-averaged Relative Turbulence Intensity at Longitudinal Transition

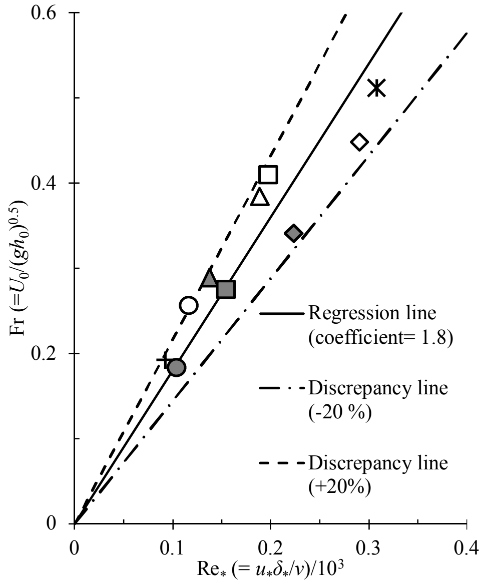

Figure 4.23 Linear Relationship between Boundary Reynolds Number and Froude Number at Longitudinal Transition

4.1.2 Characteristic Length Scale

Previously, several hydraulic parameters were analyzed with various flow conditions at the longitudinal transition. In this chaper, development of turbulent shear layer thickness at the transition toward an abrupt bed elevation decrease were analyzed in backward-facing step flow. Appropriate length scale from this tests will be applied to normalize the temporal development of local scouring in the following chapter.

To analyze the development of turbulent shear layer thickness, vertical 2-D flow measurement were conducted with using PIV system in the backward-facing step flow. Experimental setup was decribed in Figure 4.24. Laser supply system is mounted on the carriage and reflectging mirror changed the direction of laser from the system. A field of view is ~300 * 300 mm in the vicinity of the step (height= 0.2 m). Measuring frequency was 10 Hz for 30 seconds (i. e. 300 data set). Measuring interests of this test were described in Figure 4.25 in detailed. Previously analyzed, flow separation and excessive increase of gradients of stream-wise velocity were estimated close to the step. Based on the data of dU/dz and recirculation profiles of vector flow field, developed length scale of turbulent shear layer thickness, $\delta_{*,m}$ and the longitudinal distance from the transition to the location of $\delta_{*,\mathrm{m}}$ were determined from the contour plot in Figure 4.26. And the slope of the turbulent shear layer from the transition, θ_δ was calculated with the ratio of $\delta_{*,\mathrm{m}}$ and $L_{*,m}$. and compared with upstream scour slope, θ_{up} in the next chapter. Also properties of turbulent shear layer thickness in the backward-facing step flow were estimated in Table 4.6 and fuctional relationships of them were analyzed.

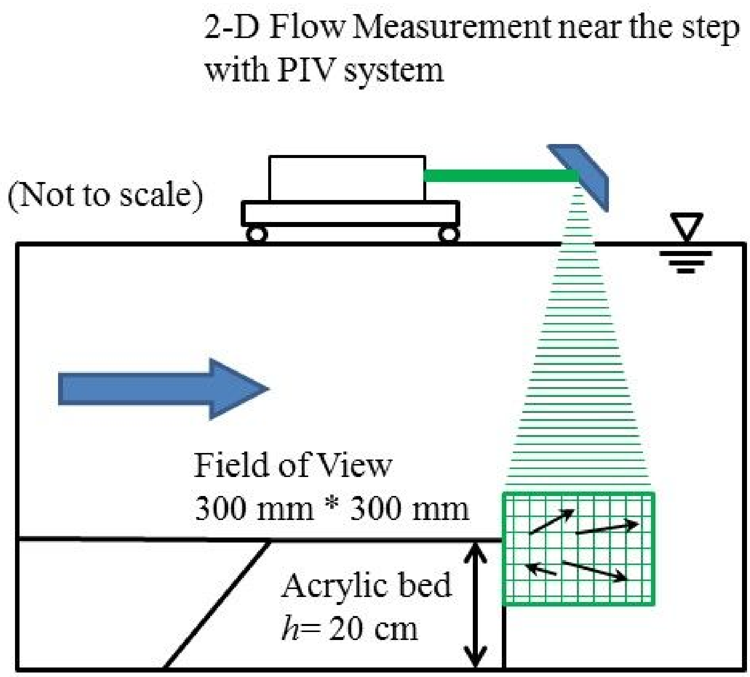

Figure 4.24 Schematic Diagram of 2-D Flow Measurement in Backward-facing Step Flow

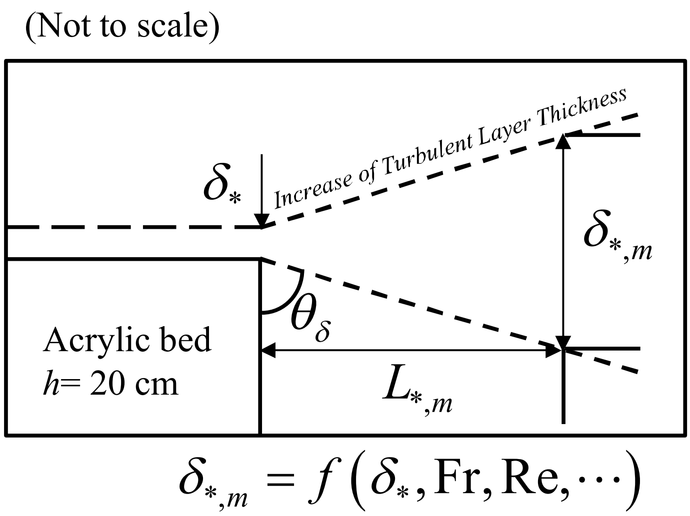

Figure 4.25 Development of Turbulent Layer Thickness in Backward-facing Step Flow

a) Q15h150 (Fr= 0.137)

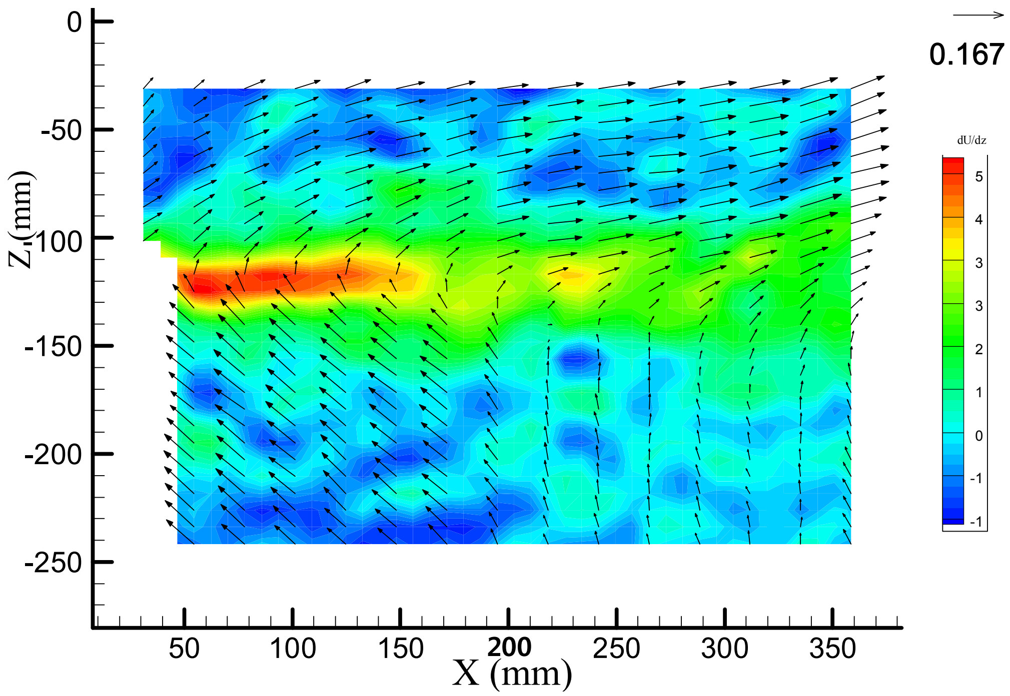

b) Q30h240 (Fr= 0.136)

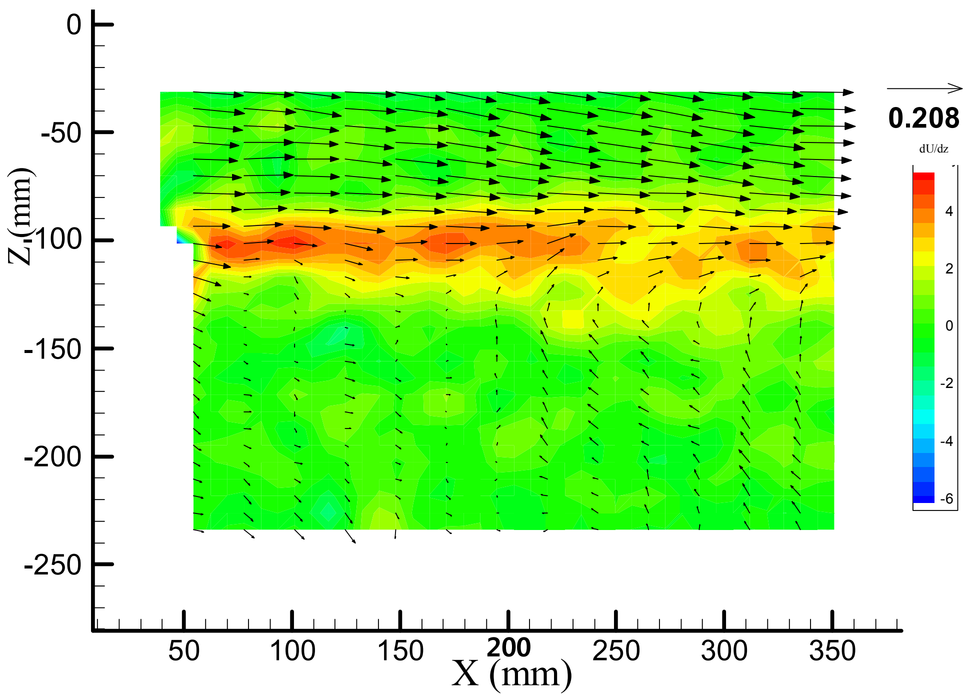

Figure 4.26 Distributions of Vector Fields and Shear Stress in Backward-facing Step Flow

c) Q20h150 (Fr= 0.183)

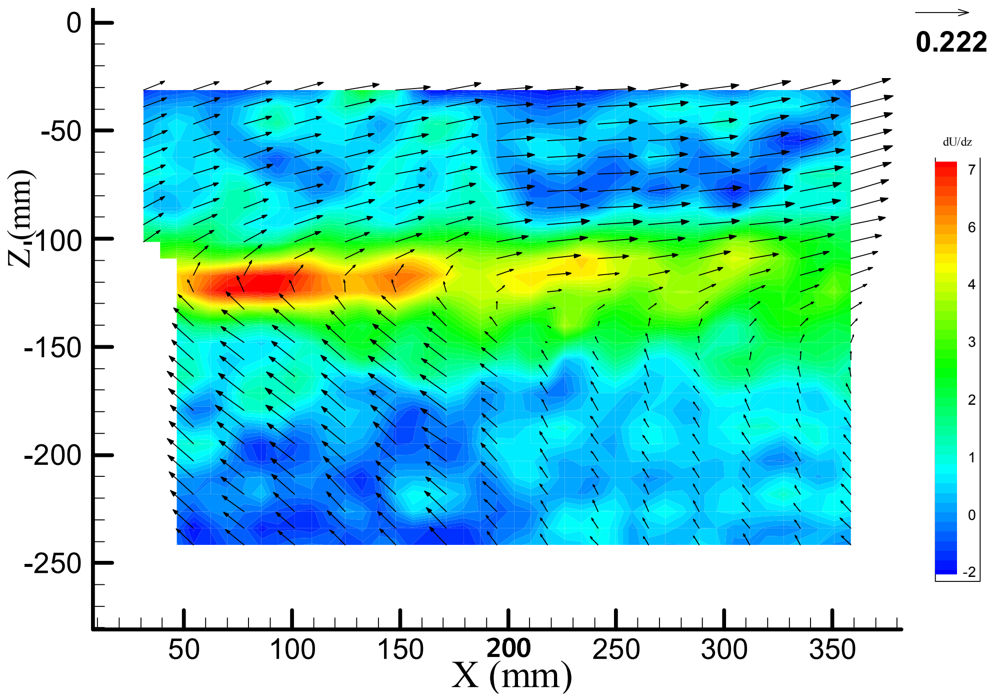

d) Q35h210 (Fr= 0.194)

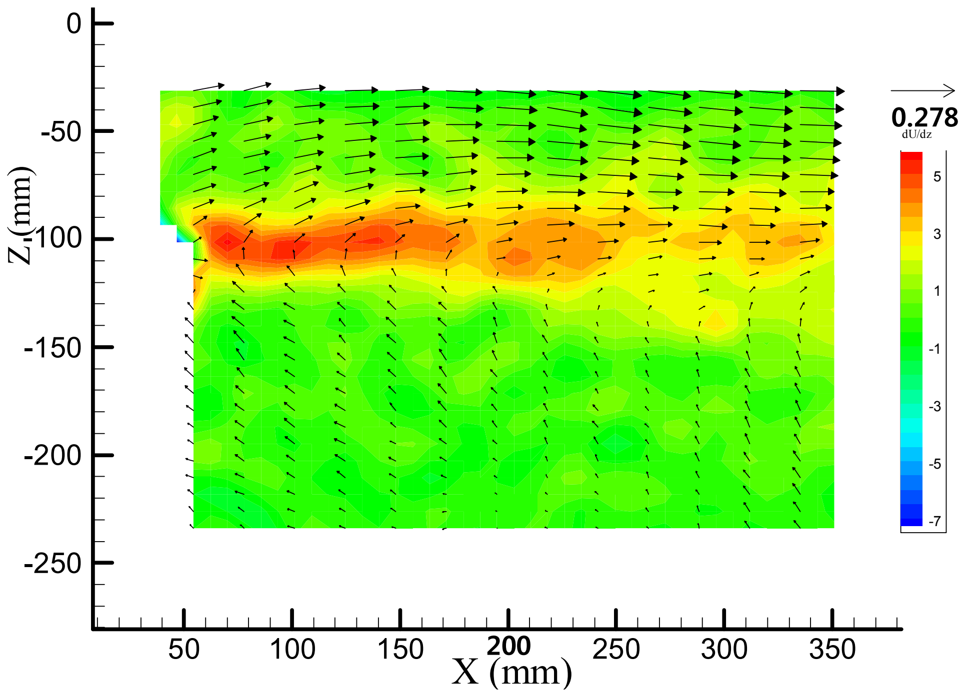

Figure 4.26 Continued

e) Q35h144 (Fr= 0.34)

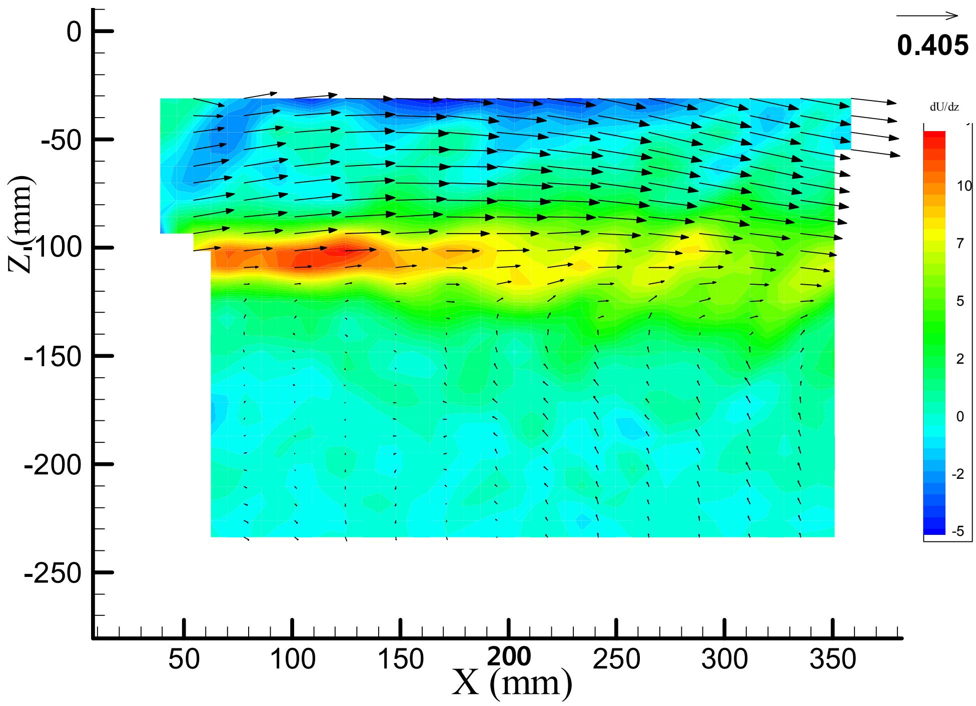

Figure 4.26 Continued

Table 4.6 Flow Parameters and Results of Backward-facing Step Test

case	U_0 (m/s)	Fr (-)	Re_* (-)	δ_* (mm)	$\delta_{*,m}$ (mm)	$(\delta_{*,m}-\delta_*)/\delta_*$ (-)	$L_{*,m}$ (mm)	cot θ_δ ($=2L_{*,m}/\delta_{*,m}$, -)
Q15h150	0.167	0.137	90	7.0	100	13.2	100	0.25
Q30h240	0.21	0.136	89	7.0	80	10.4	200	0.20
Q20h150	0.22	0.183	120	7.9	70	7.9	180	0.194
Q35h210	0.28	0.194	128	8.1	50	5.2	160	0.156
Q35h144	0.41	0.34	10	9.5	40	3.2	200	0.133

With data of two dimensional vorticity can be calculated as follows:

$$d\Gamma = \left(\frac{\partial \overline{w}}{\partial x} - \frac{\partial \overline{u}}{\partial z} \right) dxdz \tag{4.4}$$

Here, Γ denotes the value of vorticity in the x-z plane. Eq. 4.4 can be rearranged as follows:

$$\frac{d\Gamma}{dxdz} = \xi_{xz} = \frac{\partial \overline{w}}{\partial x} - \frac{\partial \overline{u}}{\partial z} \tag{4.5}$$

Here, ξ_{xz} denotes vorticity per unit area.

Distribution of ξ_{xz} were depicted in Figure 4.27 with the distribution of streamline. From the figures, two dimensional distribution of the per unit area were corresponded the distribution of the velocity gradients. And the maximum value of the vocity was occured at x~ 0.4 m from the step. Also backward flow distribution were occured until x= 1.0 m and then all of the streamline were headed toward downstream of the step.

Ratios of turbulent layer thickness at the longitudinal transition and in the turbulent shear layer is as follows:

$$\frac{\Delta\delta_*}{\delta_*} = \frac{\left(\delta_{*,m} - \delta_*\right)}{\delta_*} \alpha_4 \left(\mathrm{Fr} \cdot \mathrm{Re}_*\right)^{\beta_4} \tag{4.6}$$

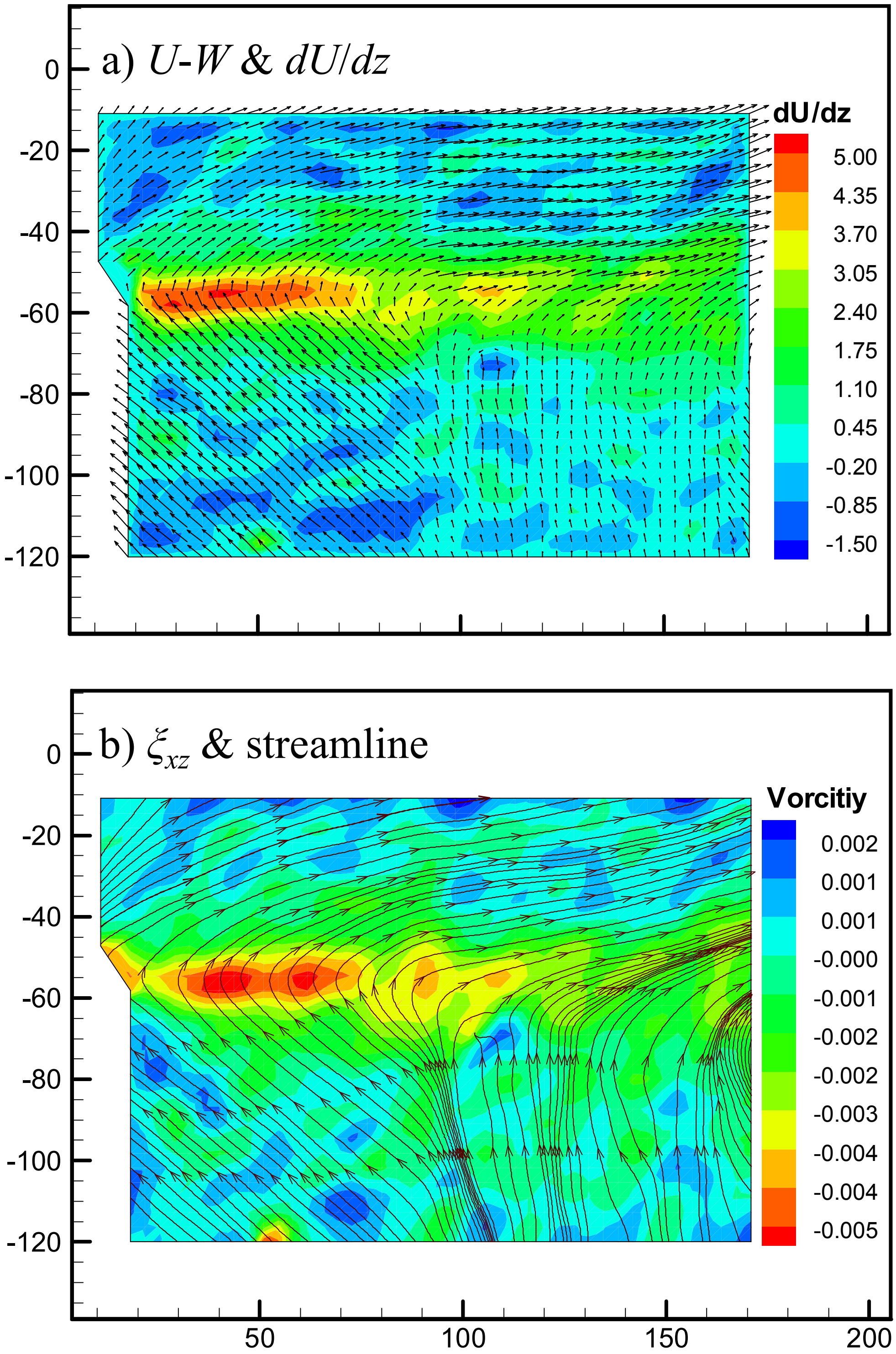

Figure 4.27 Distribution of Velocity Gradient and Vorticity (case Q15h150; Fr= 0.137)

where α_4 and β_4 are the calibration coefficient (= 40) and exponent (= -0.6), which were estimated in Figure 4.27-a). With Eq. 4.4, $\delta_{*,\mathrm{m}}$ can be rewritten as follows:

$$\delta_{*,m} = \delta_* \left[\alpha_4 \left(\mathrm{Fr} \cdot \mathrm{Re}_* \right)^{\beta_4} + 1 \right] \tag{4.6}$$

$\delta_{*,\mathrm{m}}$ represents the capacity of the local scouring due to the flow fluctuation and excessive values of stream-wise velocity gradients in the turbulent shear layer. Therefore characteristic length scale on the local scouring, λ in this study was determined as follows:

$$\lambda = \delta_{*,m} = f\left(\delta_*, \mathrm{Fr}, \mathrm{Re}_* \right) \tag{4.6}$$

λ was also applied to normalize the length scale of scour depth and to determine the time scale of scouring in the following chapter as well.

Additionally, a longitudinal distance from the transition to the location of the maximum values of δ_* was denoted as $L_{*,m}$ in Figure 4.25. A functional relationship of the slope of the turbulent shear layer and flow parameters were regressed as follows:

$$\frac{\delta_*}{2L_{*,m}} = \cot\theta_\delta = \alpha_5 \left(\mathrm{Fr} \cdot \mathrm{Re}_* \right)^{\beta_5} \tag{4.7}$$

where α_5 and β_5 are the calibration coefficient (= 0.5) and exponent (= -3.2), which were estimated in Figure 4.28-b). This slope of the layer were compared with the development of upstream scour slope in the scour test.

a) Thickness

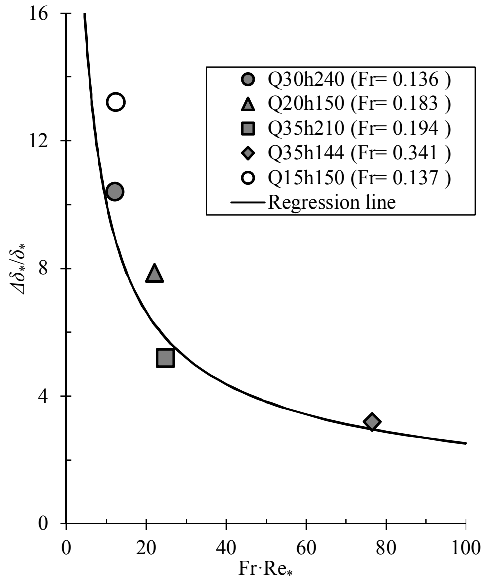

b) Slope

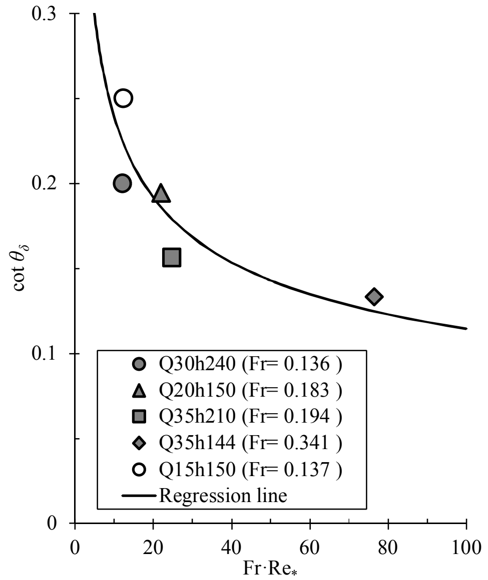

Figure 4.28 Functional Relationships of Turbulent Shear Layer Thickness and Slope in Backward-facing Step Flow

4.2 Temporal Development of Local Scour Hole

4.2.1 Scour Test

To conduct a scour test, Approaching wedge model was positioned at 3 m behind the headtank of the flume and 4 m-long and 0.2 m-high acrylic box model also was attached behind the wedge. And 8.5 m-long region, which is situated 2.5 m at the upstream of the tailgate of the flume was filled with the sand. Measurent of bed and 3-D velocity profiles in the scoured hole was performed with Vectrino on the autotraverse system (Figure 4.29).

At the beginning of the scour test, appropriate setup of sand in the region of the test is the most important procedure. Firstly, dry sand in the test region was packed and flattened with initial bed elevation (η_0= 0.2 m). And then the desirable value of water depth was reached with tab water only to keep the initial bed elevation. Secondly, elevation of movable bed was flattened again to reduce the soil pore with light compaction. Then the desirable water discharge was reached gradually (Figure 4.30). Lastly, scour test was started.

4.2.2 Temporal Development of Local Scour Hole

At each time steps, which were dependent to the scouring, distances from the transmitter of the Vectrino to the eroded bed were measured at each longitudinal measuring grid, which were also dependent to the scouring. Then those values were converted to the bed elevation η (x, t). Temporal developments of the η (x, t) of each 10 cases were plotted in Figure 4.31. To distinguish the change of the bed elevations, only 6 data set of the each cases were drawn and compared.

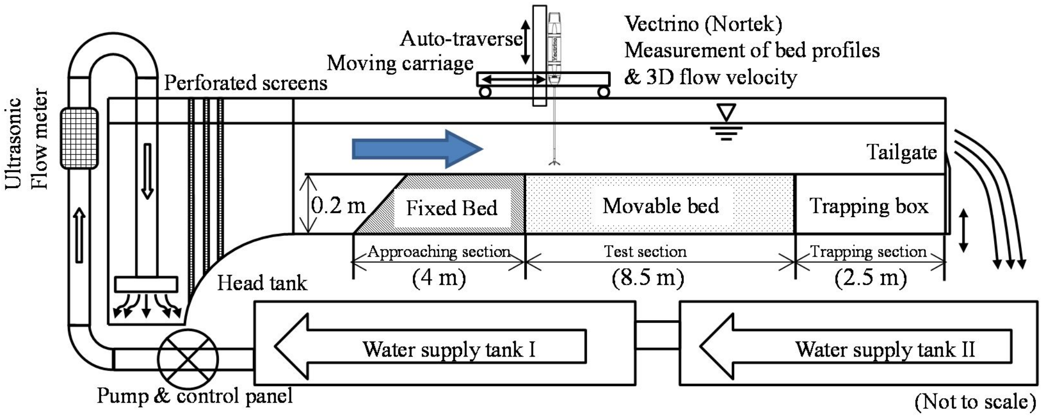

Figure 4.29 Schematic Diagram of Experimental Setup and Apparatus of Scour Test

a) Compacting

b) Flattening

c) Wetting

d) Testing

Figure 4.30 Procedure of Scour Test

a) **Q20h120d12**

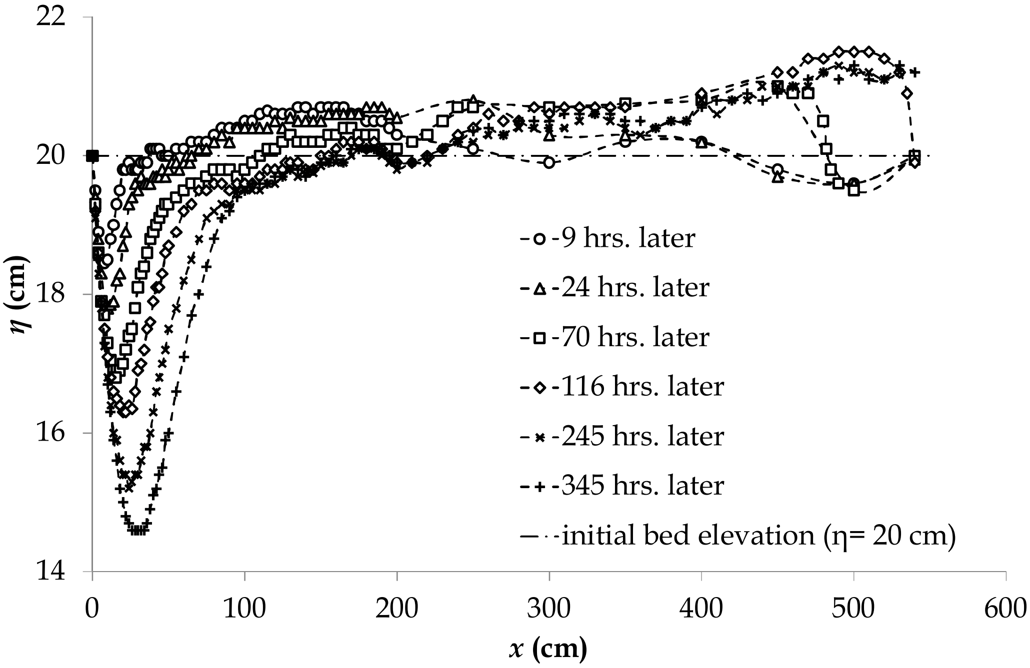

b) **Q30h150d12**

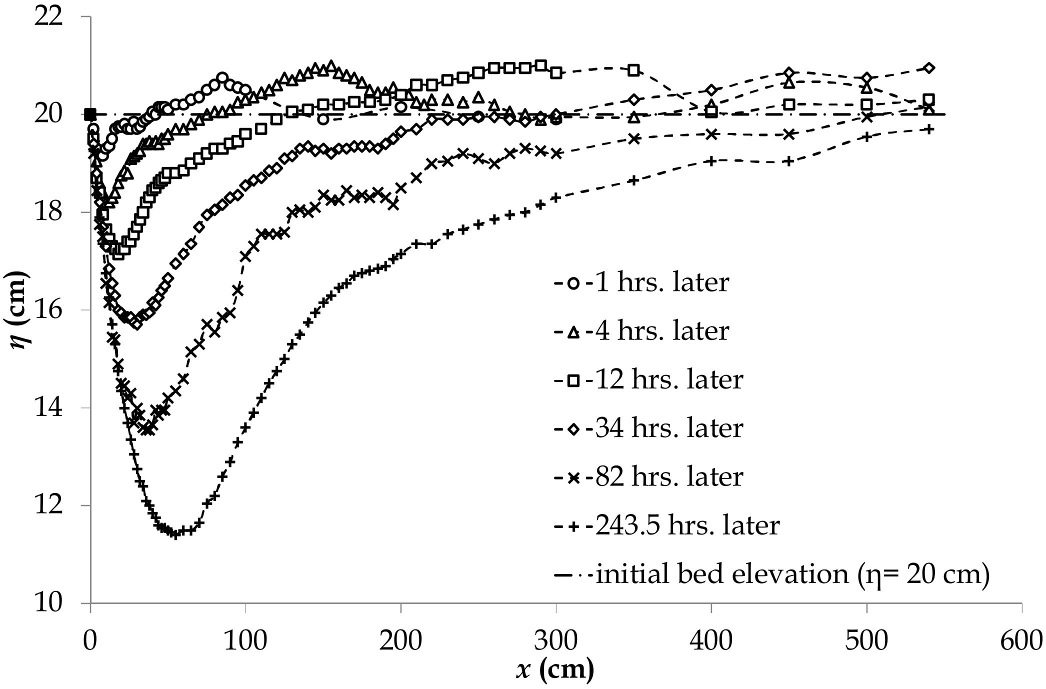

Figure 4.31 Temporal Development of bed Profiles

c) Q30h120d12

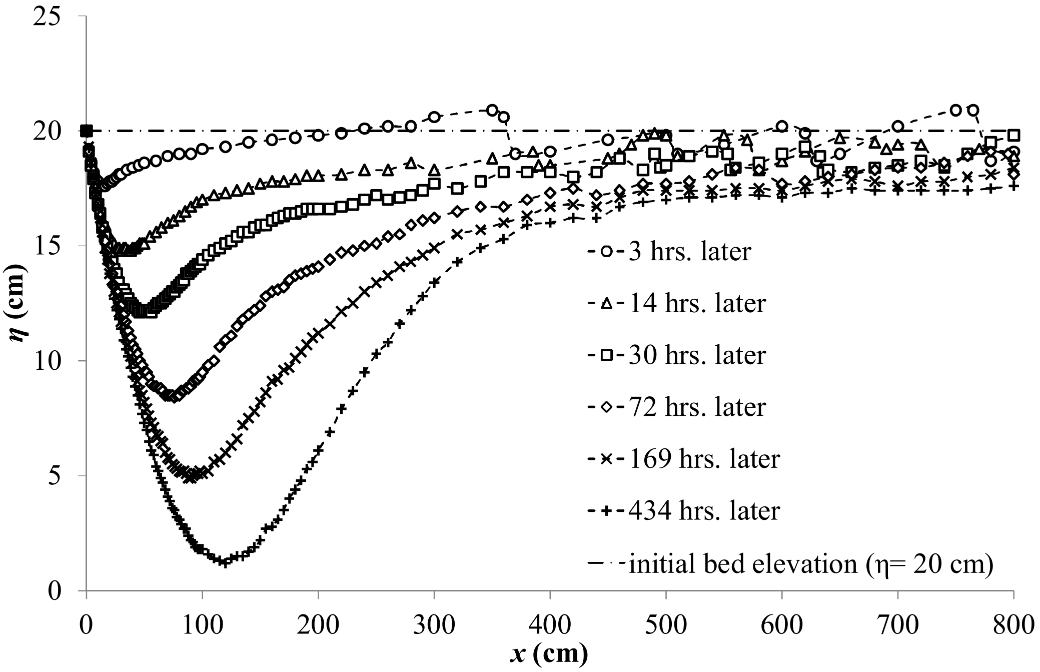

d) Q30h145d12

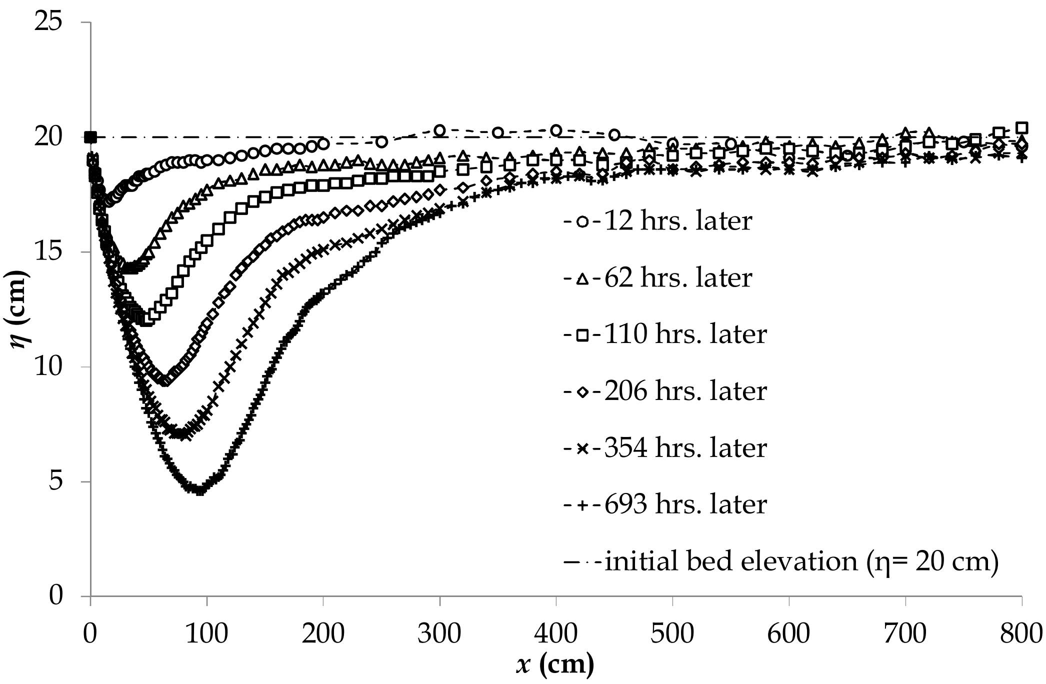

Figure 4.31 continued

e) Q35h120d12

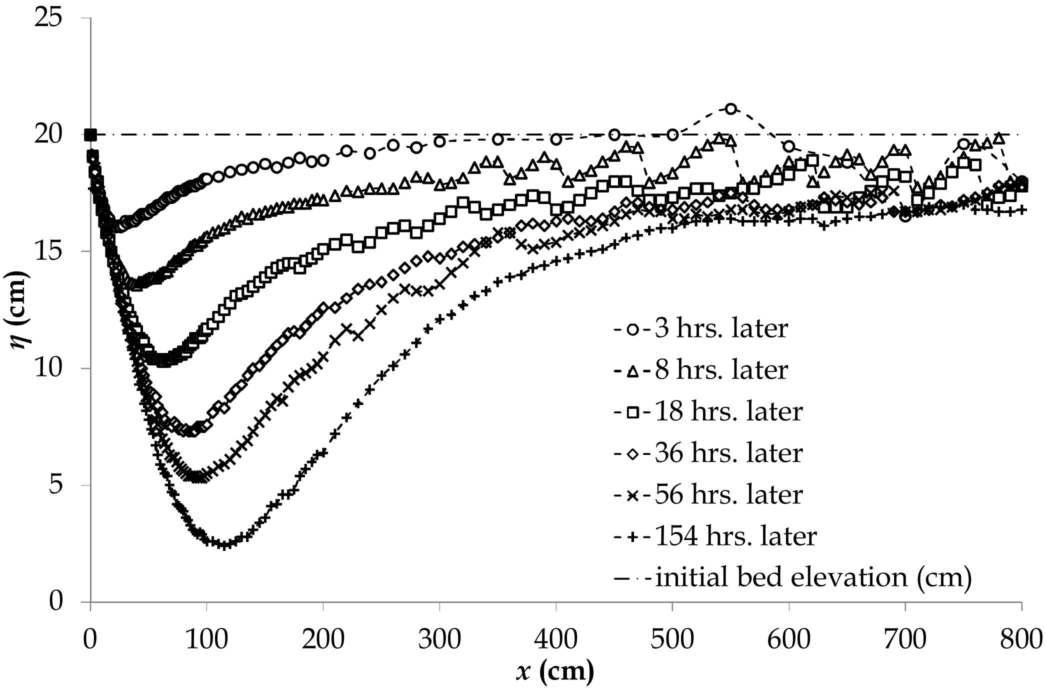

f) Q35h144d12

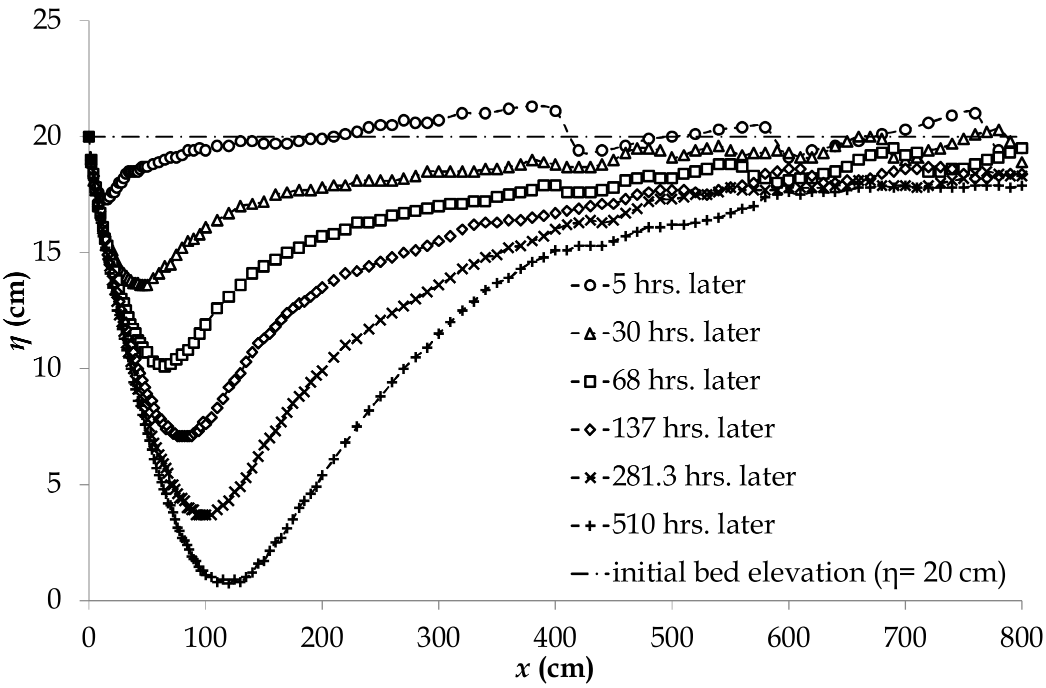

Figure 4.31 continued

g) Q20h120d06

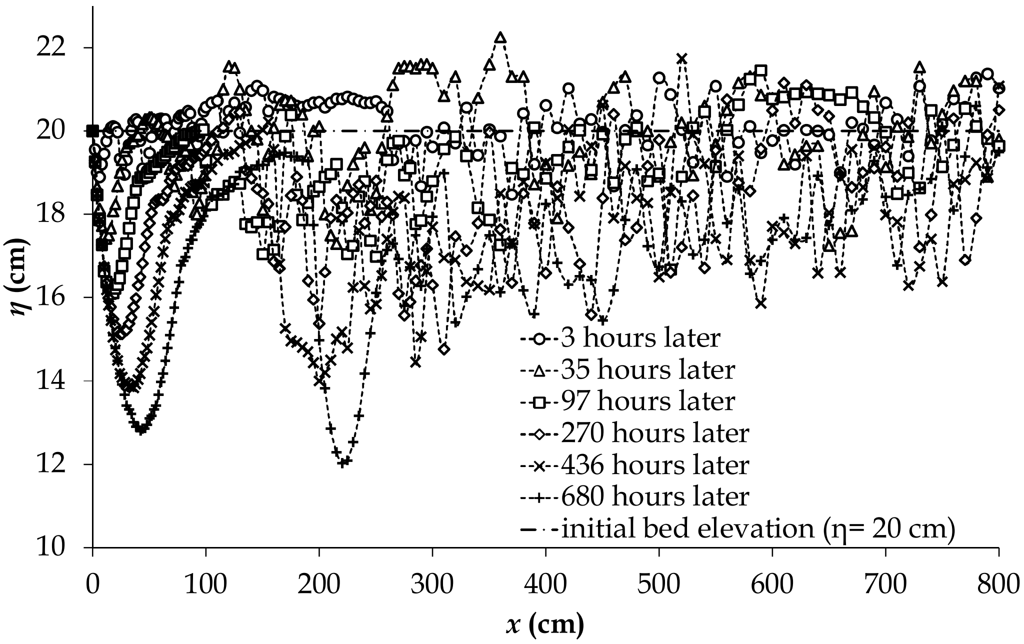

h) Q35h120d06

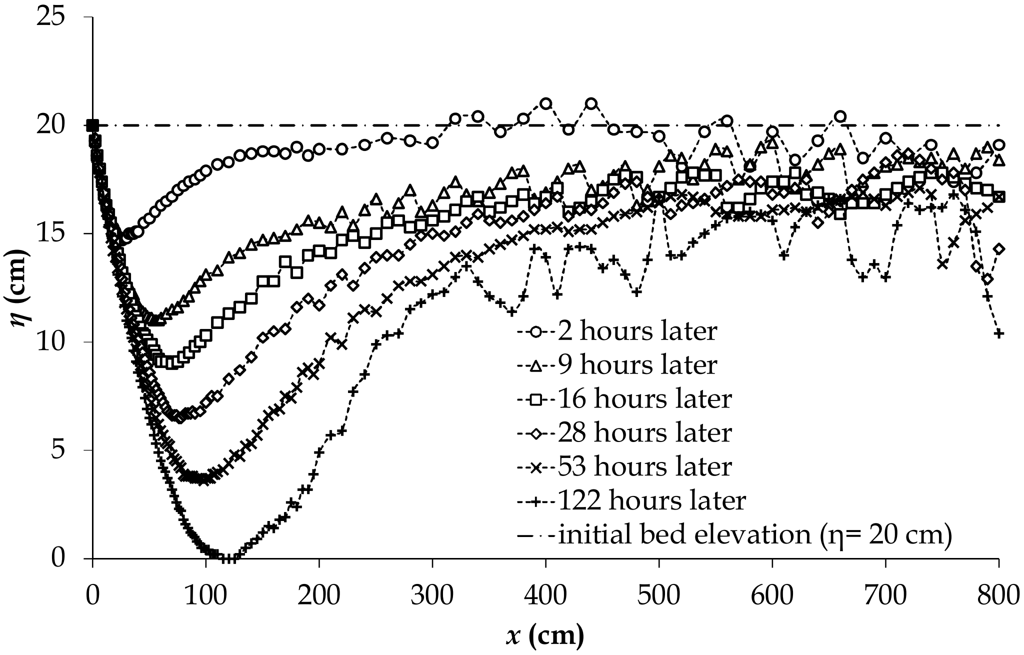

Figure 4.31 continued

i) Q35h150d06

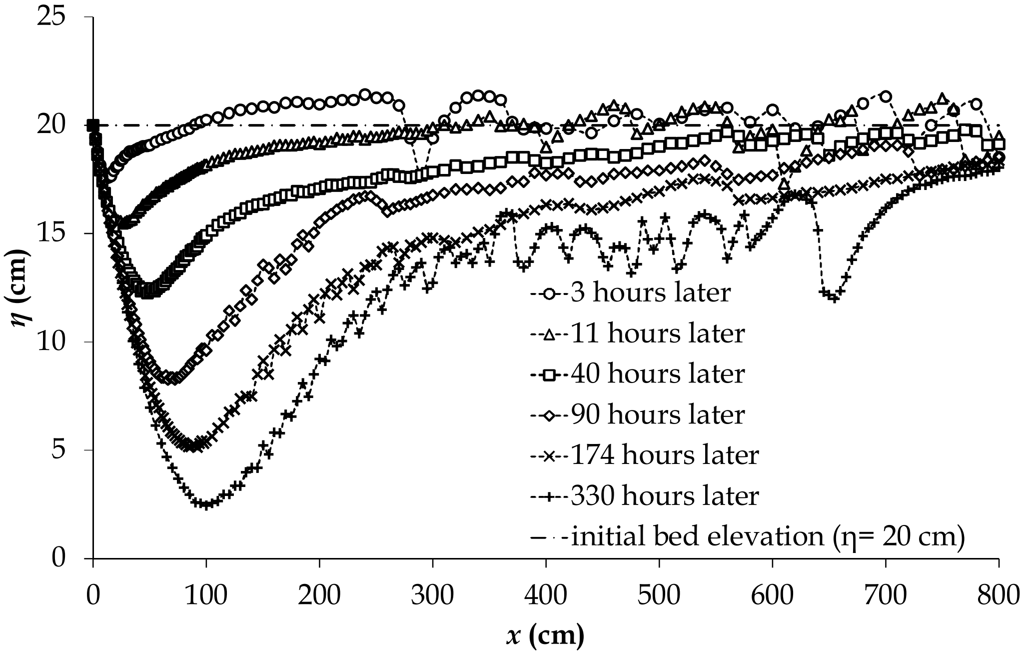

j) Q32h120d06

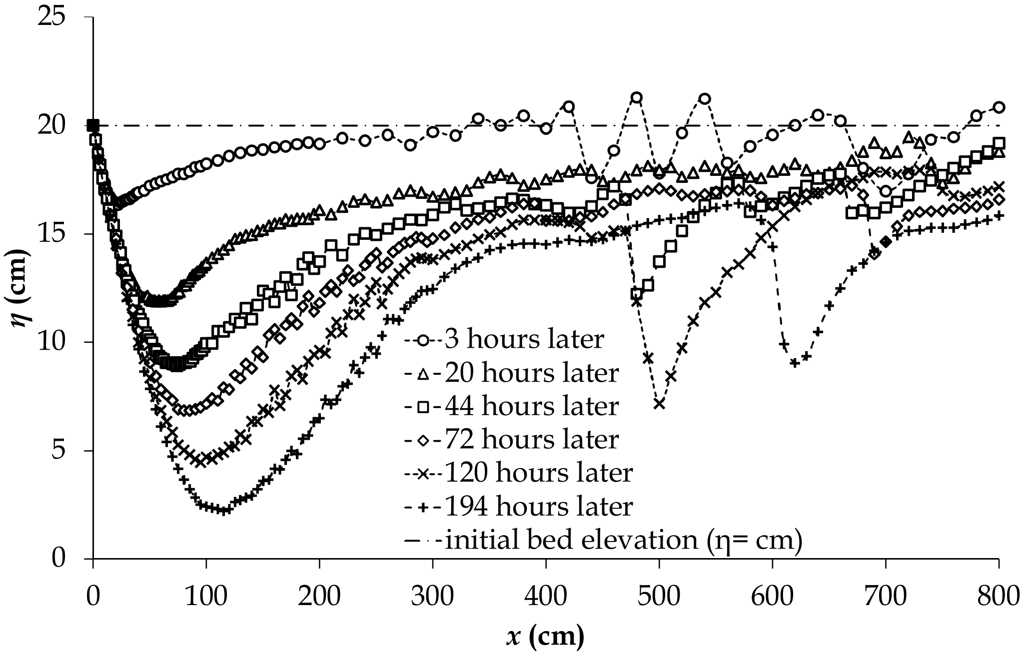

Figure 4.31 Continued

4.2.3 Normalized Maximum Scour Depth

From temporal changes of the bed profiles, properties of the local scouring were estimated as decribed in Chapter 2. And the most important property is the temporal development of the maximum scour depth, $y_m\ (t)$. Temporal change of the values of $y_m\ (t)$ were drawn and compared in Figure 4.32. To compare them accurately, a modified equation of temporal change of y_m was decribed as follows:

$$\frac{y_m}{\lambda} = \left(\frac{t}{t_\lambda}\right)^\gamma \tag{4.8}$$

where λ and t_λ were defined as characteristic length and time scales and described as follows:

$$\lambda = \delta_{*,m} \tag{4.9-a}$$

$$t_\lambda = \left(\alpha_* U_0 - U_c\right) / \delta_{*,m} \tag{4.9-b}$$

With using the Eq. 2.6, Eq. 4.9-b can be rewritten as

$$t_\lambda = \frac{y_{m,e}}{h_0 \lambda} U_c \tag{4.10}$$

Additionally, differentiation of Eq. 4.8 was as follows:

$$\frac{d\left(y_m/\lambda\right)}{dt}=\gamma\frac{t^{\gamma-1}}{t_\lambda^{\ \gamma}} \tag{4.11}$$

We found

$$\frac{d\left(y_m/\lambda\right)}{dt}=\frac{\gamma}{t}\left(\frac{t}{t_\lambda}\right)^\gamma=\frac{\gamma}{t}\left(\frac{y_m}{\lambda}\right) \tag{4.12}$$

And re-arranging Eq. 4.12

$$\frac{d\left(y_m/\lambda\right)}{y_m/\lambda}=\gamma\frac{dt}{t} \tag{4.13}$$

From the upper Eq. 4.13, a meaningful-physical factor on temporal change of y_m, γ was decribed as follows:

$$\begin{aligned}\gamma&=\frac{d\left(y_m/\lambda\right)/\left(y_m/\lambda\right)}{dt/t}\\&=\left(\frac{\text{Fractional change in scour depth}}{\text{Fractional change in time}}\right)\end{aligned} \tag{4.14}$$

Hydraulic-sedimentological parameters and dominant factors on local scouring to predict the equililbrium scour deph were estimated in Table 4.7 and 4.8, respectively.

a) Q20h120d12

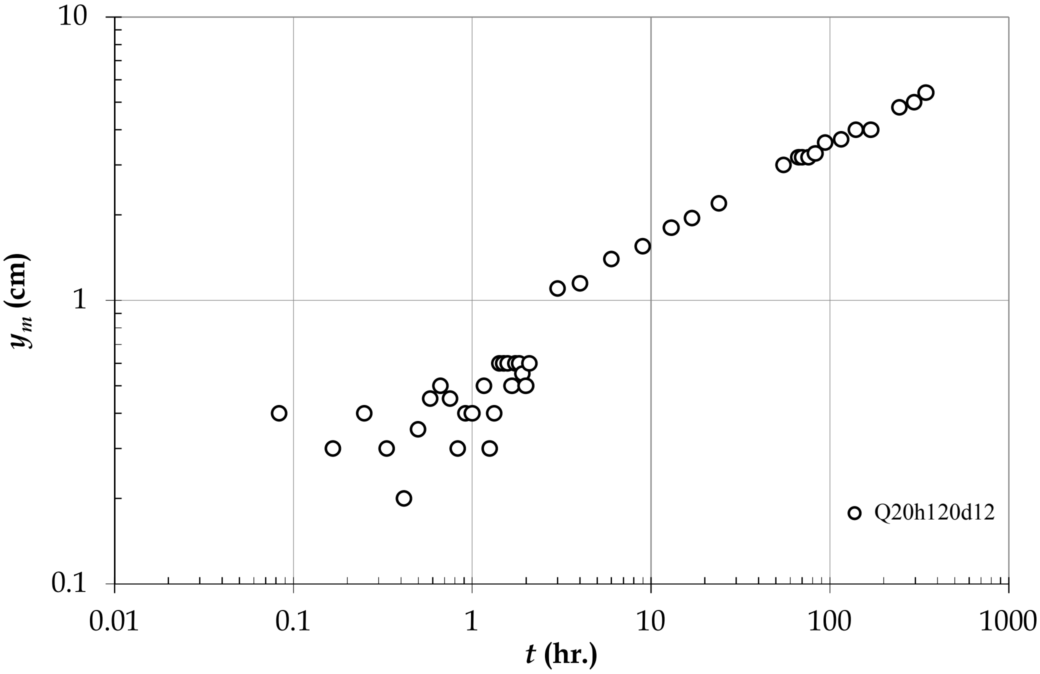

b) Q30h150d12

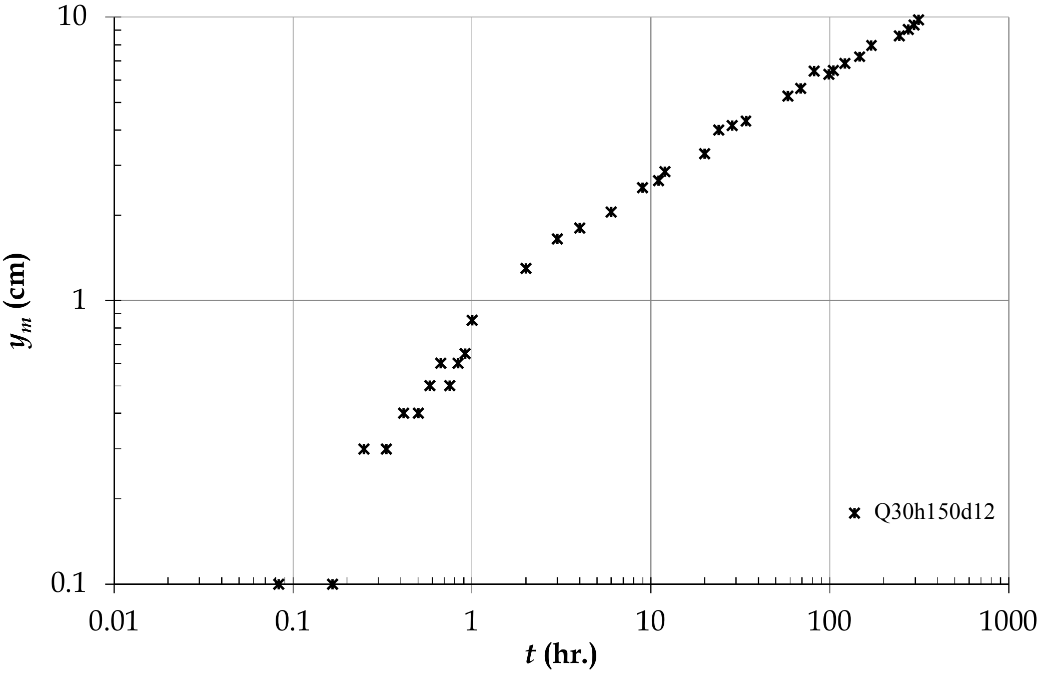

Figure 4.32 Temporal Development of Maximum Scour Depth

c) Q30h120d12

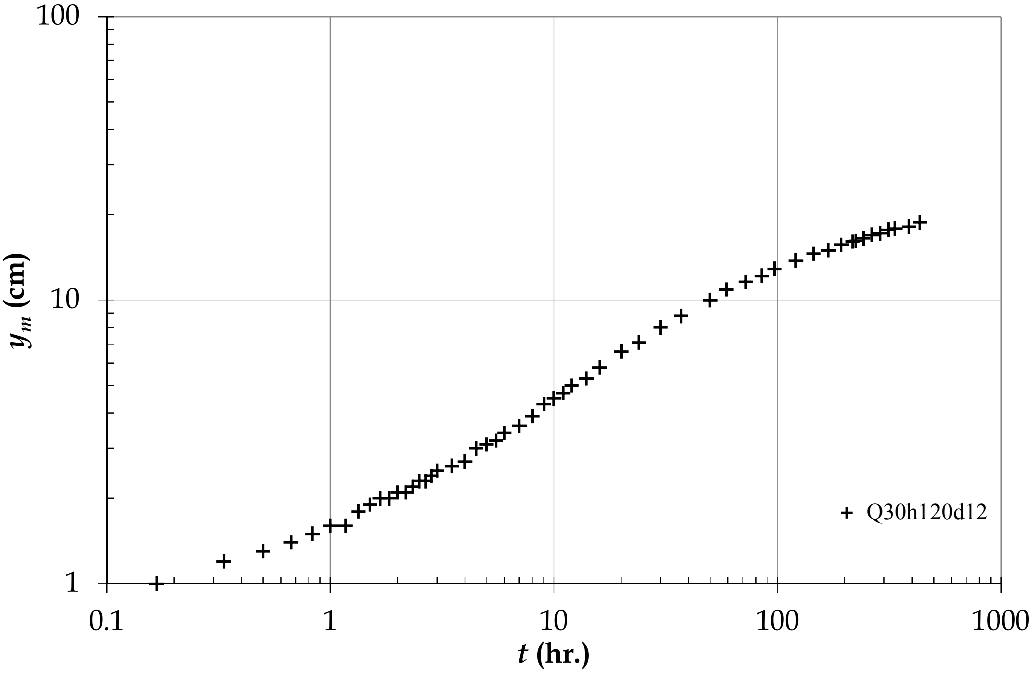

d) Q35h144d12

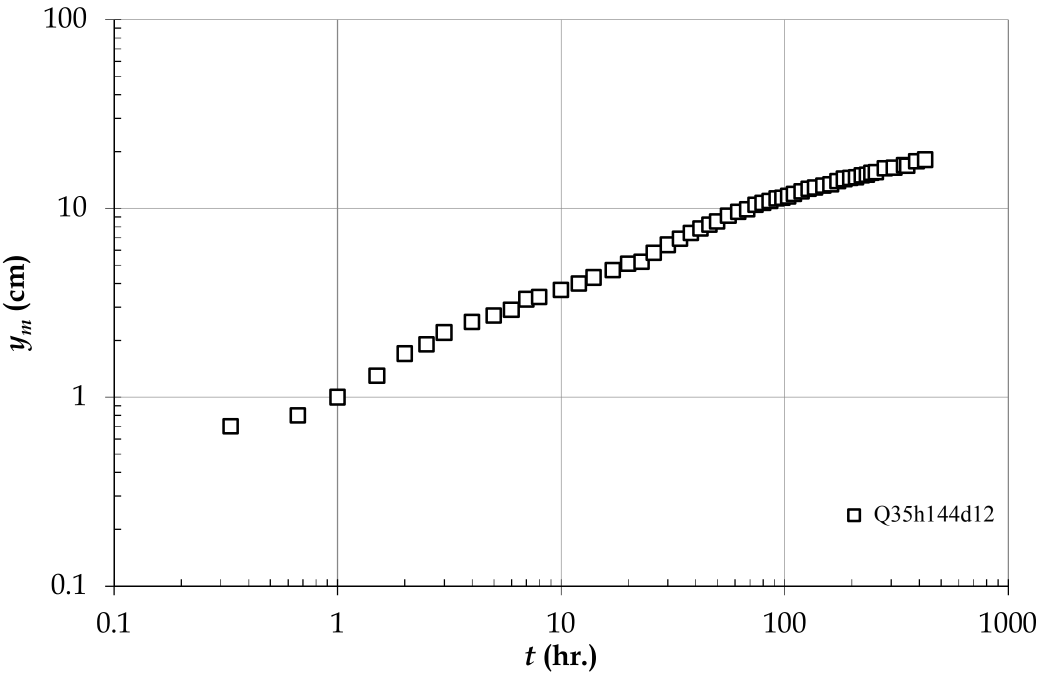

Figure 4.32 continued

e) Q35h120d12

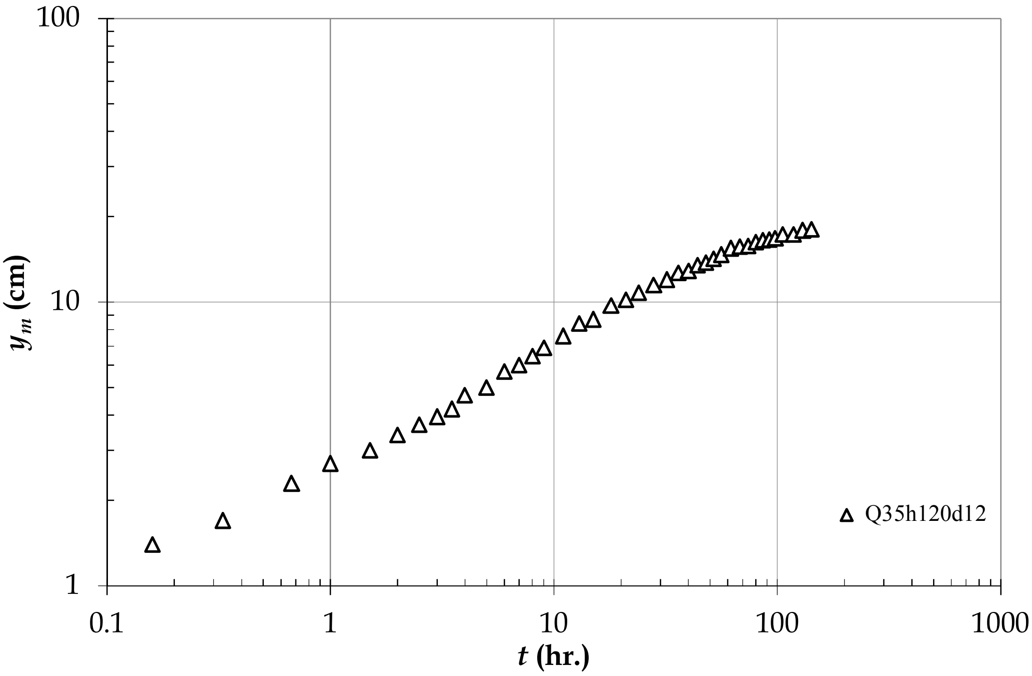

f) Q30h145d12

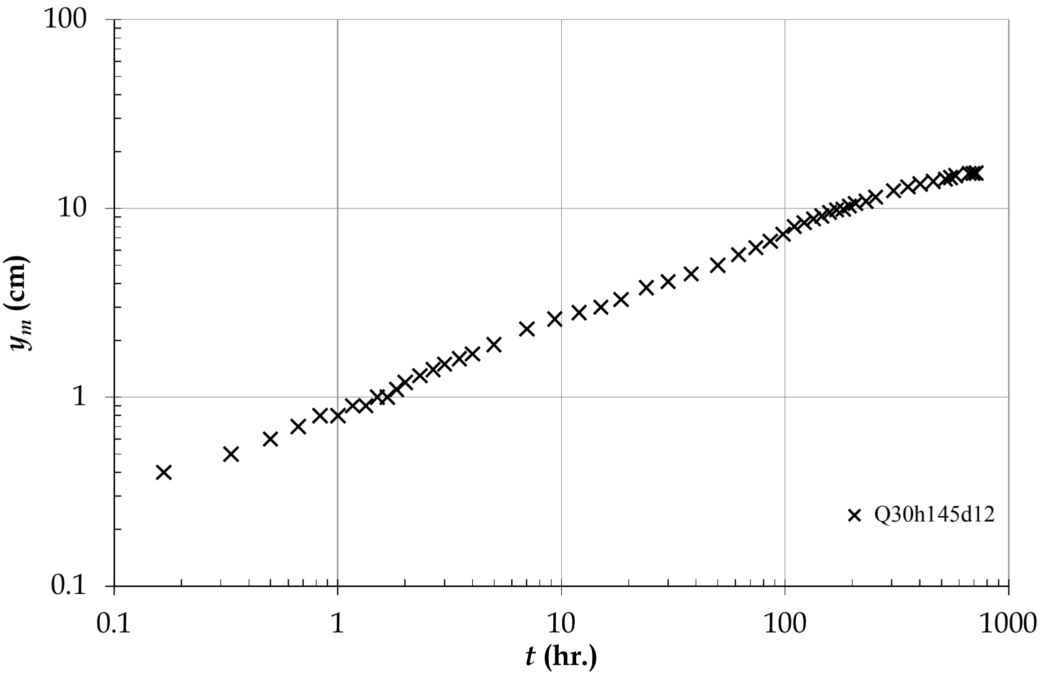

Figure 4.32 continued

g) Q20h120d06

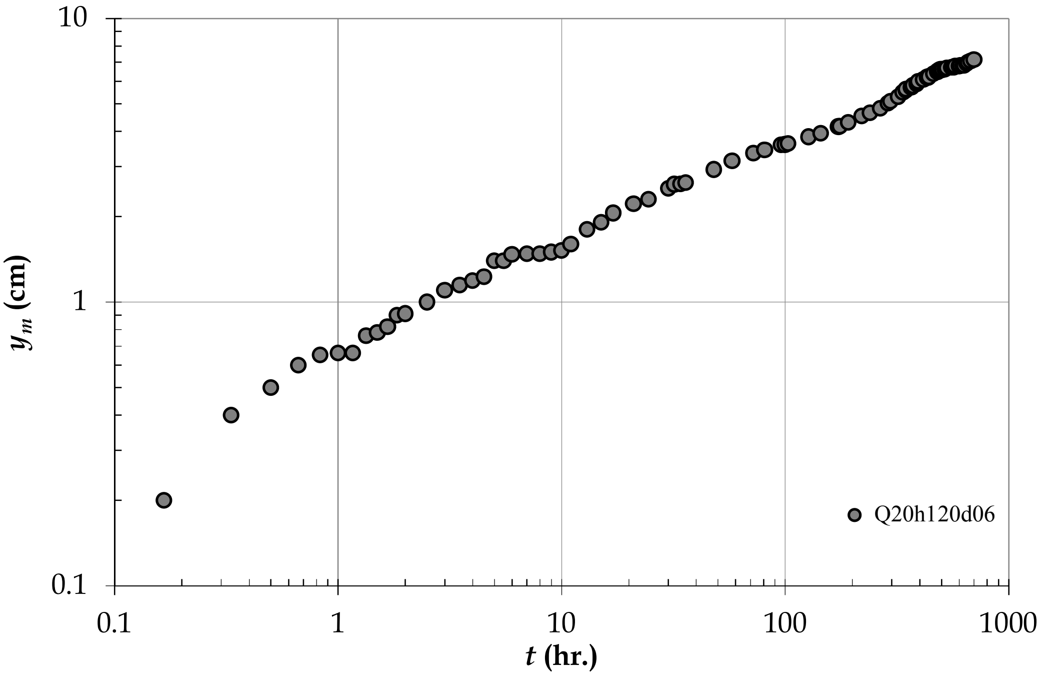

h) Q35h120d06

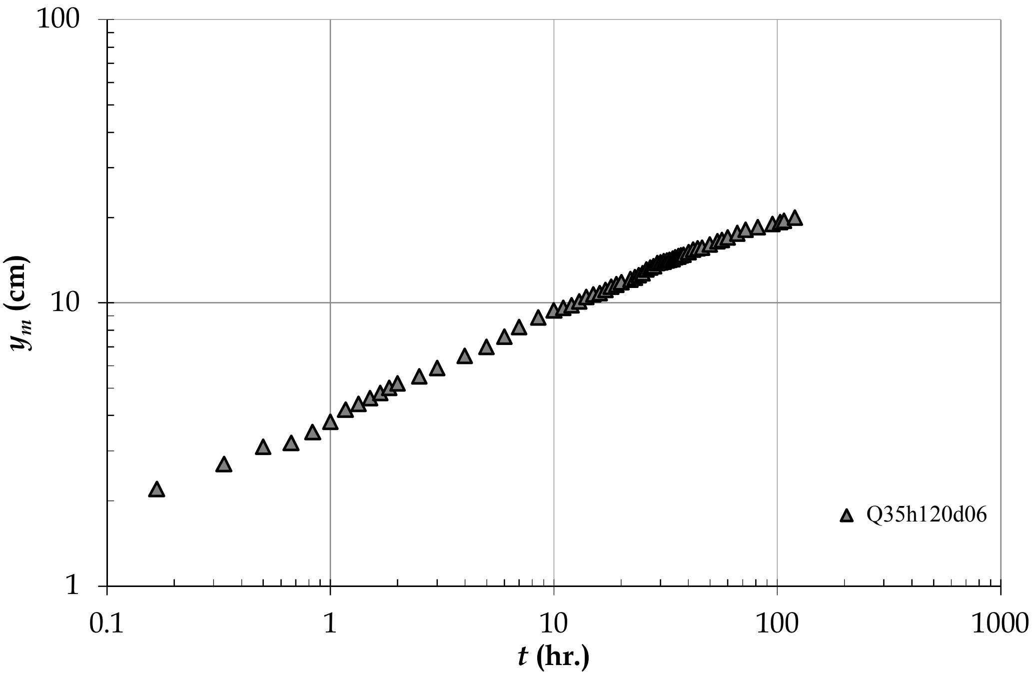

Figure 4.32 continued

i) Q35h150d06

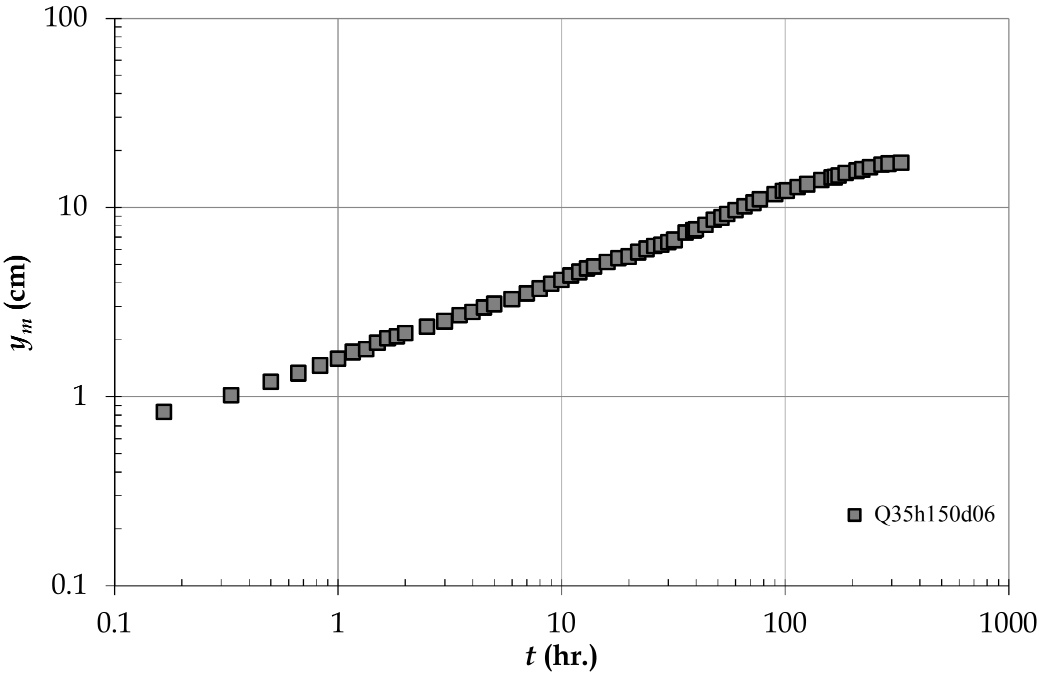

j) Q32h120d06

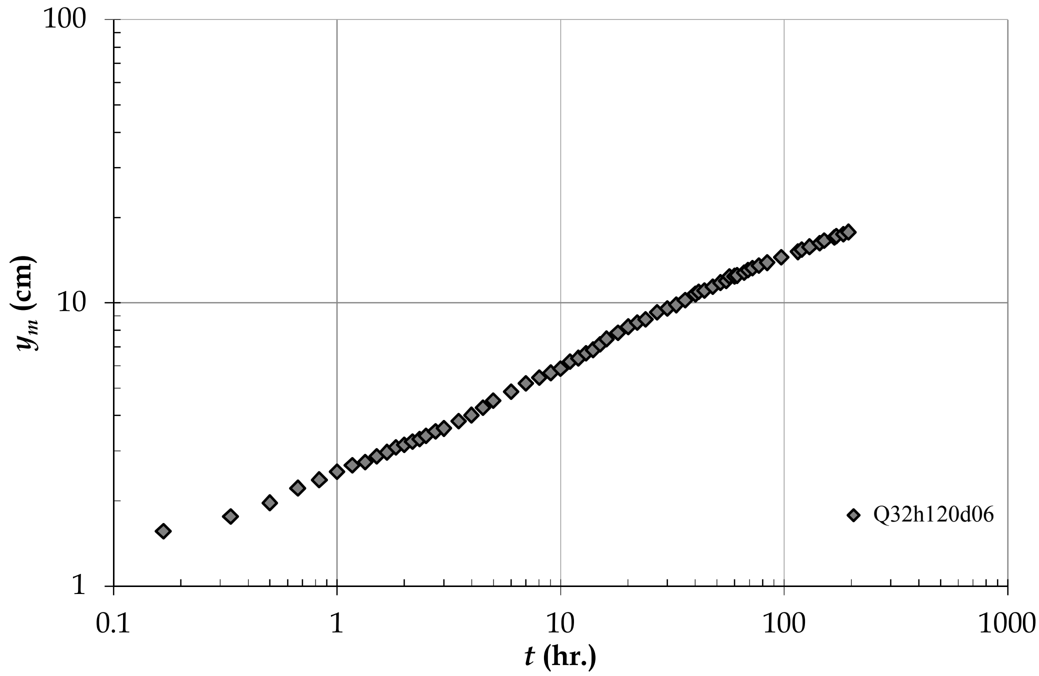

Figure 4.32 Continued

Table 4.7 Initial Parameters of Scour Test

case number	Flow Parameters					Sediment Parameters	
	U_0 (m/s)	Fr (-)	r_0 (-)	τ_0 (Pa)	Re_* (-)	k_s (mm)	D_* (m)
Q20h120d12	0.27	0.30	0.073	0.29	113	6	30.4
Q30h150d12	0.33	0.34	0.054	0.23	140	6	30.4
Q30h120d12	0.42	0.45	0.055	0.36	172	6	30.4
Q35h120d12	0.49	0.53	0.054	0.48	246	6	30.4
Q35h144d12	0.41	0.42	0.056	0.36	197	6	30.4
Q30h145d12	0.35	0.35	0.059	0.29	124	6	30.4
Q20h120d06	0.27	0.24	0.06	0.29	113	3	15.18
Q35h120d06	0.49	0.53	0.054	0.48	246	3	15.18
Q35h150d06	0.39	0.32	0.057	0.38	187	3	15.18
Q32h120d06	0.44	0.49	0.057	0.44	174	3	15.18

Table 4.8 Dominant Factors of Scour Test

case number	Chracteristic Scales			Equilibrium Prediction			
	$\delta_{*,\mathrm{m}}$ (mm)	λ (-)	t_λ (-)	$u_{*,c}$ (m/s)	U_c (m/s)	α_* (-)	$y_{m,e}$ (m)
Q20h120d12	0.27	0.30	0.073	0.021	0.26	1.88	0.121
Q30h150d12	0.33	0.34	0.054	0.023	0.30	1.98	0.178
Q30h120d12	0.42	0.45	0.055	0.022	0.28	2.4	0.31
Q35h120d12	0.49	0.53	0.054	0.0192	0.24	2.6	0.51
Q35h144d12	0.41	0.42	0.056	0.023	0.30	2.2	0.29
Q30h145d12	0.35	0.35	0.059	0.023	0.30	2.0	0.193
Q20h120d06	0.27	0.24	0.06	0.0182	0.26	1.82	0.108
Q35h120d06	0.49	0.53	0.054	0.0159	0.23	2.6	0.55
Q35h150d06	0.39	0.32	0.057	0.184	0.27	2.2	0.32
Q32h120d06	0.44	0.49	0.057	0.0171	0.24	2.5	0.42

And the relationship between normalized velocity and equilibrium-maximuim scour depth was plotted in Figure 4.33. This figure showed that the predicted $y_{m,e}$ of smaller d_{50}, were slightly larger than that of larger d_{50}. And also that of larger gaps of normalized velocity were remarkable larger than that of smaller gap of normalized velocity. Therefore, linear regression equation of its relationship is as follows:

$$\frac{y_m}{h_0} = \alpha_{m,e}\left(\frac{U_0 - U_c}{U_c}\right) + \beta_{m,e} \tag{4.16}$$

where $\alpha_{m,e}$ (= 3.3)and $\beta_{m,e}$ (0.64-0.96) are the calibration coefficient and intercept. Even the zero value of gaps normalized velocity can also make the scouring. Eq. 4.16 is applicable to the case, when it is not possible to estimate the turbulence properties at the longitudinal transion in field.

Normalized values of maximum scour depth and time of all cases were plotted and compared in Figure 4.34. And fractional exponents of scouring, γ was estimated as ~0.4, which was suggested by Hoffmans and Verheij (1997).

4.2.4 Equilibrium-maximum Scour Depth

Equilibrium state values of the maximum scour depth were estimatedfrom the suggestion of Dietz (1969) in Figure 4.33. And also it can be regressed with the following equation:

$$y_{m,e} / h_0 = 1.3\ln\left(C_{eq}\right) - 0.13 \tag{4.17-a}$$

$$C_{eq} = f\left(r_0, \mathrm{Fr}, \mathrm{Re}_*\right) = r_0 * \mathrm{Fr} * \mathrm{Re}_* \tag{4.17-b}$$

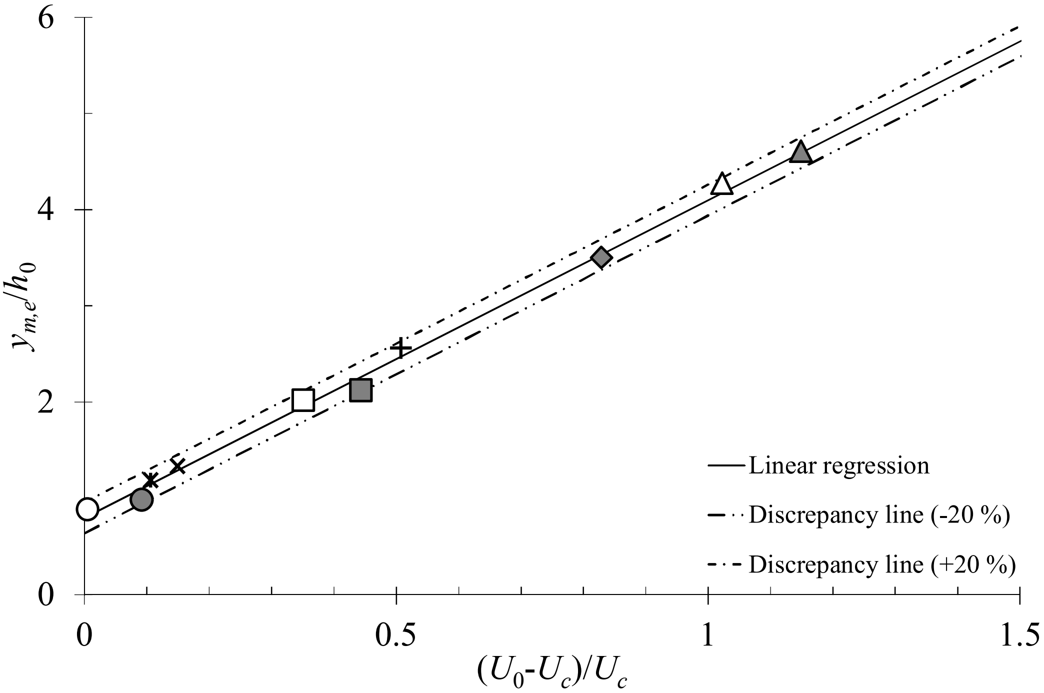

Figure 4.33 A Relationship of Normalized Velocity Difference and Equilibrium-maximum Scour Depth

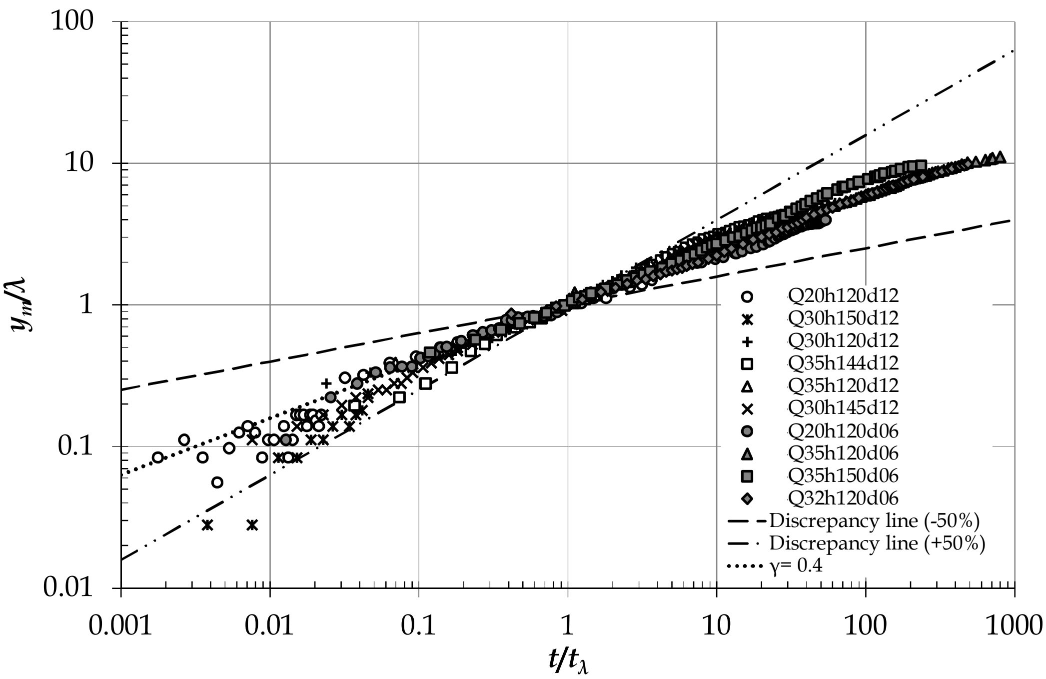

Figure 4.34 Relationship between the Normalized Maximum Scour Depth and Time

4.3 Flow and Turbulence in Scoured Hole

4.3.1 Flow Separation and Turbulent Shear Layer

Flow patterns at 245 hours later (approximately 10 days later) of case Q20h120d12 in the upstream scour slope were captured motion of fine particles for visualization in Figure 4.35. Flow velocity was faster in the vertically upper part ($z> \eta_0$) than in the lower part ($z< \eta_0$) of scoured hole. And in the lower part of upstream scour slope, a reverse and circulating movement of particles with relatively much slower than primary flow were shown.

To reveal the flow patterns in the upstream scour slope quantitatively, three-dimensional velocity data (measured for 30 seconds and ensemble-averaged as mentioned in the Chaper 3) were measured and analyzed in Figure 4.36. Flow velocity near the end of fixed bed were faster than in the scour hole with vertically uniform distribution. From the transition to 0.2 m, the reverse flow near the bed (2-10 mm from the bed) were measured with slower than in the upper part of scour hole as mentioned previously. Values of 3-D turbulence intensity were calculated and plotted in Figure 4.37 and reversal flow were compared with turbulent kinetic energy. Mostly, at 2 cm from the scoured hole, the values turbulent kinetic energy were estimated with excessively increased due to the larger values of velocity gradients and flow circulation. Maximum value of turbulent kinetic energy was estimated as 0.1 m^2/s^2) at the 0.26 m from the transition. According to the results by Breusers (1966), high turbulence intensities are possible in decelerating turbulent flows, due to the formation of layers with great velocity gradients in abrupt expansions of water depth. Also Hoffmans and Booij (1993-b) described turbulent mixing (or shear) layer in the scour hole with experimental data and numerical approaches. As they proposed, re- circulation (or reverse

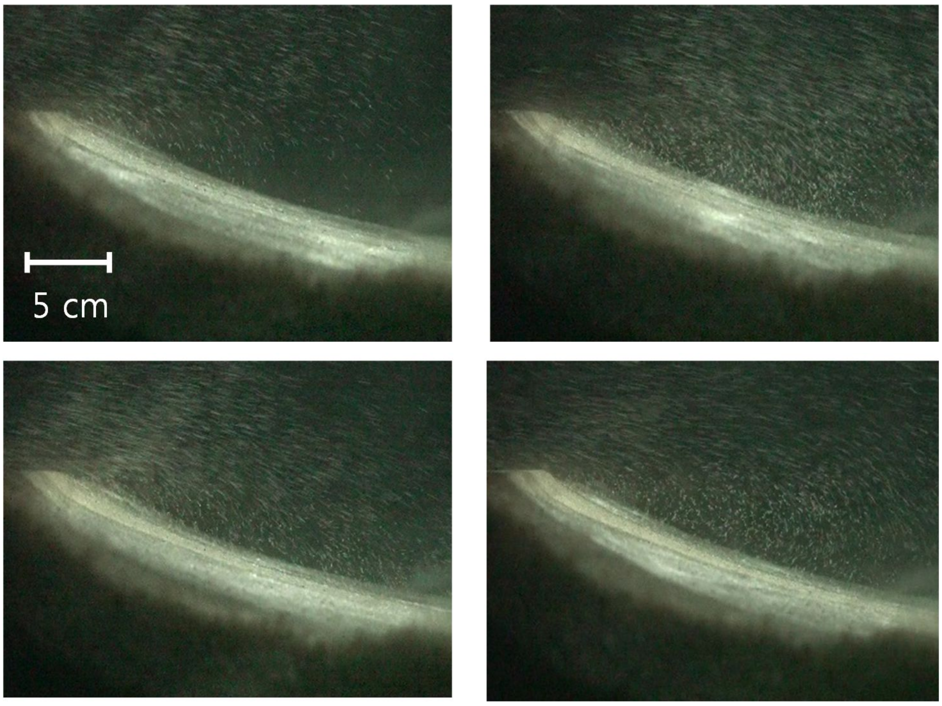

Figure 4.35 Snapshot of Visualization Particle in the Scoured Hole

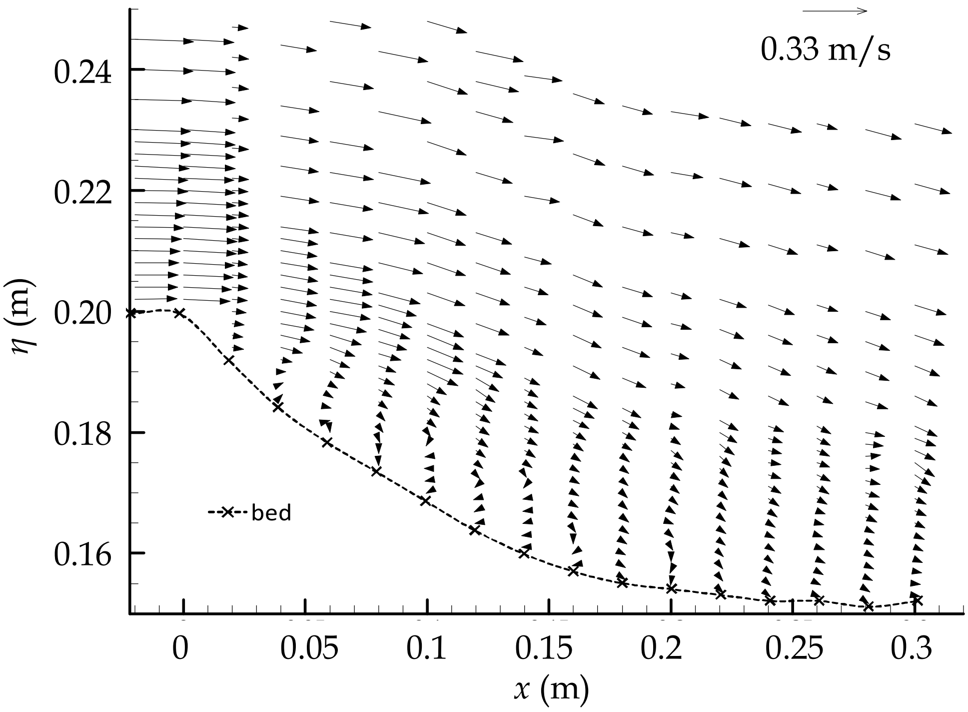

Figure 4.36 Two-dimensional Vector Profiles in Scoured Hole

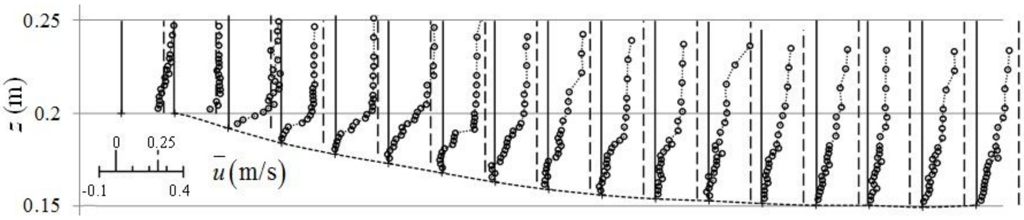

a) Stream-wise Mean Flow Velocity

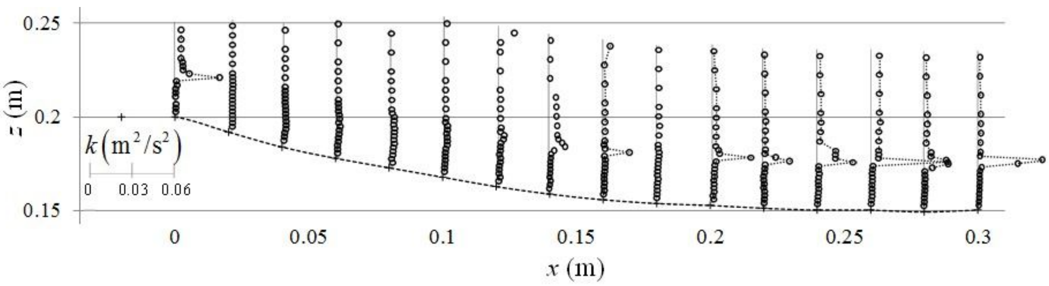

b) Turbulence Kinetic Energy

Figure 4.37 Distribution of Mean Flow and Turbulent Kinetic Energy in the Scoured Hole

movement) of flow in the upstream scour slope occurs near the bed and a mixing layer develops between the transient flow and the recirculating flow. In the beginning of the scour process, when the flow near the bed is not directed against the primary flow, a wake zone appears (Hoffmans and Booij, 1993-b). From the Figure 4.37 and 4.38, a reverse flow and abrupt increase of k (at 0.1 m from the bed) were measured in upstream scour hole. And these ultimate values of k were reflected in the turbulent shear layer in particular location with respect to the depth (Hoffmans and Booij, 1993-b).

Behind the transition, a lower region of mean velocity and turbulence intensity took place and the ultimate values were gradually developed at z= 2 cm (17 % of the h_0) from the scoured bed. And the maximum values of δ_{*m}, which represent a thickness of the turbulent mixing layer revealed by Hoffmans and Booij, 1993-b, was 1.1 cm (50 % of 0.09x) at x= 0.24 m from the transition.

4.3.2 Bed Shear Stress in Scoured Hole

Applying 2.52, values of bed shear stress in the scoured hole were calculated with 3-D velocity data at z= -2 mm from the bed at each longitudinal measuring grid and time steps. Longitudinal distributions of Reynolds shear stress and kinetic energy along the soured hole (case Q35h144d12) of each time step in Figure 4.38. in the upstream part of the maximum scour depth, values of turbulent kinetic energy were larger than in the downstream of it and decreased gradually toward the downstream. Values of Reynolds shear stress did not have excess differences between upstream and downstream of the maximum scour depth.

a) 221 hours later

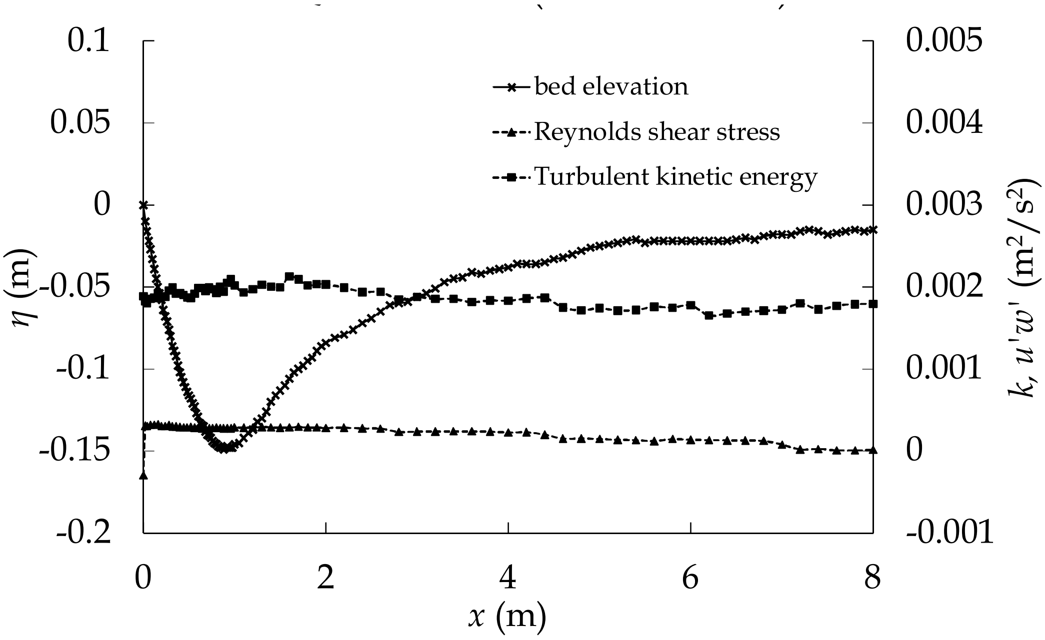

b) 245 hours later

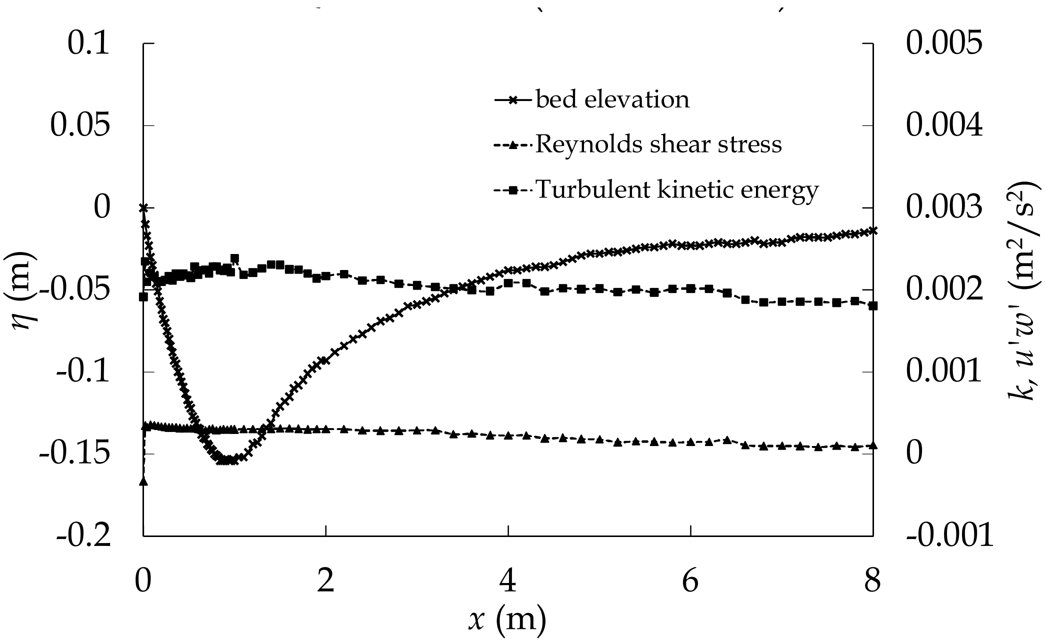

Figure 4.38 Temporal Change of Turbulence Properties near the Bed of Scoured Hole

c) 269 hours later

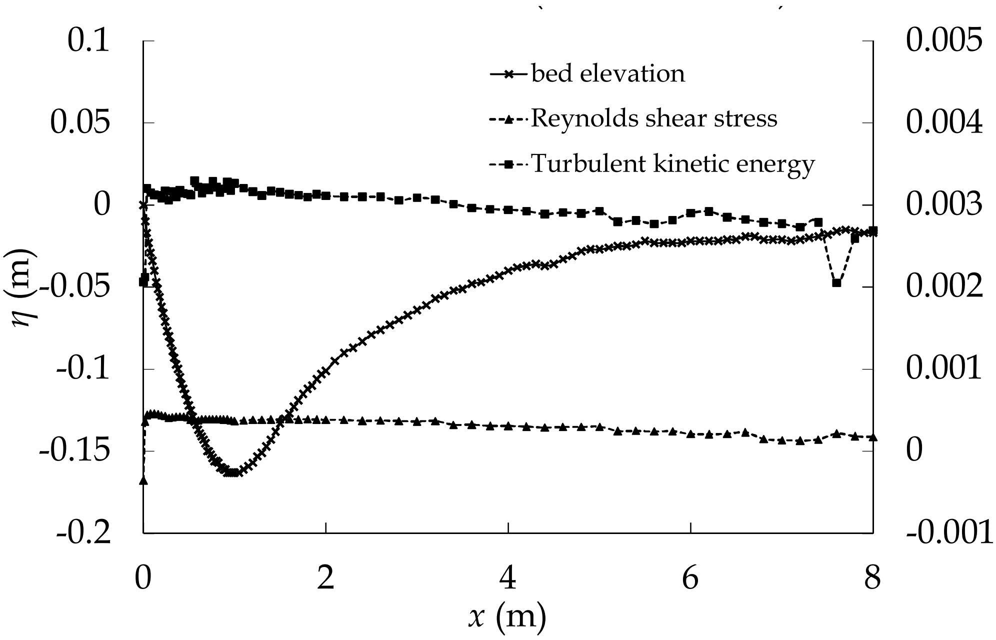

d) 365 hours later

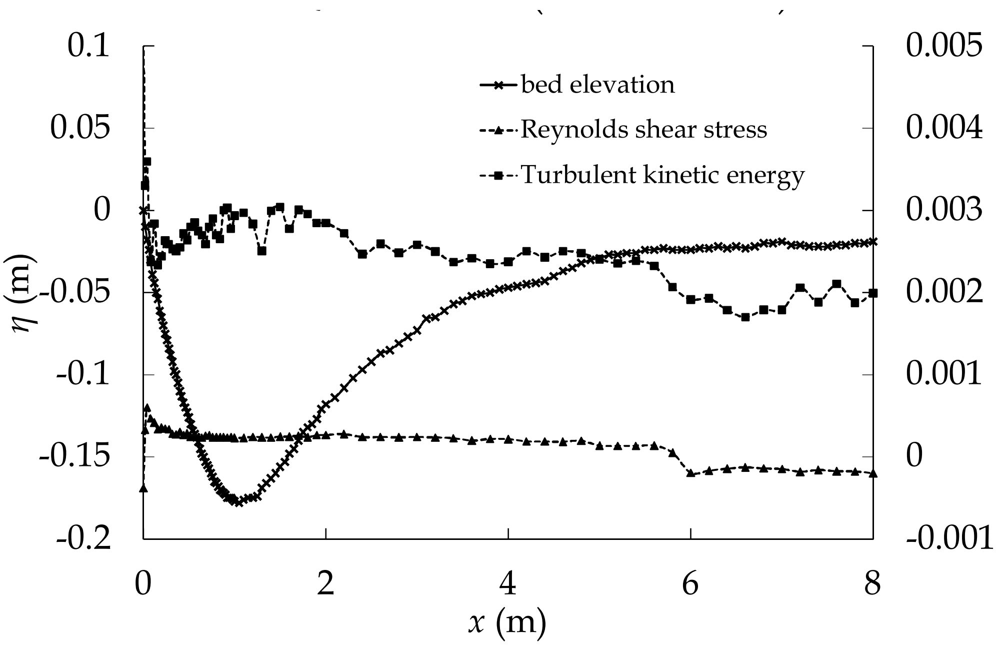

Figure 4.38 Continued

e) 401 hours later

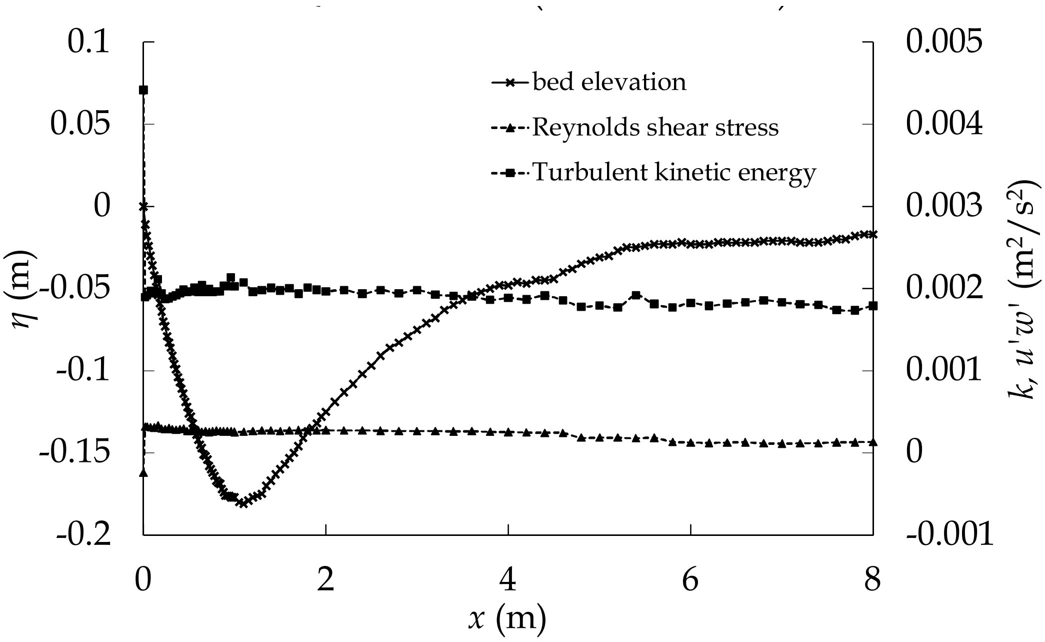

f) 437 hours later

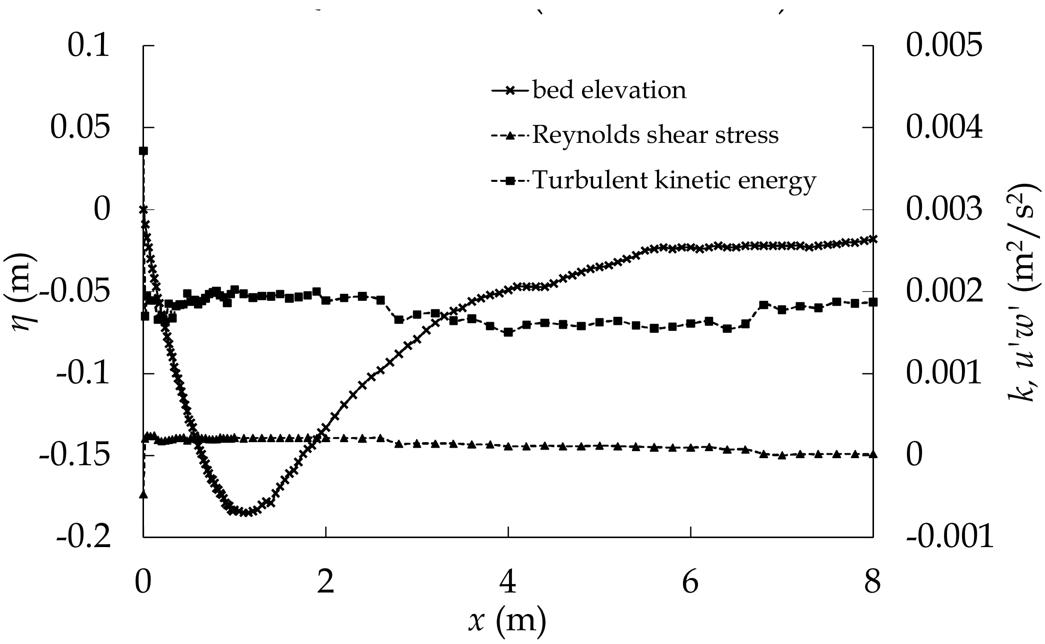

Figure 4.38 Continued

g) 473 hours later

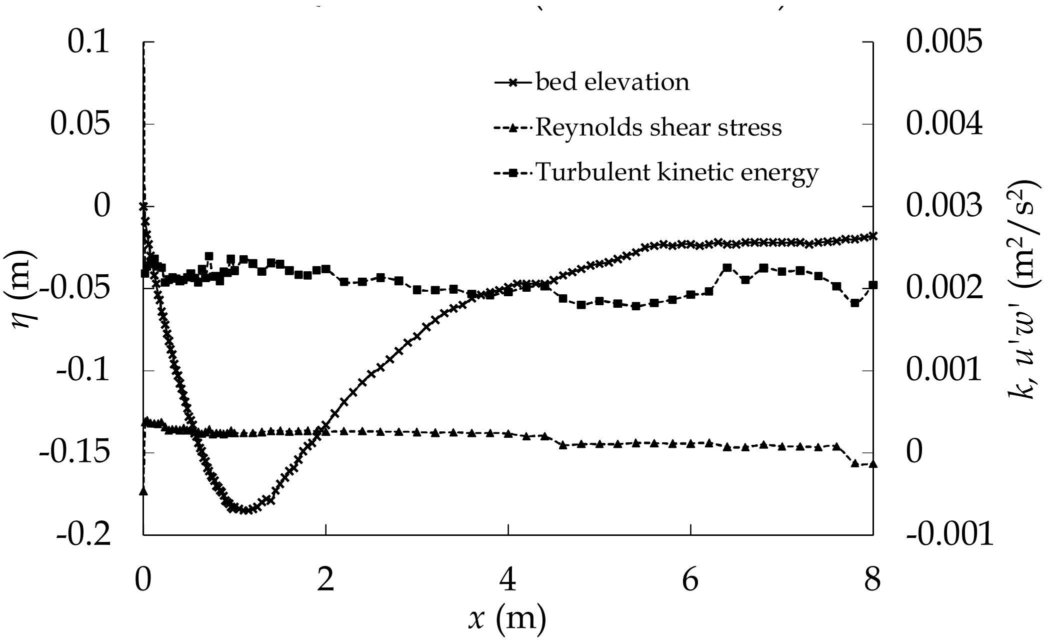

h) 509 hours later

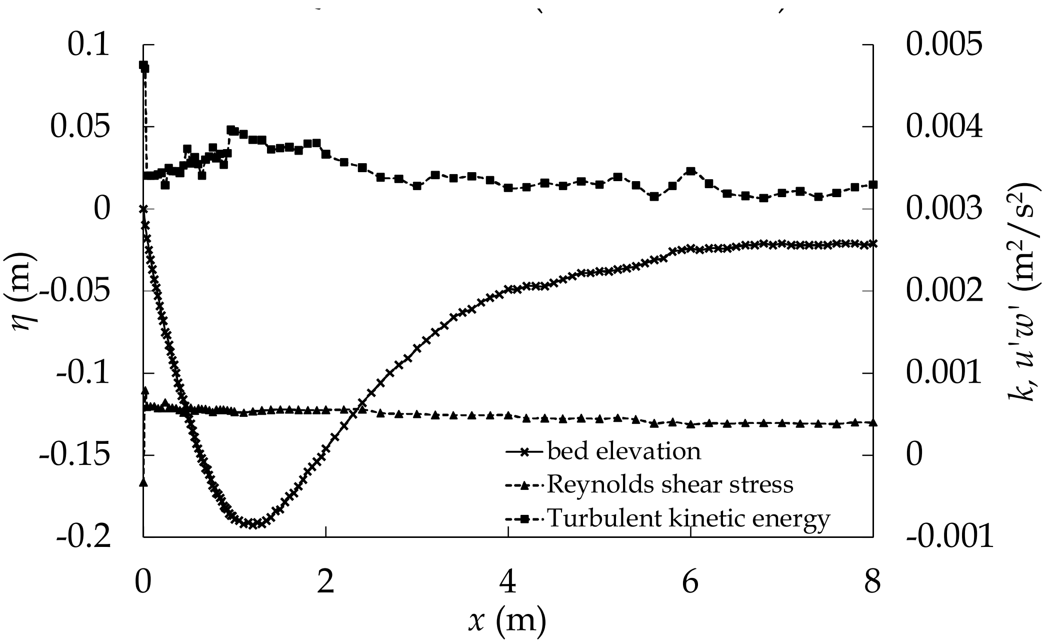

Figure 4.38 Continued

4.3.3 Energy Dissipation Rate

Hydraulic gradient, S_e is the slope of the hydraulic grade line (or mean energy slope) and it means the slope of the water surface in the open channel flow. For uniform flow conditions, estimating equation of S_e by Graf (1998) as follows:

$$S_e = \frac{2\nu U_0}{gR_h^{\ 2}} + \frac{u_*^{\ 2}}{gR_h} \tag{4.18}$$

Also Graf (1988) suggested the functional relationship between the friction coefficient of Darcy Weisbach equation, $f_{D,W}$ and depth-averaged relative turbulence intensity in open channel flows as follows:

$$f_{D,W} = 8\left(\frac{u_*}{U_0}\right)^2 = 5.6 r_0^{\ 2} \tag{4.19}$$

Substituting Eq. 4.19 into Eq. 4.18,

$$S_e = \frac{2\nu U_0}{gR_h^{\ 2}} + \frac{0.7\left(r_0 U_0\right)^2}{gR_h} \tag{4.20}$$

The first term on the RHS of Eq. 4.20 represents the influence of laminar flow which can be neglected with respect to the second term if Re>2,000.

With the condition of turbulent open channel flow, Eq. 4.20 can be re-written as

$$S_e(x) = \frac{0.7\left[r_0(x)U_0(x)\right]^2}{gR_h(x)} = \frac{0.7k_0(x)}{gR_h(x)} \tag{4.21}$$

Estimated values of energy slope (3 cases) were plotted with the values of bed elevation in Figure 4.39. Maximum value of S_e was $5.15*10^3$ and it was decreased gradually to the downstream of the scoured hole. Relationship between normalized energy slope and hydraulic radius was regressed as follows:

$$\frac{S_e(x)}{\eta(x)/\eta_0} = a_1\left[\frac{R_h(x)}{h_0}\right]^{a_2} \tag{4.22}$$

where a_1 (4.5-89) and a_2 (= 8.5) calibration coefficient and exponent, respectively (Figure 4.40). Errors were analyzed with the following methods in Figure 4.41.

$$RMSE = \sqrt{\frac{1}{N}\sum_{n=1}^{N}\left(x_{n,cal} - x_{n,mea}\right)^2} = 0.0045 \tag{4.23}$$

$$MAE = \frac{1}{N}\sum_{n=1}^{N}\left|x_{n,cal} - x_{n,mea}\right| = 0.003 \tag{4.24}$$

$$AGD = \left[\prod_{n=1}^{N} R_n\right]^{1/N} = 1.0992 \tag{4.25}$$

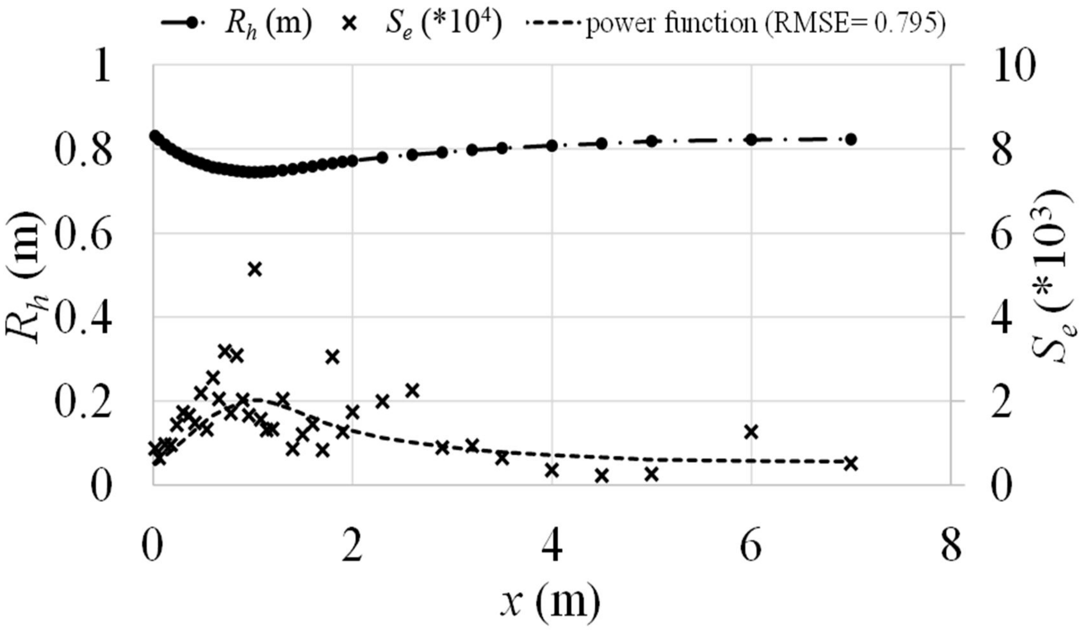

Figure 4.39 Longitudinal Distribution of Energy Slope in the Scoured Hole

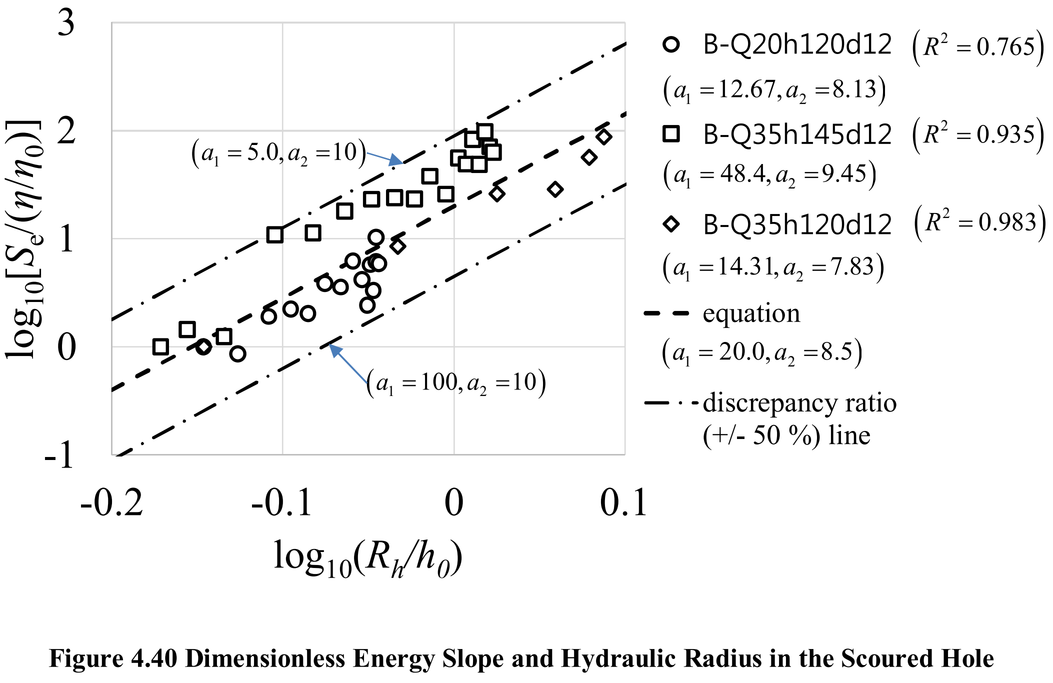

Figure 4.40 Dimensionless Energy Slope and Hydraulic Radius in the Scoured Hole

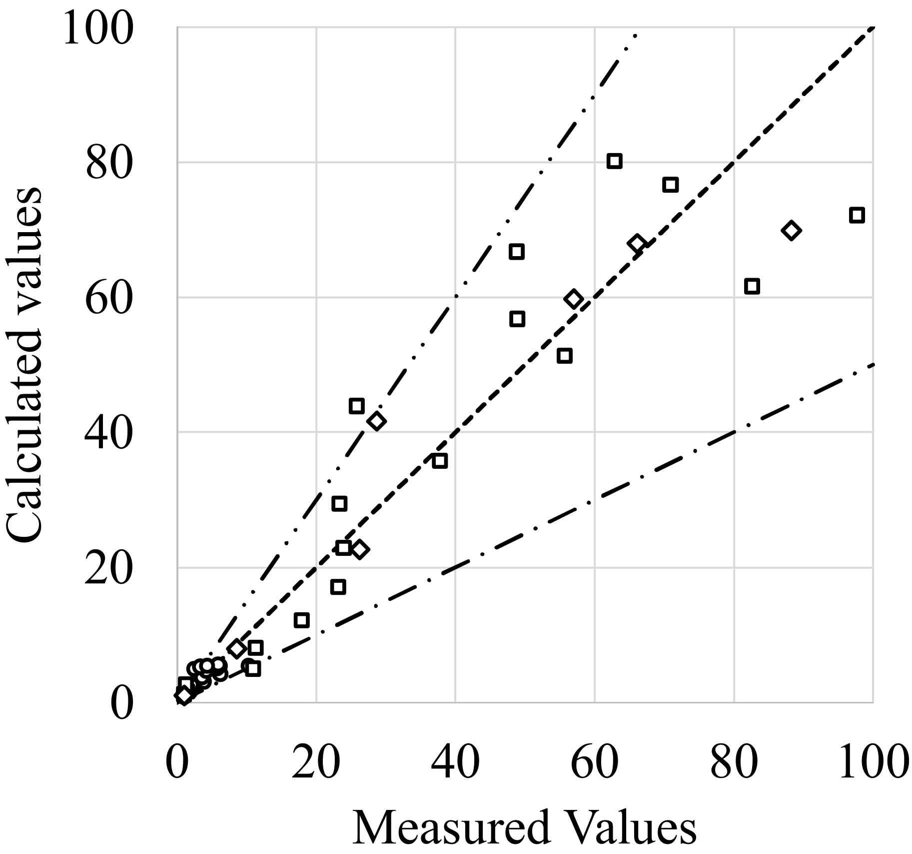

Figure 4.41 Error Analysis of Empirical Equation of Energy slope

4.3.4 Flow and Turbulence Distribution in the Scoured Hole

Three dimensional velocity data were measured and analyzed spatially in the scoured hole, which was mostly stabilized for each 4 cases. At the upstream part from the L_1, relatively dense distributions (Δx= 2 cm) were setup and downstream part from the L_1, relatively coarse distribution (Δx= 5-50 cm) of measuring grid points were setup respectively. And also vertical intervals of measuring grid were from 2 mm to 5-20 mm from the scoured bottom (Figure 4.42).

As metioned in Chapter 2.3, measured flow data can be spiked due to the mistakes of the sensor configuration in the zones of spatially varied flow and occasionally undesirable particle moving. Figure 4.43 showed the contaminated and filtered values of the stream-wise directional velocity data in time domain. Also Figure 4.44 showed the spiked values with the confidence ellipses and filtered values of the instantaneous velocity in the confidence ellipses.

With the despiking procedure, flow velocity and turbulence properties were plotted in Figure 4.45. Distributions of stream-wise velocity, which dominantly affects the sediment transport of bed matrials, were analyzed that relatively high valued in the upper layer from the scoured hole. And near the bottom, reversal flow were analyzed like that in the backward facing step flow. Excessively large values of the velocity gradients of the stream-wise velocity made the turbulent shear layer, which also can affect the undesirable motion of bed materials. According to the results of the previous researches, this remarkable distribution of TKE is due to the large differences of the stream-wise velocity to the water depth direction. There is a slightly cyclic motion of the flow and it will be stretched to the depth and dissipated to the downstream.

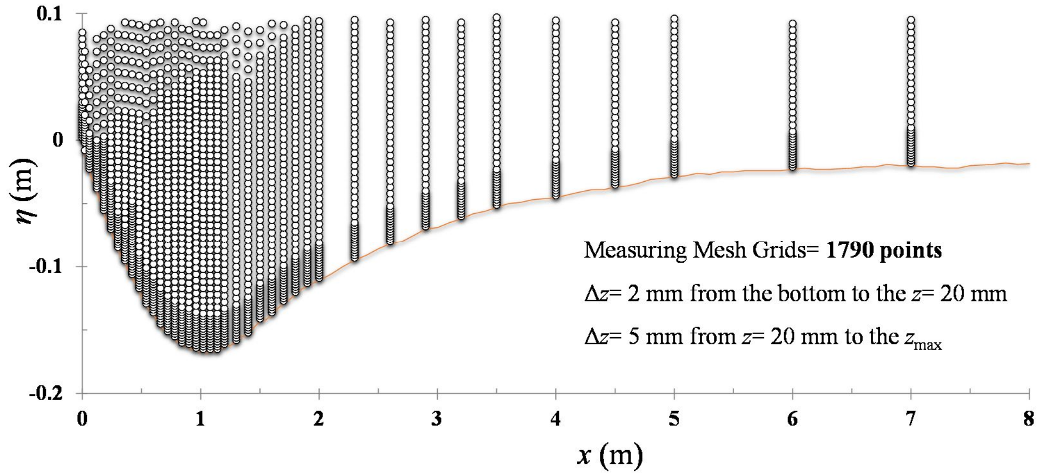

Figure 4.42 Distribution of Measuring Grid Points in Scoured Hole

(case B-Q35h144d12; at *t*= 330 hrs. later)

a) Δu vs. u

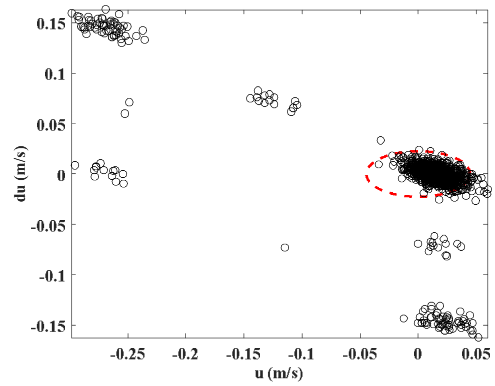

b) $\Delta^2 u$ vs. Δu

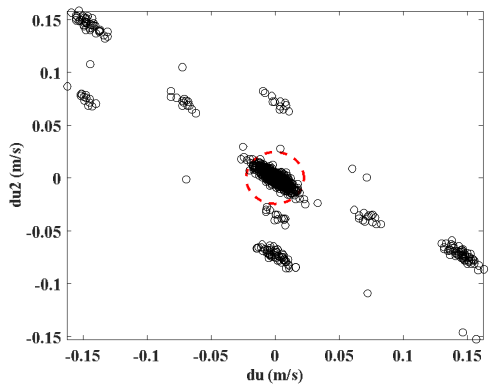

c) $\Delta^2 u$ vs. u

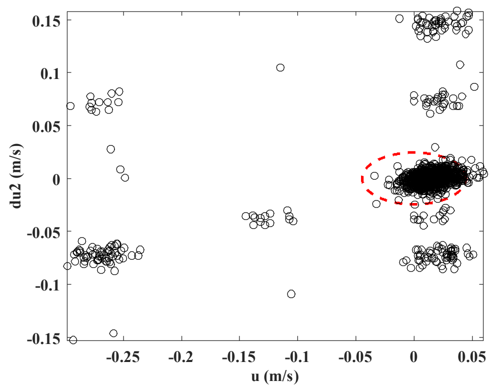

Figure 4.43 Spiked Values of Velocity Data and Confidence Ellipses

a) Δu vs. u

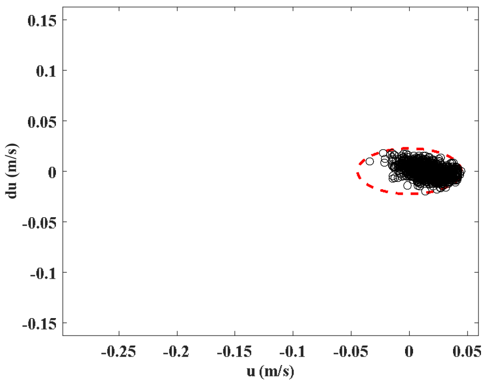

b) Δ^2u vs. Δu

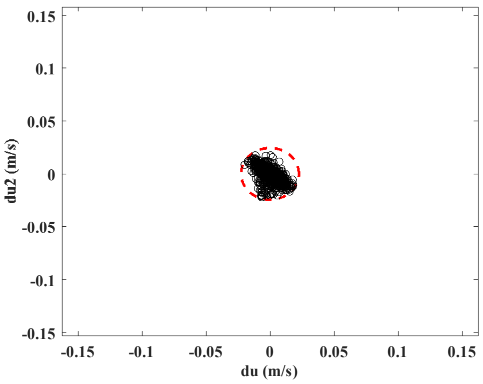

c) Δ^2u vs. u

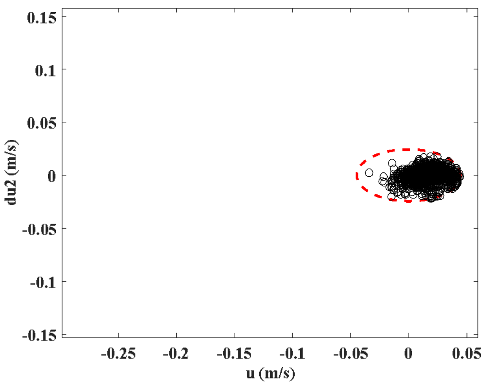

Figure 4.44 Filtered Values of Velocity Data and Confidence Ellipses

a) Stream-wise velocity distribution

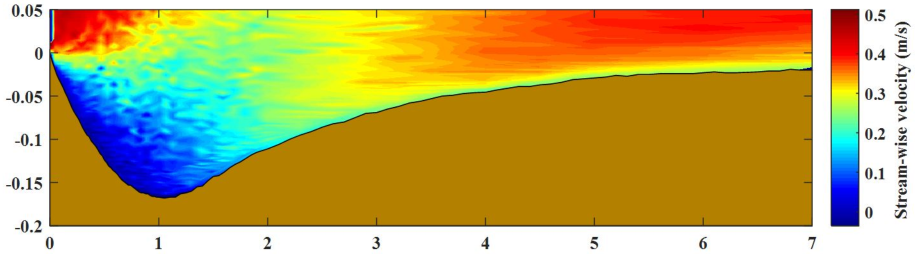

b) Reynolds shear stress distribution

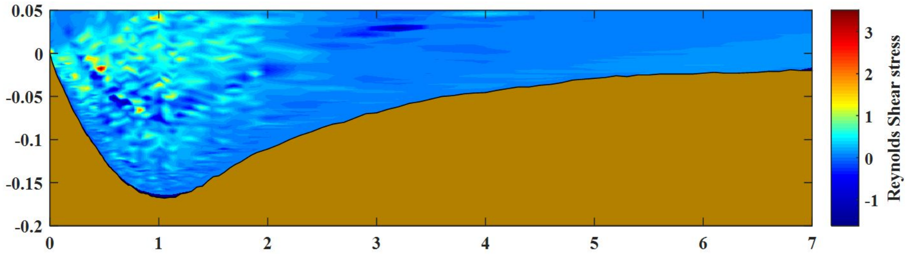

c) Turbulent Kinetic Energy distribution

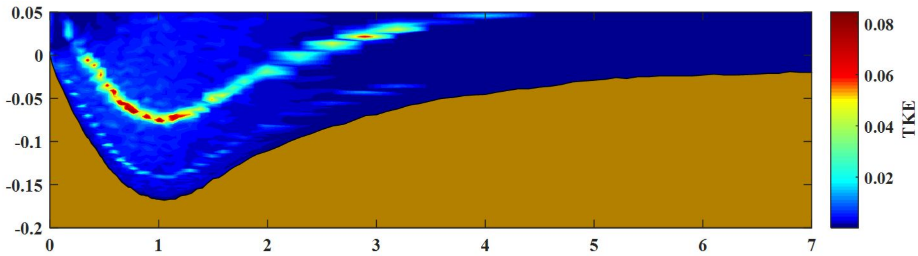

Figure 4.45-a) Flow and Turbulence Distributions in Stablized Scoured Hole

(case B-Q35h144d12; at *t*= 330 hrs. later)

a) Stream-wise velocity distribution

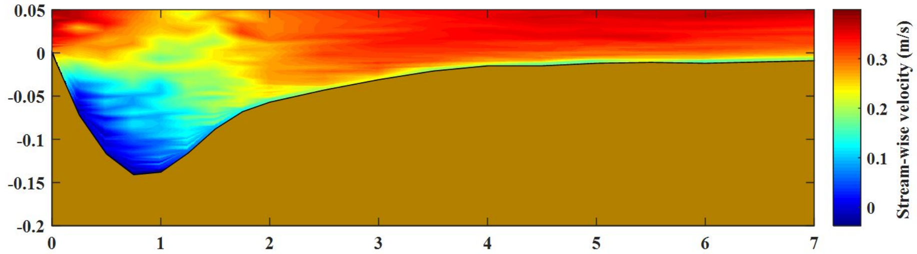

b) Reynolds shear stress distribution

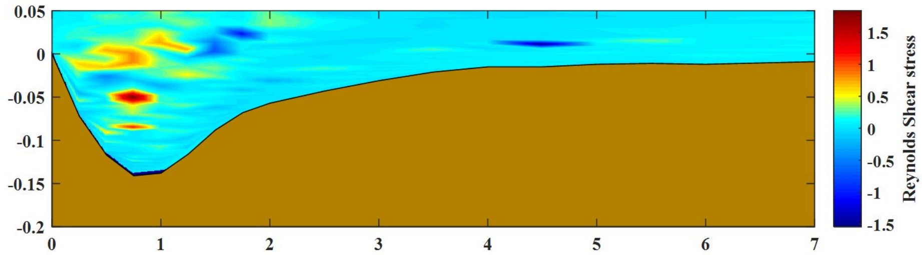

c) Turbulent Kinetic Energy distribution

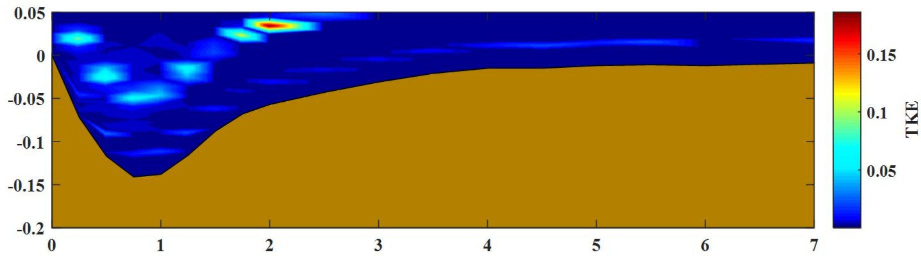

Figure 4.45-b) Continued (Case B-Q30h145d12)

a) Stream-wise velocity distribution

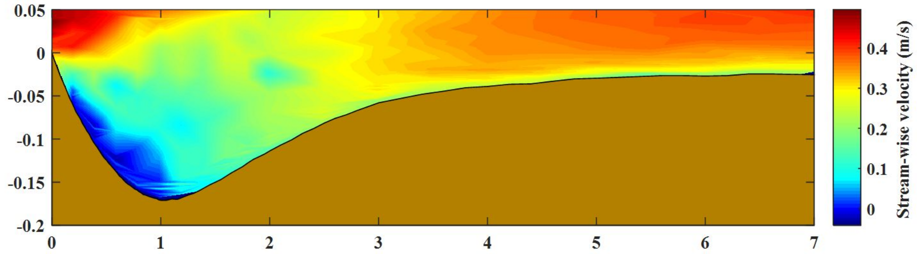

b) Reynolds shear stress distribution

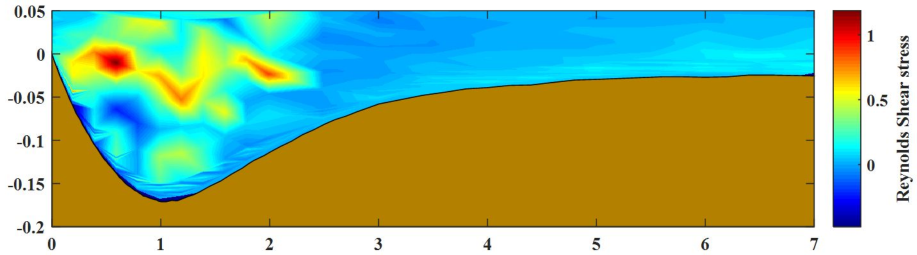

c) Turbulent Kinetic Energy distribution

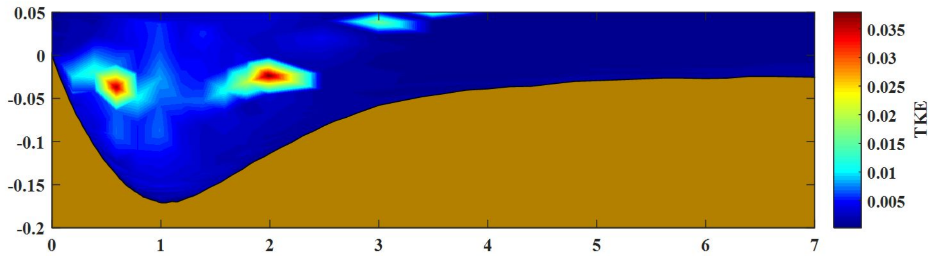

Figure 4.45-c) Continued (Case B-Q30h120d12)

a) Stream-wise velocity distribution

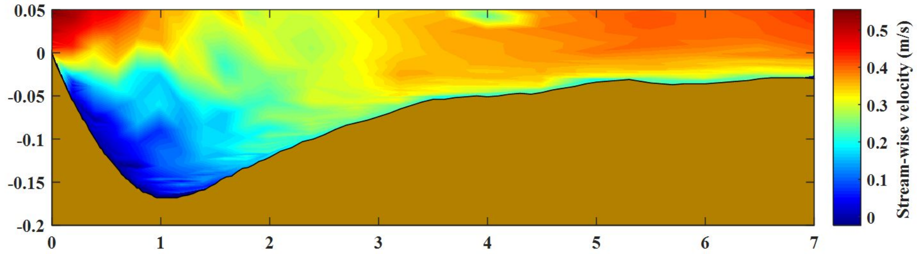

b) Reynolds shear stress distribution

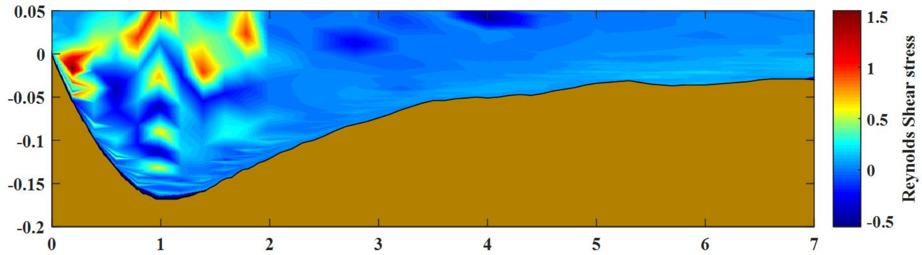

c) Turbulent Kinetic Energy distribution

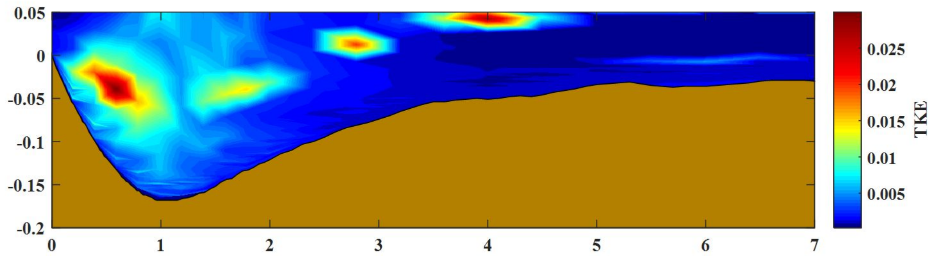

Figure 4.45-d) Continued (Case B-Q35h120d12)

With data of the time averaged velocity, vorticity and three dimensional velocity data were measured and analyzed spatially in the scoured hole, which was mostly stabilized for each 4 cases. At the upstream part from the L_1, relatively dense distributions (Δx= 2 cm) were setup and downstream part from the L_1, relatively coarse distribution (Δx= 5-50 cm) of measuring grid points were setup respectively. And also vertical intervals of measuring grid were from 2 mm to 5-20 mm from the scoured bottom (Figure 4.42).

CHAPTER 5

LOCAL SCOURING WITH MESH GRID GENERATED TURBULENT FLOW

5.1 Experimental Setup

Previously, turbulence properties at the transition is one of the dominant factors on local scouring at the downstream of the fixed. In this chapter, to analyze the effect of the turbulence at the upstream of the transition, scour tests were conducted with a setup of rectangular shape meshed wall (fully blocked along the width of the cross section). Flow pattern with this mesh grid is named as mesh grid generated turbulent flow (MGGT flow) and it can make the increase of the turbulence properties at the longitudinal transition. Schematic diagram of this setup was decribed in Figure 5.1.

5.2 Comparison of Flow and Turbulence at the Transition

Firstly, 3-D flow velocity data were measured at the transition in MGGT flow and analyzed with same methods, which were applied in Chapter 4. Hydraulic conditions of the test were described in Table 5.1. The range of the Froude number is from 0.256 to 0.448 and that of mean flow velocity is from 0.278 to 0.486.

Configurations of measuring flow velocity in MGGT Test were same as those in no meshed flow. Estimated values of the tests were noted in Table 5.2 and compared with the data from the no meshed flow in previous chapter (Figure 5.2 and 5.3).

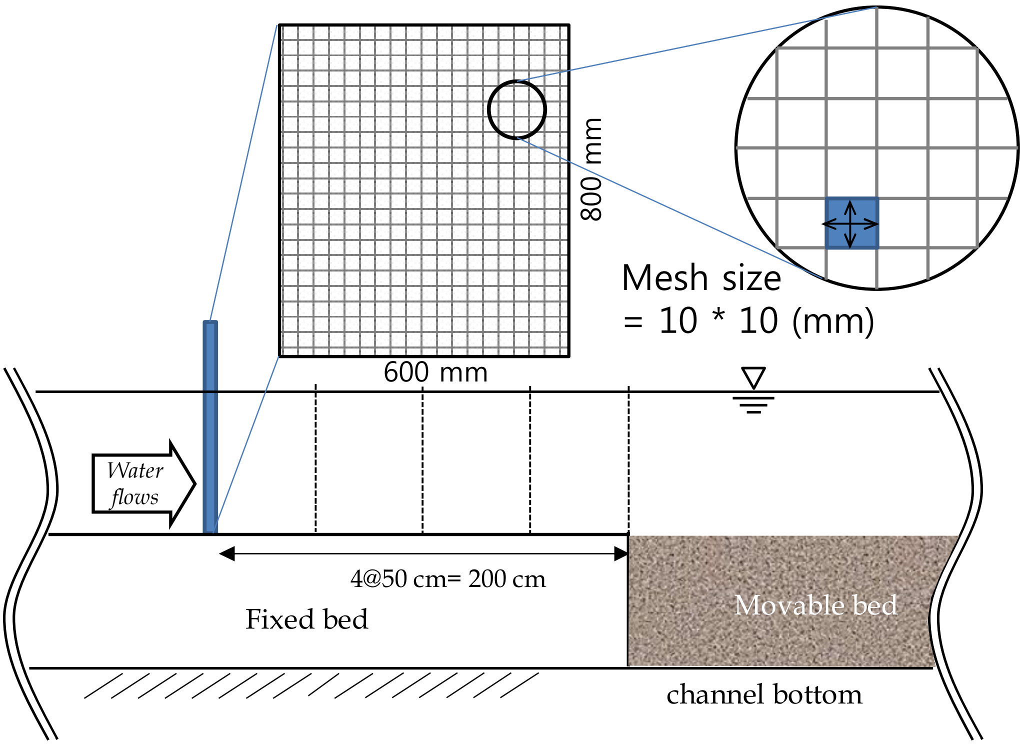

Figure 5.1 Schematic Diagram of MGGT Flow and Scour Test

Table 5.1 Experimental Conditions of MGGT Flow Test at Longitudinal Transition

case number	Q (m^3/s)	h_0 (m)	U_0 (m/s)	Fr (-)	Re ($*10^5$)
Q20h320	0.030	0.150	0.278	0.256	0.333
Q30h320	0.035	0.120	0.417	0.384	0.500
Q30h350	0.030	0.145	0.333	0.274	0.500
Q32h320	0.020	0.120	0.444	0.410	0.533
Q35h320	0.035	0.120	0.486	0.448	0.583
Q35h350	0.035	0.150	0.405	0.341	0.583

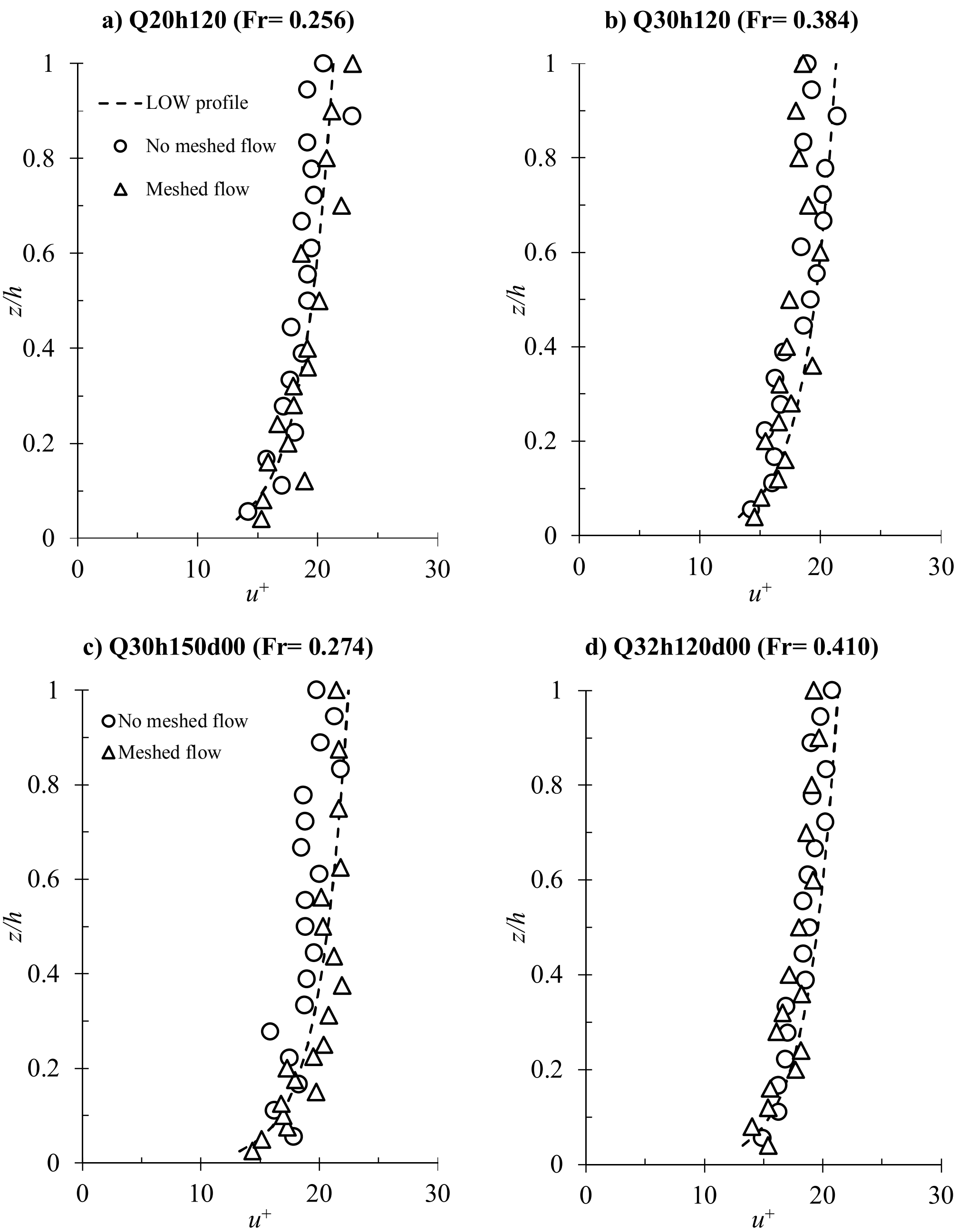

Figure 5.2 Comparisons of LOW Methods at the Transition

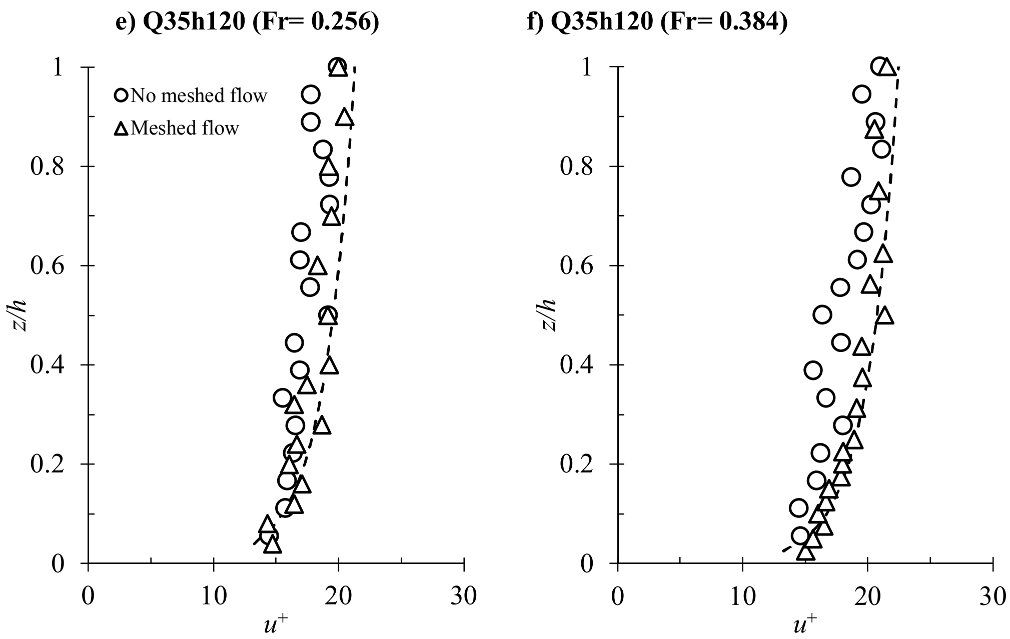

Figure 5.2 Continued

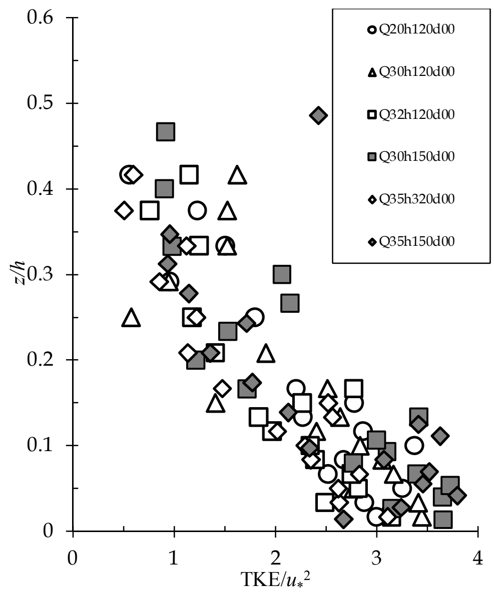

Figure 5.3 Comparisons of TKE Methods at the transition

Table 5.2 Hydraulic Conditions of MGGT Flow Test

case	U_0 (m/s)	Fr (-)	LOW method				TKE method
			τ_0 (Pa)	δ_* (mm)	U_{free} (m/s)	Re_* $*10^{-3}$ (-)	r_0 (-)
Q20h120	0.28	0.26	0.23	8.4	0.35	127	0.063
Q30h320	0.42	0.38	0.63	12.2	0.59	306	0.056
Q30h350	0.33	0.27	0.32	12.2	0.43	221	0.053
Q32h320	0.44	0.41	0.68	11.8	0.61	307	0.058
Q35h320	0.49	0.45	0.84	11.0	0.68	318	0.043
Q35h350	0.41	0.34	0.44	16.3	0.50	342	0.036

5.3 Comparison of Local Scouring

5.3.1 Temporal Development of Local Scour Hole

Three cases of scour test in MGGT flow condition were conducted and compared with those of no meshed flow condition at the upstream (Table 5.3). Median grain size of movable bed is 0.6 mm. Developments of scoured hole at each time step were similar with those of no meshed flow. Especially, a group of ripples were moving toward downstream of the maximum scour depth like same case with no meshed flow (case Q20h120d06). Scouring also of the case Q35h150d06 is similar. However frequency of the rippled bed in MGGT flow condition is smaller than no meshed flow condition (Figure 5.4).

5.3.2 Maximum Scour Depth

Development of ym in MGGT flow is slightly smaller than that of no meshed flow condition and difference in the case Q20h120d06 is largest among those experimental cases.

Table 5.3 Experimental Conditions of MGGT Scour Test

case number	Q (m^3/s)	h_0 (m)	U_0 (m/s)	Fr (-)	Re (*10^5)
Q20h120	0.030	0.150	0.278	0.256	0.333
Q35h320	0.035	0.120	0.486	0.448	0.583
Q35h350	0.035	0.150	0.405	0.341	0.583

a) Q20h120d06

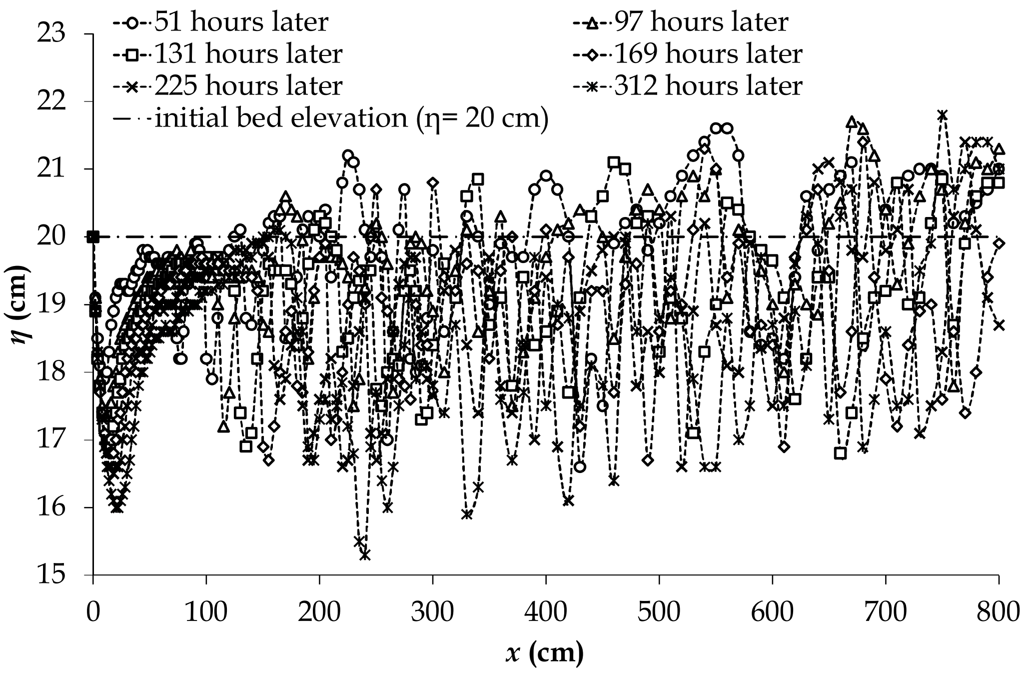

b) Q35h120d06

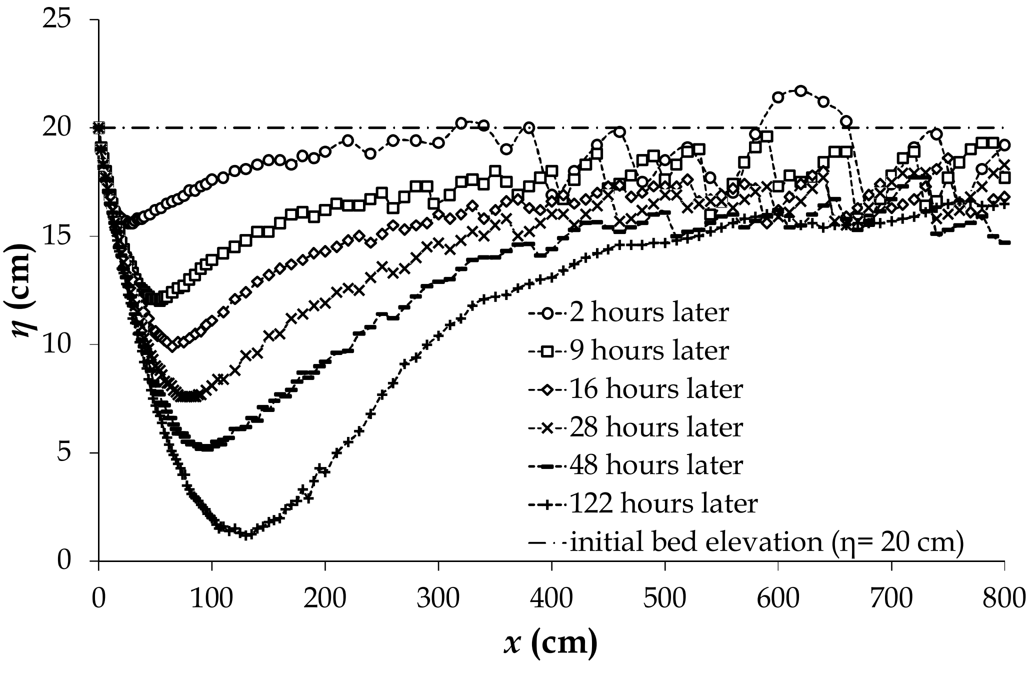

Figure 5.4 Temporal Change of Bed Profiles in MGGT Flow Condition

c) Q35h150d06

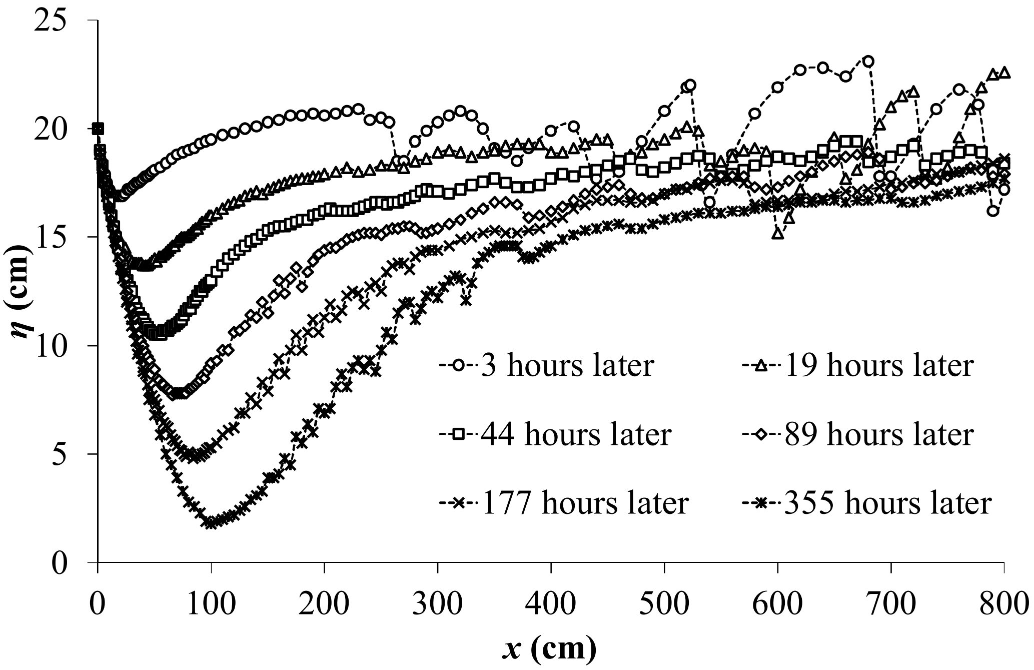

Figure 5.4 Continued

a) Q20h120d06

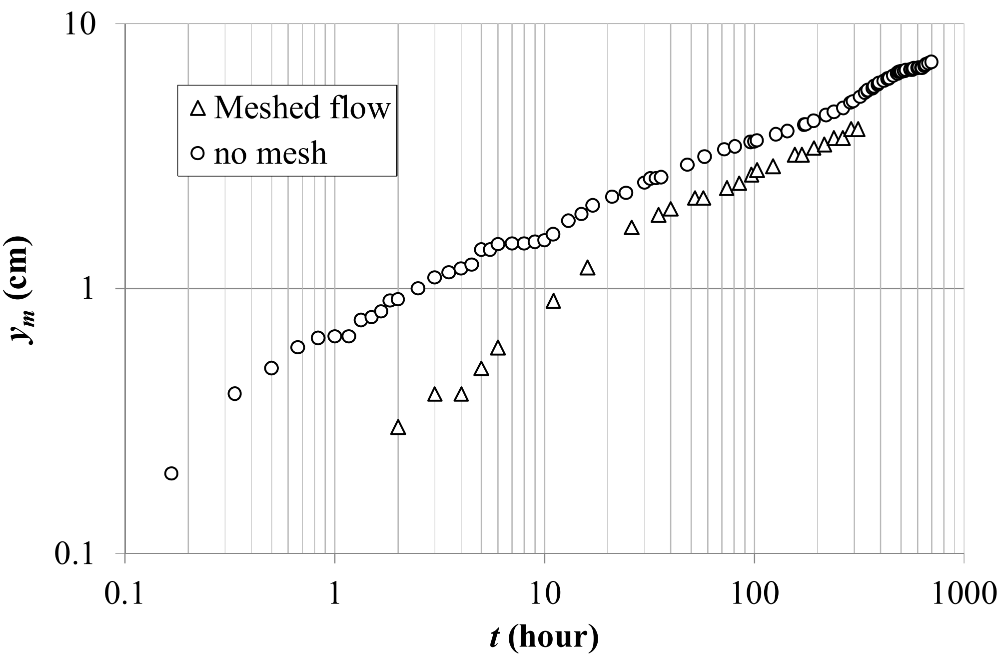

Figure 5.5 Comparisons of the Temporal Development of Maximum Scour Depth

b) Q35h120d06

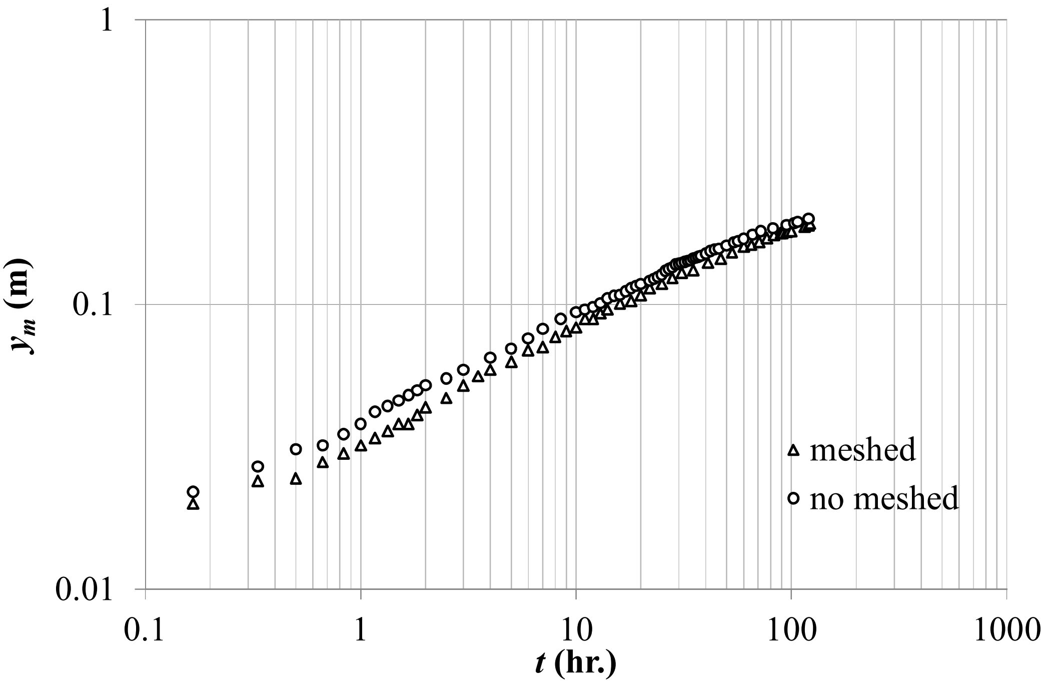

c) Q35h150d06

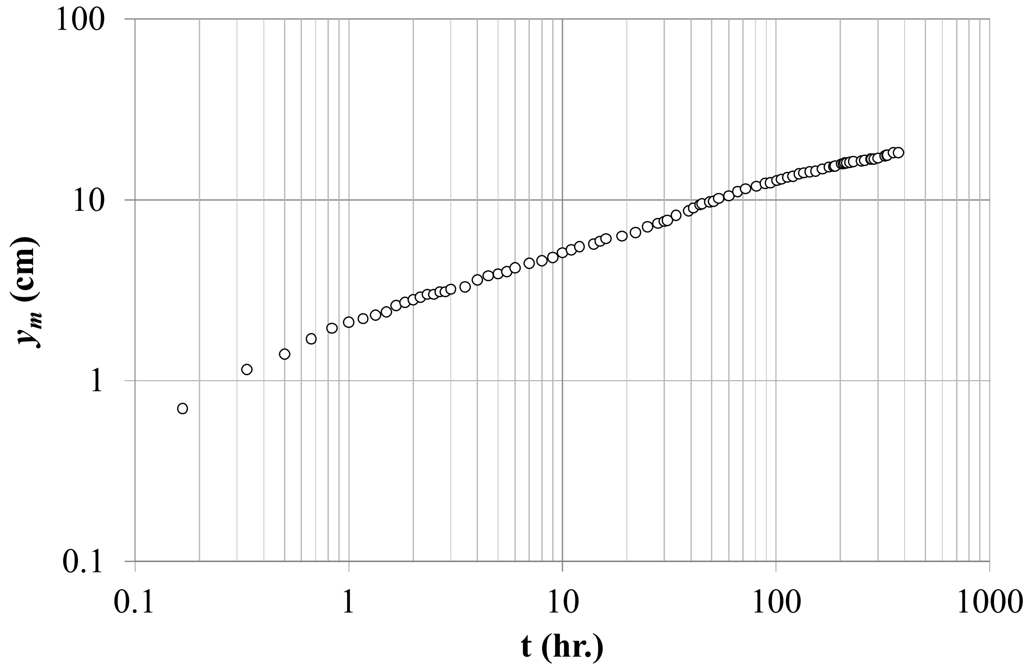

Figure 5.5 Continued

CHAPTER 6

FUNCTIONAL RELATIONSHIPS BETWEEN DOMINANT FACTORS AND LOCAL SCOURING

6.1 Dominant Factors on Local Scouring

Previously analyzed, dominant parameters of flow condition and sediment characteristics were suggested and compared with the scour results. Especially the difference of the turbulent shear layer thickness between fixed bed and movable is significantly dominant. Although this factor has been dominantly suggested by previous studies, Quantification of the development of this thickness has never been applied to estimate and predict the scouring and its development. And also Shields parameter has been used to predict the equilibrium state of the scoured hole.

6.2 Equilibrium-maximum Scour Depth

Equilibrium state of scouring is hard to be predicted due to the slight motions of the particles and continuous bed erosion at the downstream of the scoured hole. Therefore stabilized values from the temporal development of the maximum scour depth can be replaced to predict the maximum scale of the scour hole. This replaced values also can be applied to design of the bed protection. From the results of the experiments, regression equation was formulated as Eq. 4.17 and Figure 6.1. Using the information of the flow conditions at the longitudinal transition and bed materials at the downstream of the bed protection, Equilibrium values of the maximum scour depth can be predicted.

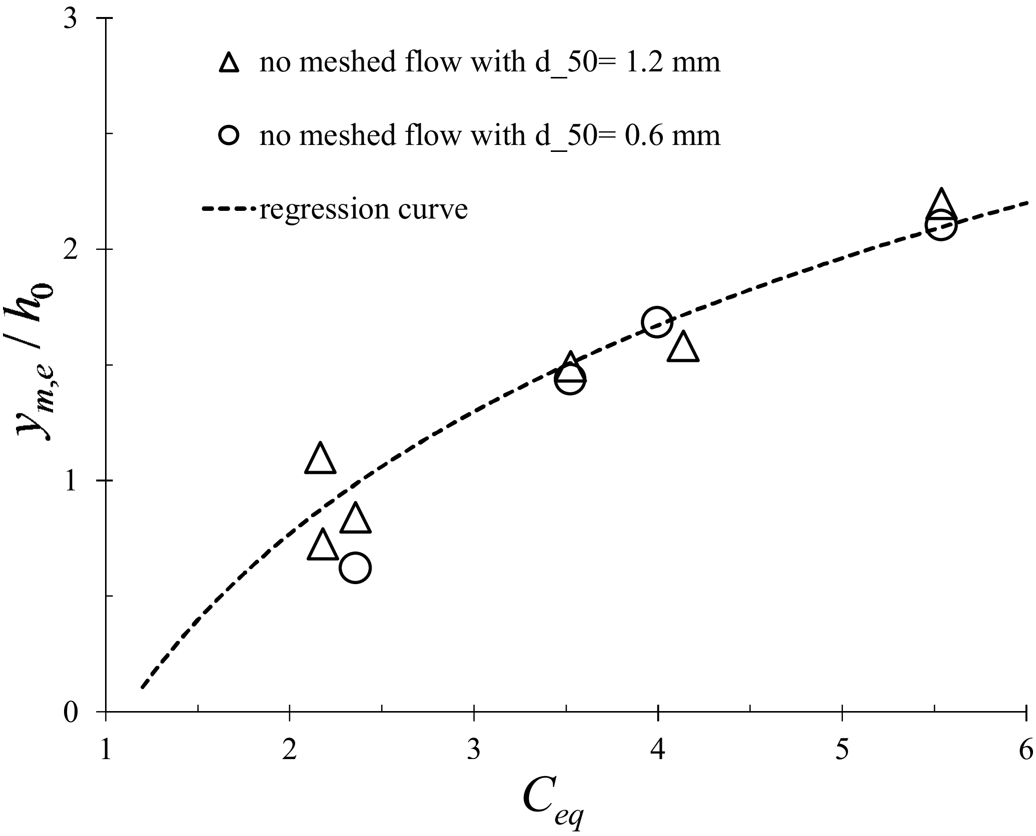

Figure 6.1 Empirical Relationship between Equilibrium Coefficient and the Normalized Equilibrium-maximum Scour Depth

CHAPTER 7

SUMMARY AND CONCLUSION

In this study, experimental approaches were conducted to analyze the local scouring at the downstream of the river bed protection, which is precisely important mechanism for the safety of the upstream hydraulic structures in rivers and streams. To acquire knowledge about the physical processes playing important roles in scouring, 20 cases of flow tests and 13 cases of scour tests were performed with variations of flow condition and sediment particle sizes. From the results of the physical tests in flumes, surface properties of the bed protection, flow condition from the upstream, and sedimentological parameter were revealed as the dominant factors on local scouring. Those results, which can be described with maximum scour depth, and longitudinal length and the position, etc. can be estimated and predicted with appropriate normalized length and time scale. These scales were also represented as the flow characteristics, which is affected from the bed roughness and properties of the movable bed. From the results of 3-D velocity profiles, fully log-law developed flow converted into the baxkward-facing step flow in the scoured hole and excessive values of the turbulent kinetic energy in the turbulent shear layer were measured in the scoured hole. To analyze the countermeasure against the local scouring, mesh grid generated turbulent flow tests were conducted and also scour tests were performed and compared with no mesh cases.

First of all, total durations of this studies were much longer than previous experimental researches (upto 10 times of total duration of previous tests) to reveal the continuity and equilibrium state of the local scouring. And these relatively longer duration could make the regression equation of the equilibrium state of the maximum scour depth. Secondly, previous assumption of the largest vortex size in the empirical equation of the temporal change of the maximum scour depth could be modified with the reasonable dominant factors, which were related to the flow conditions at the longitudinal tiransition and characteristics of the bed meaterials at the movable bed. Thirdly, flow and turbulence characteristics in the stablized scoured hole were analyzed with the high-resolution velocimetry sensor, Vectrino. To analyze the turbulence, statistical method were applied in the despiking the invalid velocity data due to the variation of the flow velocity and sediment transport in the scoured hole.

From the tests, appropriate normalized equation with dominant factors on local scouring can be applied to the cases and field condition. With the prediction of the scour scale, design criteria of the bed protection and gate operation at the upstream of the bed protection will be strongly substantial.

REFERENCES

- Adrian, R. J., and Jerry, W. (2010). *Particle Image Velocimetry*, Cambridge University Press.

- Akselvoll, K., and Moin, P., (1996). "Large eddy simulation of turbulent confined coannular jets and turbulent flow over a backward facing step", *Journal of Fluid Dynamics*, Vol. 315, pp. 387-411.

- Armaly, B. F., Durst, F., Pereira, J. C. F., and Schonung, B. (1983). "Experimental and theoretical investigation of backward-facing step flow", *Journal of Fluid Mechanics*, Vol. 127, pp. 473-496.

- Balachandar, R. and Kells, J. A. (1997). "Local Channel Scour in Uniformly graded sediments: the time-scale problem", *Canadian Journal of Civil Engineering*, Vol. 24, pp. 799-807.

- Balachandar, R., and Patel, V. (2002). "Rough wall boundary layer on plates in open channels", *Journal Hydraulic Engineering*, Vol. 128, pp. 947-951.

- Barkley, D., Gabriela, M., Gomes, M., and Henderson, R. D. (2002). "Three-dimensional instability in flow over a backward-facing step", *Journal of Fluid Mechanics*, Vol. 473, pp. 167-190.

- Bligh, W. G. (1916). *Dams and Weirs: An Analytical and Practical Treatise on Gravity Dams and Weian Analytical and Practical Treatise on Gravity Dams and Weirs, Arch and Buttress Dams, Submerged Weirs and Barrages*, Kessinger Publishing.

- Breusers, H. N. C. (1967). “Time Scale of two-dimensional local scour”, *Proceedings of 12th IAHR-congress*, Fort Collins, Colorado, pp. 275-282.

- Buchko, M., Kolkman, P., Pilarczyk, K. (1987). “Investigation of local scour in cohesionless sediments using a tunnel-model”, *IAHR-congress*, Lausanne; Topics in hydraulic modeling, pp. 233-239.

- Chiang, T. P., and Sheu, T. W. H. (1999). “A numerical revisit of backward-facing step flow problem”, *Physics of Fluids*, Vol. 11, No. 4, pp. 862-874.

- CIRIA, (2007). *The Rock Manual: the use of rock in hydraulic engineering*, CIRIA C638.

- Fessler, J. R., and Eaton, J. K. (1999). “Turbulence modifiaction by particles in a backward-facing flow”, *Journal of Fluid Mechanics*, Vol. 394, pp. 97-117.

- García, C. M., Cantero, M. I., Niño, Y., and García, M. H. (2005). “Turbulence Measurements with Acoustic Doppler Velocimeters”, Journal of Hydraulic Engineering, ASCE, Vol. 131, No. 12, pp. 1062-1073.

- Gartling, D. K. (1990). A test problem for outflow boundary conditions - flow over a backwardfacing step", *International Journal of Numerical Methods in Fluids*, Vol. 11, 953-967.

- Goring, D. G., and Nikora, V. I. (2002). "Despiking Acoustic Doppler Velocimeter Data", *Journal of Hydraulic Engineering*, Vol. 128, No. 1, pp. 117-126

- Graf, W. H., and T. Song. (1995). "Sediment Transport in Unsteady Flow", *Proceedings of 26th Congress*, IAHR, Vol. 1. London.

- Graf, W. H. and Song, T. (2010). "Bed-shear stress in non-uniform and unsteady open-channel flows", *Journal of Hydraulic Research*, Vol. 33, no. 5, pp. 699-704

- Hoffmans, G. J. C. M., and Pilarczyk, K. W. (1995). "Local Scour Downstream of Hydraulic Structures", *Journal of Hydraulic Engineering*, ASCE, Vol. 121 (4), pp. 326-340.

- Hoffmans, G. J. C. M., and Verheij, H. J. (1997). *Scour Manual*, Taylor and Francis Group.

- Hurther, D., and Lemmin, U. (2000). "Shear stress statistics and wall similarity analysis in turbulent boundary layers using a high resolution 3-D acoustic Doppler velocimetry profiler", *Joural of Oceanic Engineering*, Vol. 25, pp. 446-457.

- Jimenez, J. (2004). “Turbulent flows over rough walls”, *Annual Review of Fluid Mechics*, Vol. 36, pp. 173-96.

- Jovic, S., and Driver, D., (1995). “Reynolds number effect on the skin friction in separated flows behind a backward-facing step”, *Experimental Fluids*, Vol. 18, pp. 464-467.

- Jovic, S. (1996). “An Experimental Study of a Separated/Reattached Flow Behind a Backward-facing Step”, NASA Technical Memorandum 110384.

- Kasagi, N., and Matsunaga, A. (1995). “Three-dimensional particle-tracking velocimetry measurement of turbulence statistics and energy budget in a backward-facing step flow”, *International Journal of Heat and Fluid Flow*, Vol. 16, pp. 477-485.

- Katul, G.G., and Parlange, M.B. (1995). “Analysis of Land Surface Heat Fluxes using the Orthonormal Wavelet Approach”, Water Resource Research, Vol. 31, pp. 2743-2749.

- Keirsbulck, L., Labraga, L., Mazouz, A., and Tournier, C. (2002). “Surface roughness effects on turbulent boundary layer structures”, *Journal of Fluids Engineering*, Vol. 124, pp. 127-135.

- Kim, J., Kline, S. J., and Johnston, J. P. (1985). "Investigation of a reattaching turbulent shear layer: flow over a backward-facing step", *Journal of Fluids Engineering*, Vol. 102, pp. 302-308.

- Kundu, P. K., and Cohen, I. M. (2008). *Fluid Mechanics* (4th revised edition), Academic Press

- KWRA. (2009). *Design Criteria of the Hydraulic Structures and River Managements in Rivers*, KWRA.

- Le, H., Moin, P., and Kim, J. (1997). "Direct numerical simulation of turbulent flow over a backward-facing step", *Journal of Fluid Dynamics*, Vol. 330, pp. 349-373.

- Lee, D. H. and Son, M. (2012). "Investigation on Mean Diameter of Bed Material and Relationship with Tractive Force in Korean Rivers", *Journal of the Korean Geomorphological Association*, Vol. 18, No. 1, pp. 1-11 (in Korean).

- Lee, T., and Mateescu, D. (1998). "Experimental and numerical investigation of 2-D backward facing step flow", *Journal of Fluids and Structures*, Vol. 12, pp. 703-716.

- Malley, K. O., Fitt, A. D., Jones, T. V., Ockendon, J. R., and Wilmott, P. (1991). “Models for high-Reynolds-number flow down a step”, *Journal of Fluid Mechanics*, Vol. 222, pp. 139-155.

- Nakagawa, H., and Nezu, I. (1987). “Experimental investigation on turbulent structure of a backward facing step flow in an open channel”, *Journal of Hydraulic Research*, Vol. 25, pp. 67-88.

- Neumann, J., and Wengle, H. (2003). “DNS and LES of passively controlled turbulent backwardfacing step flow”, *Flow, Turbulence and Combustion*, Vol. 71, pp. 297-310.

- Nezu, I, and Nakagawa, H. (1993). *Turbulence in Open-Channel Flows*, IAHR Monograph.

- Nikora, V., and Goring, D. (2000). “Flow turbulence over fixed and weakly mobile gravel beds”, *Journal of Hydraulic Engineering*, Vol. 126, pp. 679-690.

- Nortek (2009*). User Guide of Vectrino Velocimeter*.

- O’Neill, P. L., Honnery, N. D., and Soria, J. (2004). “Autocorrelation Functions and the Determination of Integral Length with Reference to Experimental and Numerical Data”, *Proceedings of 15th Australasian Fluid Mechanics Conference*, The University of Sydney, Sydney, Australia, pp. 13-17.

- Raffel, M., Gharib, M., Ronneberger, O., and Kompenhans, J. (1998). *Particle Image Velocimetry- A Practical Guide*, Springer.

- Rani, H. P., Sheun, T. W. H., and Tsai, E. S. F. (2007). "Eddy structures in a transitional backward-facing step flow", *Journal of Fluid Mechanics*, Vol. 588, pp. 45-58.

- Rashid, S. M. H. (2010). "Effectiveness of Widely Used Crtical Velocity and Bed Shear Stress Equations for Different Types of Sediment Beds", MsD. Thesis, Washinton State University.

- Schultz, M. P., and Flack, K. A. (2003). "Turbulent boundary layers over surfaces smoothed by sanding", ASME, *Journal of Fluids Engineering*, Vol. 125, pp. 863-870.

- Simões, F. J. M. (2014). "Shear velocity criterion for incipient motion of sediment", *Water Science and Engineering*, Vol. 7, No. 2, pp. 183-193.

- Shields, A. (1936) *Application of Similarity Principles and Turbulence Research to Bedload Movement*. Berlin: Wasserbau Schiffbau.

- Stella, A., Guj, G. Kompenhans, J., Raffel, M., and Richard, H. (2001). "Application of particle velocimetry to combusting flows: design considerations and uncertainty assessment", *Exp Fluids,* 30, 167-180.

- Tachie, M., Bergstrom, D., and Balachandar, R. (2000). "Rough wall turbulent boundary layers in shallow open channel flow", *Journal of Fluids Engineering*, Vol. 122, pp. 533-541.

- Termini, D. (2011). "Bed Scouring Downstream of Hydraulic Structures Under Steady Flow Conditions: Experimental Analysis of Space and Time Scales and Implications for Mathematical Modeling", *Catena*, Vol. 84, pp. 125-135.

- Tritton, D.J. (1988). *Physical Fluid Dynamics*, 2nd Edition, Oxford University Press.

- TSI Inc. (2004). *Insight3G user's manual.*

- ul Haque, A., Yamada, F. A. S., and Chaudhry, S. (2007). "Assessment of turbulence models for turbulent flow over backward facing step", *Proceedings of the World Congress on Engineering II.*

- USACE. (1987). *Hydraulic Design of Navigation Dams*, Engineering Manual, U.S. Army Corps of Engineers, USA.

- USACE. (2006). *Hydraulic Design of Navigation Locks*, Engineering Manual, U.S. Army Corps of Engineers, USA.

- USBR. (1984). *Hydraulic Design of Stilling Basins and Energy Dissipators*, A Water Resources Technical Publication, Bureau of Reclamation, U.S. Department of the Interior, USA.

- USBR. (1987). *Design of Small Dams*, A Water Resources Technical Publication, Bureau of Reclamation, U.S. Department of the Interior, USA.

- USBR. (1987). *Hydraulic Laboratory Techniques*, A Water Resources Technical Publication, Bureau of Reclamation, U.S. Department of the Interior, USA.

- Van der Meulen, T. and Vinjé, J. J. (1975). "Three-Dimensional Local Scour in Non-cohesive Sediments", *Proceedings of 16th IAHR-congress*, san Paulo, Brasil.

- Vermaas, D. A. (2008). "Mixing layers in open channel flow with abrupt bed roughness changes", Ms. D. Thesis, Wageningen University.

국문초록

하천 하상보호구조물 하류부에서 국부세굴에 관한 실험적 연구

서울대학교 대학원
건설환경공학부
박 성 원

하천 하상보호공 직하류부에서 발생하는 국부세굴은 고정식 혹은 수문식 위어, 그리고 댐 여수로 등의 상류부 수리구조물의 설계 및 지속가능한 관리측면에서 매우 중요한 부분 중 하나이다. 특히 수리구조물 주변에서 발생하는 하상재료의 유실은 상류부 수리구조물의 안전성에 큰 위협이 될 수 있다.기존 연구에서는 수치 해석적 및 실험적 연구를 통해, 국부세굴발생의 지배인자가 시간 변화성, 흐름 및 난류특성, 그리고 하상재료의 속성 등이라고 제안된 바 있다. 하지만 연구의 부적절한 가정과 계측방법 및 모니터링의 한계로 인하여 경험식이나 예측식이 불분명하게 쓰이고 있는 실정이다.

따라서 본 연구에서는 보다 진보된 설비와 계측방식을 활용한 고정하상 하류부에서의 국부세굴 실험이 수행되었다. 본 실험적 연구는 고정하상과

이동하상의 경계지점에서 발생가능한 과도한 하상유실의 방지를 위하여, 국부세굴공의 시간발달양상과 각 시간변화에 따른 세굴공 내부에서의 흐름 및 난류특성의 분석에 초점을 맞추었다. 우선, 시간변화에 따른 하상고의 변화를 측정하여 발생가능한 최대세굴심의 예측에 사용될 수 있는 최대세굴심의 시간변화율과 수리조건과의 경험적 관계식을 수립하였다, 특히 흐름방향 경계지점에서의 수심적분된 상대난류강도값과 하상전단응력 최대세굴심의 시간변화율과 평형상태값에 지배적임을 분석하였다. 그리고 안정화된 세굴공 내부에서의 흐름 및 난류특성을 분석하기 위해서 유사한 양상을 나타내는 후면단차흐름조건에서 PIV와 ADV 계측방법을 이용하여 흐름 및 난류특성을 계측 및 분석하였다. 고해상도의 PIV 계측결과와 적분시간규모가 고려된 앙상블평균방법과 디스파이킹된 3차원 ADV 계측결과로부터 단차주변에서의 흐름 및 난류특성을 분석할 수 있었다. 이 방법을 통해 안정화된 세굴공 내부에서 발생하는 회전류와 난류전단층의 발생이 추가적인 하상재료의 유실에 영향을 미치는 것을 분석하였다.

그리고 발생가능한 최대세굴심의 적절한 방지법을 찾기 위해서, 흐름방향 경계지점에 메쉬망 난류흐름조건에서의 동일한 국부세굴실험을 수행하였다. 메쉬망 난류흐름조건을 통해 발생된 수심적분된 상대난류강도의 증가는 최대세굴심의 저감 및 지체를 야기하였다. 본 연구에서 제안된 경험식을 이용하면 기존에 알려진 수리학적 인자만으로 하천 하상보호공 직하류에서 발생 가능한 국부세굴심을 예측할 수 있으며, 또한 국부세굴심 저감을 위한

하천 하상보호공의 보완 및 설계 시에 정량적인 목표치로 활용될 수 있을 것으로 사료된다.

주요어: 국부세굴, 하천 하상보호공, 수심적분된 상대난류강도, 최대세굴심, 하상전단응력, 난류전단층, 메쉬망 난류흐름

학번: 2009-30231